学位論文

A Precise Measurement of Cosmic Ray Proton Spectrum

（宇宙線陽子スペクトルの精密測定）

平成８年１２月 博士（理学）申請

東京大学大学院理学系研究科

物理学専攻

佐 貫 智 行

A Precise Measurement of Cosmic Ray Proton Spectrum

By
Tomoyuki Sanuki

Department of Physics,
School of Science,
University of Tokyo

1996

Abstract

This dissertation describes the measurement of cosmic ray proton spectrum using the data obtained from three balloon flights of BESS [1] spectrometer which was launched from Northern Canada in 1993, 1994, and 1995.

In the analysis, events with a single track in the tracking chamber were selected. The identification of protons are based on the measurements of magnetic rigidity[2], time of flight, and energy loss in the plastic scintillators. The selected events were checked based on the tracking qualities, and also on the consistency among the responses of the different components of the detector. The overall selection efficiency was as high as 75%. After correcting for the selection efficiencies and for the losses due to interaction in the air and in the detector, we've obtained energy spectra for three flights in the energy region from 0.4 to 100 GeV with an estimated systematic accuracy of 10%. The measured energy spectrum from three flights data are in good agreement above 10 GeV, where the effect of solar modulation can be neglected, whereas in lower energy region, the effect of solar modulation is clearly observed.

[1] Baloon-borne Experiment with a Superconducting Magnet Spectrometer
[2] momentum per charge

Contents

List of Tables

List of Figures

Chapter 1

Introduction

Cosmic rays, the charged particles from the space, enter the atmosphere at the rate of about 1,000 per square meter per second. Among the cosmic ray particles, proton is the most abundant element, which accounts for about 90% of cosmic rays, thus the energy spectrum and absolute flux of cosmic ray proton constitute most important fundamental data in cosmic ray physics. The spectrum carries the informations on the origin and the propagation history of the cosmic rays in Galaxy. The change of the spectrum shape at the lowest energies with the solar activity (solar modulation) provides a basis to study the effect of the solar wind to the cosmic rays.

The absolute flux and the energy spectrum of the incident cosmic ray protons are also crucially important to study the terrestrial phenomena caused by the cosmic rays. A dramatic example is the atmospheric neutrino problems. Recently several underground experiments started to measure the interactions of the atmospheric neutrinos. Kamiokande and subsequently IMB have reported on anomaly in the ratio of the neutrino events including muons and electrons in the final states (μ/e anomaly), indicating the anomaly in the fluxes of ν_μ ($\bar{\nu_\mu}$) and/or ν_e ($\bar{\nu_e}$) at sub- and multi-GeV region [1][2][3]. They preferred to use the μ/e ratio, since they suspect a large ambiguity in the calculation of the absolute ν_μ and ν_e fluxes, which will mostly cancel out if one takes the ratio. However, in order to fully understand the origin of the atmospheric neutrino problem, one finally needs to compare the expected absolute flux of both ν_μ ($\bar{\nu_\mu}$) and ν_e ($\bar{\nu_e}$) to the observed μ - and e - events. The ambiguity in the calculation of the atmospheric neutrino fluxes comes mainly from the fluxes of the cosmic ray proton and helium as well as from the simulation of the proton and helium interaction in the atmosphere. Therefore, precise measurements of the absolute energy spectra of cosmic ray protons and heliums are very much needed. The ambiguity in simulating the interactions can then be constrained by accurate measurements of $\mu^\pm$ spectra at ground as well as at various depth of the atmosphere. As seen in Figure 1.1, the neutrino fluxes at sub-GeV to multi-GeV region, which are of current interests, are determined by the proton fluxes at a few to 100 GeV region[4].

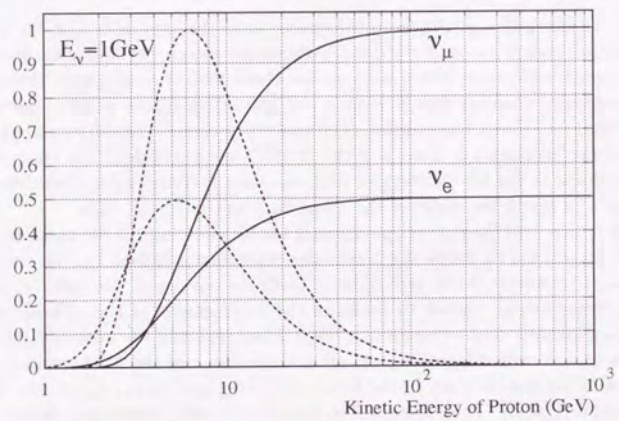

Figure 1.1: ν-yield function for protons for ν_e and ν_μ. It is shown in in integrated (solid line) and differential (doted line) form [4].

Reliable data on the absolute spectrum at this energy region are also important as the anchor-points to determine the energy spectrum at higher energy region, where various measurements with the emulsion chambers have determined the absolute flux scale of the spectra index γ in a reasonably reliable manner while suffering from large systematic errors in the absolute flux.

Although above examples show the need for the precise measurements of the absolute cosmic ray proton spectrum in GeV to 100 GeV region, previous data are not consistent with each other, by up to a factor of two, as shown in Figure 1.2.

Figure 1.3 shows a typical example of previous "spectrometer telescopes" utilized for these measurements[9]. It has small tracking volume and small numbers of tracking points, which, together with the non-uniform magnetic field, might make precise measurement of absolute rigidity[1] difficult. The tracking devices seem to be arranged such that the cosmic ray interactions with the material around the detector system might not always detected. The secondary particles from such interactions might thus contribute to backgrounds.

The detector of BESS (Baloon-borne Experiment with a Superconducting Magnet Spectrometer) system is an unique apparatus which incorporates new technologies cultivated in the collide experiments; a thin superconducting solenoid, precise tracking detectors, and a high-speed data acquisition system. The BESS detector performs continuous and redundant trackings with multi-track capabilities. The superconducting solenoidal magnet offers a uniform magnetic field in the fiducial volume. Thanks to these advantages, the BESS detector can measure absolute rigidity of incident particles precisely, and recognize interactions which happens at the detector. The simple and wide geometry makes it trivial to precisely determine the effective area and the solid angle. Furthermore, cylindrical configuration provides large geometrical acceptance, which results to measurements with small statistical errors and high sensitivity. The high number of events also allow us to perform detailed checks on the systematic errors by using the collected events themselves.

This thesis report on a measurement of cosmic ray proton spectrum by BESS detector in the energy region 0.3 to 100 GeV, based on the data collected in '93, '94 and '95.

[1] momentum per charge

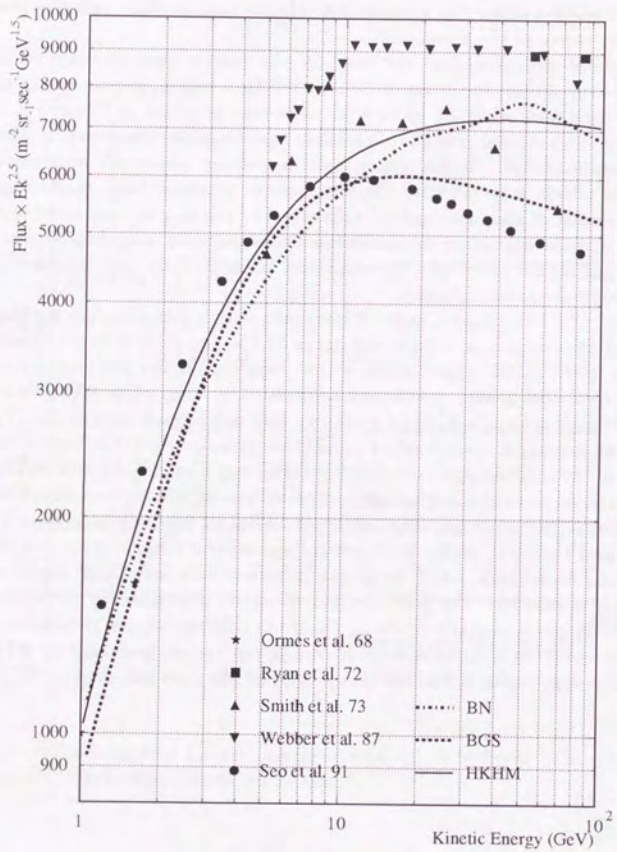

Figure 1.2: Absolute differential proton spectrum obtained by previous experiments [5][6][7][8][9] together with those assumed spectrum in MC calculations of the atmospheric neutrino spectra by BGS[11], HKHM[12] and BN[13].

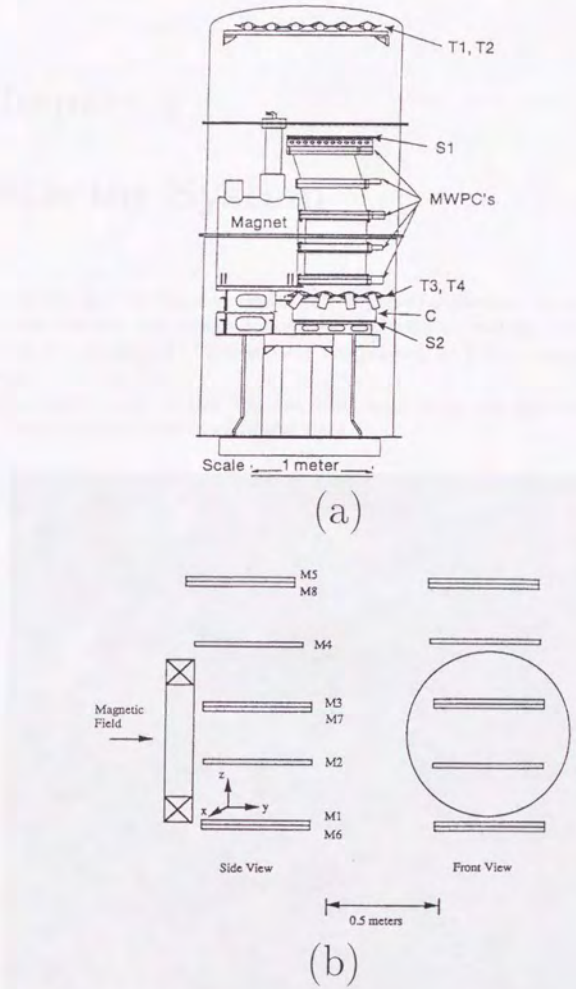

Figure 1.3: Schematic view of (a) a typical telescope prior to BESS detector; (b)its tracking device (magnet and MWPCs) [9].

Chapter 2

Detector System

This chapter provides an overview of the employed apparatus. Section 2.1 describes the basic features and design concept of the detector system, while the following sections discuss its individual detector components and data acquisition system in detail.

The performance of the detector, evaluated using the flight data after event selections, is mostly described in section 4.2.

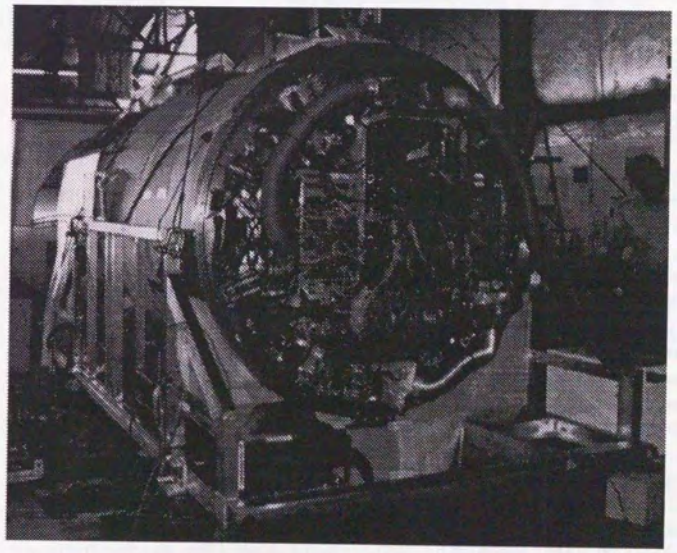

Figure 2.1: photograph of the BESS instrument ('95).

2.1 Basic Features

The BESS detector system was proposed with the primary purpose to perform a very sensitive search for rare cosmic particles, such as the low energy $\bar{p}$'s, anti-heliums and exotic heavy particles (strange matter etc.) [14]. The detector was designed also to be omni-purpose, i.e. to be able to provide fundamental data on cosmic rays such as the precision energy spectra of protons, helium, electron and positron as well as various light isotopes. Figure 2.1 is a photograph of the BESS instrument. Figure 2.2 shows a cross-sectional view of the BESS instrument in '93,'94 and '95 flight, respectively. Main parts of the BESS detector are common in all three flights, but some parts are improved year by year.

The detector system consists of jet chamber (JET), inner drift chambers (IDCs), outer drift chambers (ODCs), and time-of-flight hodoscope (TOF). These components are arranged in a cylindrical shape resulting in a large geometrical acceptance of up to ~ 0.4 m^2 sr. JET and IDCs compose the central tracking device with minimum material, immersed in a strong magnetic field of 1T produced by superconducting coil (MAG). This system functions as a magnetic rigidity (momentum per charge) spectrometer with an accuracy of 0.5% at 1 GV and with maximum detectable rigidity (MDR) of 200 GV. The track information is digitized and recorded on magnetic tape on board. The off-line analysis reconstruct the particle's trajectory three dimensionally. Since the tracking is redundant and measure up to 32 points per track, most abundant single track events as well as complicated events having interactions can easily be recognized (shown in Figure 2.3), thus minimizing the background of the secondary particles from such interactions.

Outside the coil, ODC also record the track position. The time-of-flight counters at the outermost layer measure the flight time of the particle between two scintillation counters.

All these components, along with the front-end electronics and microcomputers, are enclosed by a 2-mm-thick aluminum pressure vessel to keep the internal pressure around one atmosphere throughout the flights.

The data storage device, consisting of 8 mm video tapes and the driver, is contained in iron cylinder, which protect the data recorders from strong magnetic field and from cold atmosphere as well as from possible damages at the landing. A battery power supply system is situated outside the vessel and at the far most corner below the payload, well outside the solid angle. And a consolidated instrument package (CIP) communication unit, which is supplied by the National Scientific Balloon Facility (NSBF) and handles communications between the BESS payload and ground station, is also situated in an iron box outside the pressure vessel.

The apparatus weighs 2.2 ton including 180 kg batteries, and the dimension is 1.5 m in diameter and 3.3 m in length.

In order to minimize the effects of interactions at upper atmosphere, BESS payload ascend by a 29.5-Mft^3 helium-filled balloon up to about 35km which corresponds 5 g/cm^2 of residual air thickness.

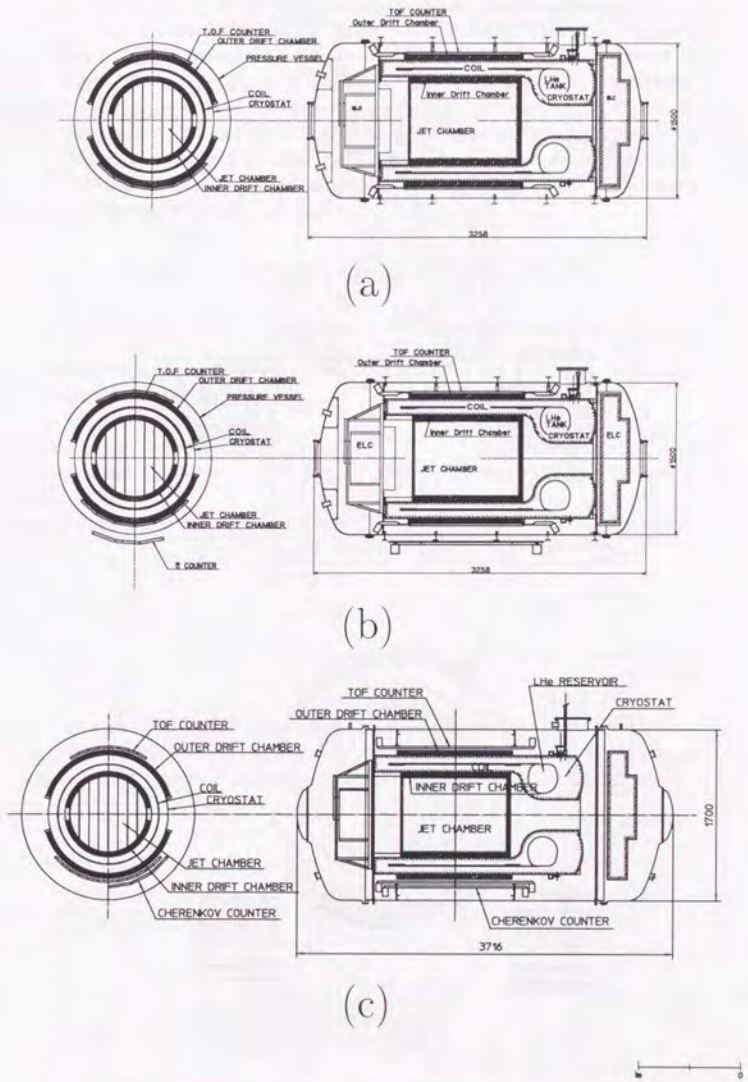

Figure 2.2: Cross-sectional view of the BESS instrument; (a):'93, (b):'94 and (c):'95.

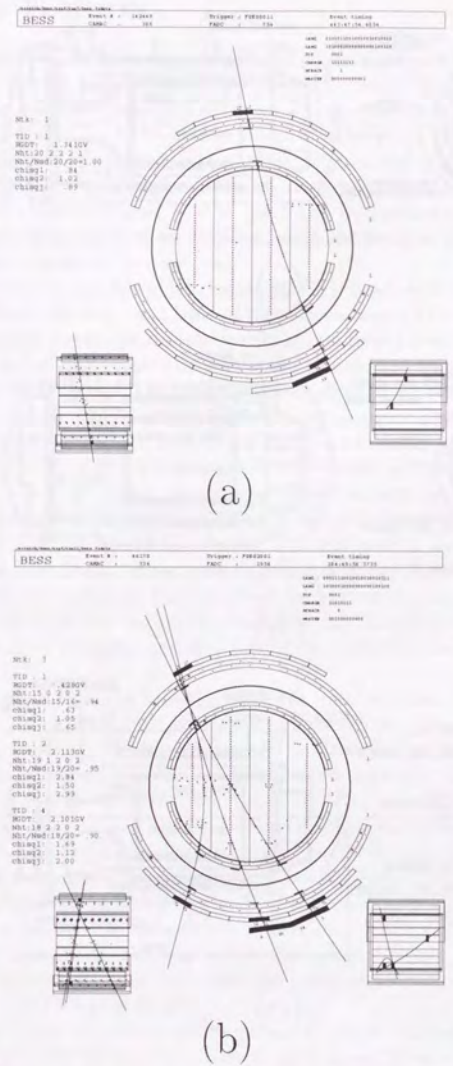

Figure 2.3: Examples of event display collected during '95 flight. (a)single track event;(b)three-track event showing the interaction at the coil.

Figure 2.2(b) shows a cross-sectional view of the BESS instrument in '94 flight, and Figure 2.2(c) shows that in '95 flight. In '94 flight, Čerenkov counters were added outside of the pressure vessel to improve the particles identification. In '95, a new larger pressure vessel was utilized to contain the Čerenkov counters. The remarkable improvement in '95 was the new TOF counters: The width of each counter was reduced to half of the old one, and the new light guides and the new photo-multipliers with high quantum efficiency were utilized, resulting to an 110 p sec TOF resolution instead of 280 p sec in '93 and '94. Table 2.1 summarize the main specifications of BESS instrument.

Table 2.1: Main specifications of BESS instrument.

	'93	'94	'95
Geometrical acceptance	0.4 m^2 sr	0.4 m^2 sr	0.32 m^2 sr
Maximum detectable rigidity		200 GV	
Trigger rate		100 – 200 Hz	
Material in the instrument		9 g/cm^2	
Pressure vessel dimension	1.5 m$\phi \times$ 3.3 m	1.5 m$\phi \times$ 3.3 m	1.7 m$\phi \times$ 3.8 m
Total weight	2.1 t	2.1 t	2.2 t
Power consumption	1.2 kW	1.2 kW	1.2 kW

In this dissertation, the cylindrical coordinates ($r\phi z$) and the rectangular coordinates (xyz) are used by defining the direction of the magnetic field at the center of the magnet as the z-axis, and the vertical direction as y-axis.

2.2 Superconducting Solenoidal Magnet

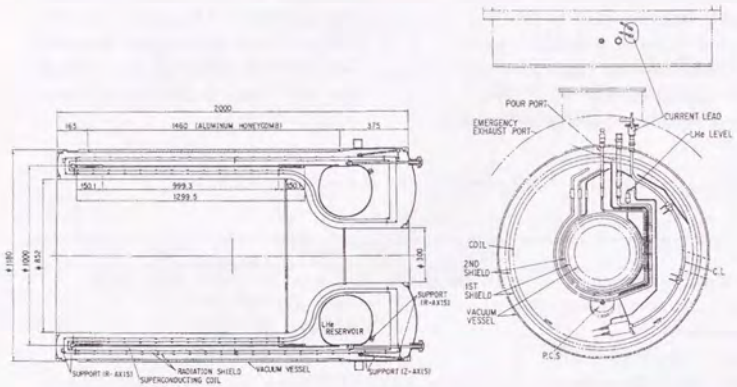

Figure 2.4: Cross-sectional view of the superconducting solenoidal magnet.

Figure 2.4 shows cross-sectional views of the superconducting solenoidal magnet (MAG) [15]. A solenoidal coil and a liquid helium reservoir tank are encased in a vacuum vessel which has a 0.85 mϕ $\times$ 1.0 m warm bore that encloses the JET and IDCs.

The solenoidal coil is made of aluminum-stabilized superconductor NbTi(Cu). It has a dimension of 1 m in diameter, 1.3 m in length and 5.2 mm in thickness. In order to ameliorate the field uniformity, extra coils of 15 cm long $\times$ 5.2 mm thick are attached at both end, and the residual field uniformity is $\pm 15\%$ for the entire area where the central tracker is sensitive. The solenoidal coil is encompassed by aluminum support cylinder which is welded to the toroidal-shaped liquid helium reservoir tank of a capacity of 150-ℓ. The coil was cooled down not directory but via the support cylinder. This static indirect cooling method has an advantage over the usual bath cooling method in that there is no need for any action during balloon flight and it allows using a thinner cryostat wall. [15]. The thickness of the MAG including the cryostat is 0.21 radiation length per wall and its total weight with helium is 430 kg. The coil, the reservoir tank and the support cylinder are enclosed with two layers of thermal radiation shields, and are contained in the vacuum vessel. The magnet is equipped with a heater and a persistent current switch (PCS) fabricated from a superconductor During magnet excitation, PCS is heated up to break the superconduction (switch-off), and the current from a DC power supply is poured into the coil. After being charged, PCS is cooled and automatically shortcut (switch-on) to close the circuit composed of the coil and the PCS. In the operational condition, a

magnetic field of 1T is generated inside the warm bore at a current of 430A, and the energy stored in the magnet amounts to 555 kJ. Although the decay time constant of this current is more than 900 years, an operational period of the magnet is limited to about 6 days because of finite volume of the reservoir tank. In order to "switch off" the magnet, the stored energy is extracted by heating up PCS again and thus by shunting the current into a register located outside the vessel. Table 2.2 summarizes the main specifications of the MAG.

Table 2.2: Main specifications of the superconducting solenoidal magnet (MAG).

Coil	Conductor		NbTi/Cu
	Diameter		1.0 m
	Length		1.3 m
	Thickness	(center)	5.2 mm
		(end)	10.4 mm
	Inductance		6 H
Cryostat	Outer diameter		1.18 m
	Inner diameter		0.85 m
	Length		2.0 m
	L-He capacity		150 liters
			6 days
Support cylinder	Material		A2219
	Thickness	(center)	2 mm
		(end)	4 mm
Central field		(nominal)	1.0 T
		(maximum)	1.2 T
Current		(nominal)	430 A
		(maximum)	520 A
Wall thickness			4 g/cm^2 (0.21 X_0)
Total weight			430 kg

2.3 JET chamber

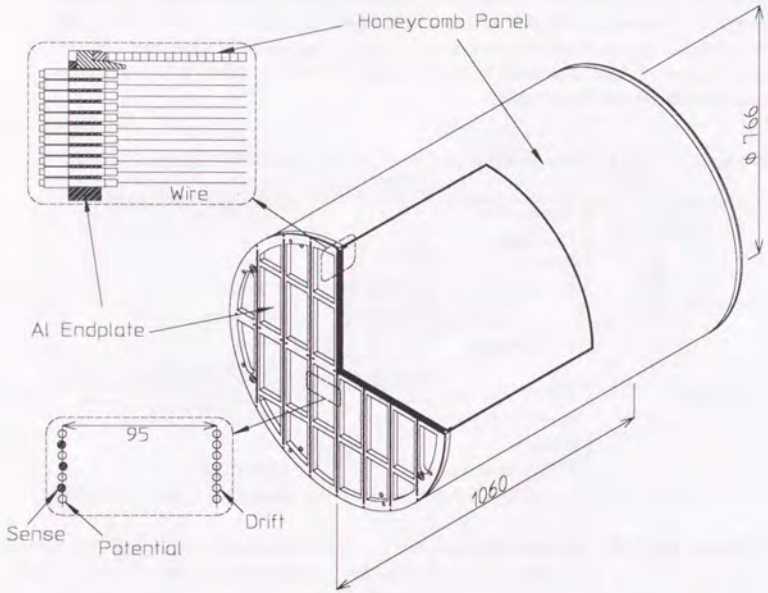

Figure 2.5: Schematic view of the JET chamber.

2.3.1 Structure

The JET chamber is a drift chamber with a large tracking volume of 0.754 m$\phi \times$ 1 m. A schematic view of the JET is shown in Figure 2.5. In order to minimize material thickness and reduce its weight, the cylindrical side walls are made of aramid core honeycomb, which is enclosed with two end plates made of aluminum disks. The chamber's total weight is only 60 kg.

Parallel to the axis of the cylinder, wires are strung at 6.7-mm intervals in seven lines between two aluminum end plates. According to electric potential, the wires are divided to three categories, i.e. drift wires, potential wires and sense wires. The potential (cathode) and drift wires are 200-μmϕ gold-plated aluminum wires. The sense wires are 20-μmϕ gold plated tungsten-rhenium wires. which are staggered by 0.5 mm to solve the left-right ambiguity. The potential and sense wires run alternately at 13.4 mm intervals. The potential wires function to lead drift electrons smoothly to the sense wires. To avoid the mechanical instability of the wires due to the electrostatic force between wires, they are stretched with a tension of 40 gw for

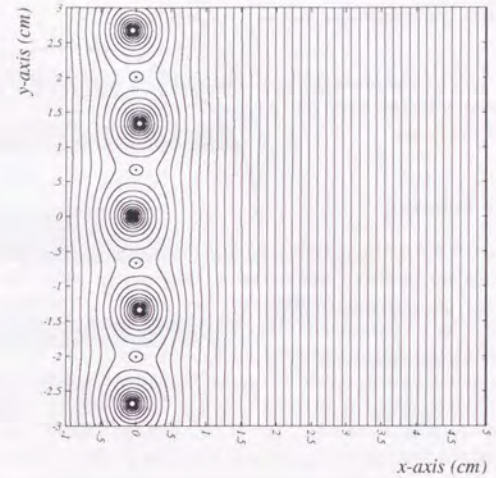

Figure 2.6: Equipotential contour map of the electric field of JET chamber.

sense wires, 350 gw for potential and drift wires.

Field-shaping patterns are etched on the inner surface of the honeycomb panel. Applying a negative potential of −10.8 kV to the drift wires and the appropriate potential to the field-shaping patterns, a constant electric field of about 1.0 kV/cm perpendicular to the magnetic field is produced (Figure 2.6). In that field, the electrons liberated in the ionization process of the cosmic rays drift into the high amplification region around the sense wires where avalanche formation occurs. The maximum drift distance of ionized electrons is 95 mm. The cylindrical volume is subdivided into four rectangular segment of 190 mm width by three cathode planes each of which actually consists of about a hundred of drift wires. At the center of each section, the sense and potential wires are aligned. In each middle (peripheral) two segment among four, there are 52 (32) sense wires and 53 (33) potential wires, namely a total of 168 sense wires and potential wires.

The chamber is filled with a mixture of 90% CO_2 and 10% Ar, being suitable for this experiment due to the following reasons:

1. The drift velocity of this gas mixture, 6.6 mm/μs, is slow enough to achieve good position resolution using a relatively slow electronics package designed for low power consumption, which is crucial for balloon experiments.

2. Due to a small diffusion coefficient, timing fluctuations caused by the longitudinal diffusion of the electron cloud are small even after a long drift of 95 mm.

3. The gas mixture is non-flammable and easy to handle.

This mixture was used for the other drift chambers for the same reasons. In fact, the entire vessel is filled with the same gas so that any chamber suffering a small gas leak will remain operational.

2.3.2 Read-out scheme

The signals from the sense wires are picked up by preamplifiers mounted on the end-plates, where the signals are amplified and converted into voltage ones. The signals are then fed into flash-type analog-to-digital converter (FADC) modules mounted in the electronics rack. The FADC modules further amplify the signals and digitize them into 8-bit digits at the rate of 28.5 megasample/second, i.e. every 35 ns. This sampling rate is well suited to record the pulse shape with a typical width of about 400 ns. Each of the module has 16 input channels and is able to measure the waveforms simultaneously with a record length of 512 samples (about 18μs) each, which is long enough for the full drift time of 14 μs. Since the FADC modules log the shape of each input waveform, the multiple tracks can be recognized if they are apart by more than 3 mm. In order to reduce the data size, the on-line zero-suppression circuits are employed to discard the data not containing signal pulse information, where the digitized 8 bits data are compared with the prescribed threshold and only data above a threshold value is accumulated into first-in-first-out (FIFO) memory. Thus data zero suppression is executed on a real-time basis. A data compressor circuit then scans all the FIFO memories sequentially and packs the pulse shape information into the compressed hit-data, which has a 8-byte format and contains the readout channel number, total charge, pulse width, and the pulse heights of the first two samplings. In this way, the principal informations on the signal pulse are kept while reducing the the data size by a factor of 3. It takes 200 μs for the compressor to scan all channels and complete the process for an event with typical data size.

The signals from 80 sense wires out of 168 were read in the experiment, to reduce the number of the FADC modules and the power consumption. Because delay time between the crossing of a charged particle and the pulse on the sense wire is essentially proportional to the distance between particle trajectory and sense wire, this measurement with FADC makes it possible to determine the track trajectory in $r-\phi$ plane (in the plane perpendicular to the magnet field direction).

In order to determine the z-coordinate, 48 (64) sense wires among the 80 'active' wires were read from both ends in '93 ('94 and '95) flight. As the tracks pass through the central region, 24 positions can be measured both in the $r\phi$ plain and for the z direction. The location of the read-out wire is shown in Figure 2.7. The hit position along the wire is obtained by applying the charge division method. Figure 2.8 shows the principle of the method. To minimize errors, the internal resistor and gain of the amplifier are calibrated using the actual flight data. As is described above, the particle's trajectory can be reconstruct in three dimensional.

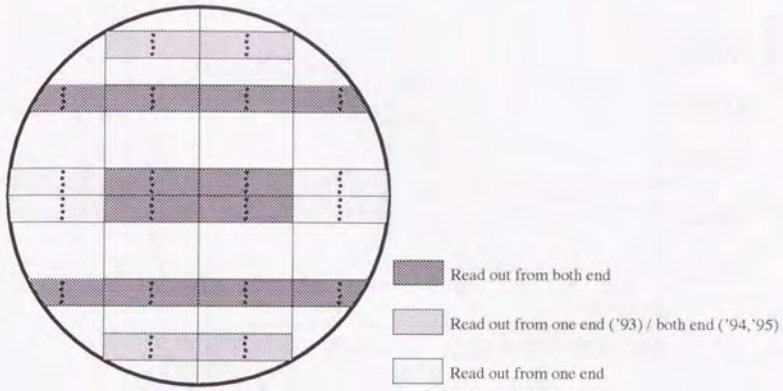

Figure 2.7: The location of the read-out wires in JET chamber.

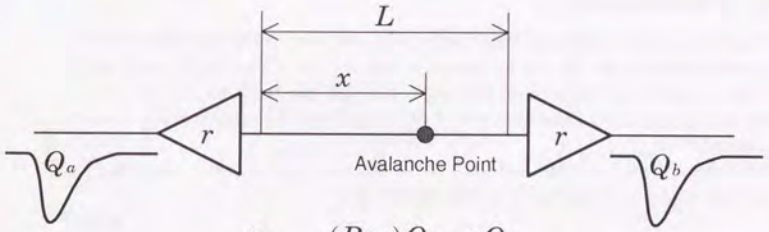

$$\frac{x}{L} = \frac{(R+r)\,Q_b - r\,Q_a}{R\,(Q_a + Q_b)}$$

L : Wire length

R : Wire resistance

r : Preamplifier input resistance

Figure 2.8: Circuit model of the charge division method used for determining the z-coordinate.

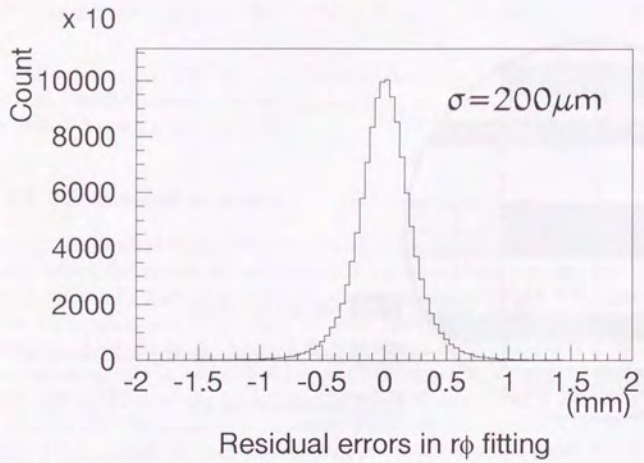

Figure 2.9: Residual distribution of the JET $r\phi$ hit points.

2.3.3 Performance

Based on the residuals obtained from the fitted track, the overall resolution in $r-\phi$ plane is estimated to be 200 μm as shown in Figure 2.9. This resolutions depends on the drift length and slightly on the angle between the track trajectory and the cathode wire plane, due to the diffusion of drift electrons. The dependence is shown in Figure 2.10.

As for the z direction, the resolution is 2.5 cm for single-charged particles (Figure 2.11 (a)) and 1.5-cm for helium (Figure 2.11 (b)).

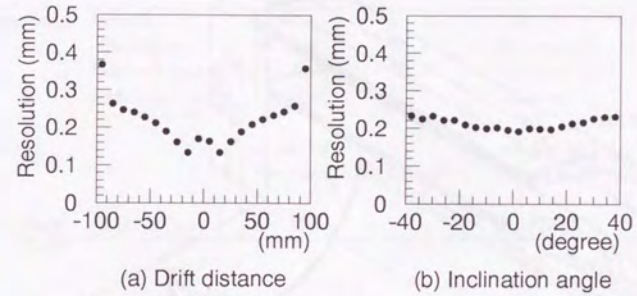

Figure 2.10: JET chamber $r\phi$ resolution as a function of (a) the drift distance, and (b) the angle ϕ across the cathode wire plane.

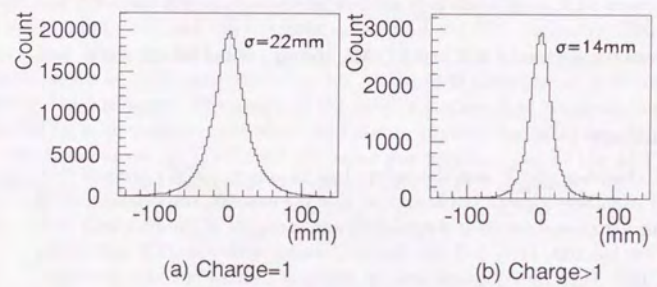

Figure 2.11: Residual plot of the JET chamber along the z-coordinate for (a) single-charged and (b) multiple-charged particles

2.4 Inner and Outer Drift Chamber

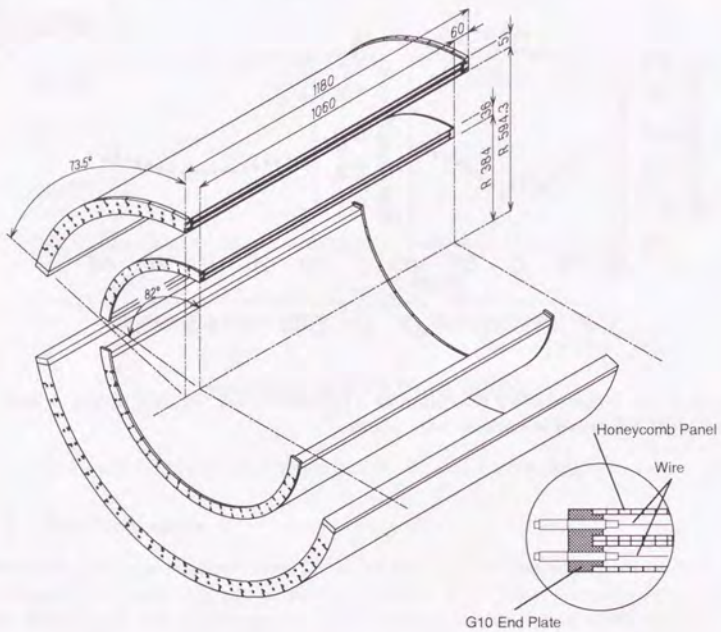

Figure 2.12: Schematic view of IDC and ODC, the upper set shows their cross sections.

2.4.1 Structure

The inner drift chamber (IDC) and the outer drift chamber (ODC) are cell-type arc-shaped drift chambers located inside and outside the magnet, respectively. Both chambers are similar except for their dimensions and strength of the magnetic field in which they are located, i.e. , 1 T for the IDC along with the JET and about 0.1 T for the ODC. They function not only as tracking devices but also as trigger chambers. As shown in figure 2.12, the mechanical structure of each chamber is composed of four semi-cylindrical walls of honeycomb panels and end/side plates of engineering plastic (G10). Some basic features of both chambers are listed in table 2.3.

Figure 2.13 depicts a cross-sectional view of the $r\phi$ plane. Four honeycomb panels form double layer structure and each panel has 3 mm-thick aramid-core and 125 μmm-thick KAPTON-surface on which copper sheets of 18 μm thickness are

Table 2.3: Basic features of IDC/ODC.

		IDC	ODC
Dimensions	Length	1.06 m	1.18 m
	Thickness	36 mm	44 mm
	Internal radius	384 mm	594 mm
	External radius	420 mm	638 mm
Location		inside MAG (between MAG & JET)	outside MAG (between MAG & TOF)
Polar angle	(ϕ-direction)	8 – 172 °	18 – 162 °

pasted. On the inner copper sheets 1.5 mm-wide strips are etched at intervals of 3 mm as field shaping patterns, while outer copper sheets act as ground shields. Onto the outermost surface of the the chamber, a 0.5 mm-thick Aluminum sheet is glued to increase mechanical strength. And furthermore, diamond-shaped vernier pads of 7.5 mm width are also etched on the inner copper sheets at the corresponding period of sense wires i.e. , 100 mm. At the center of each layer of two, sense wires and field wires are laid out by turns at intervals of about 100 mm. As the sense and field wires, gold-plated tungsten-rhenium wires of 25 μmϕ and gold-plated aluminum wires of 250 μmϕ are strung with tensions of 55 gw and 400 gw, respectively. In order to form flat electric fields, a positive potential of 2.7 kV (2.6 kV) is applied to the sense wires of the IDC (ODC), while negative potential of –4.0 kV (–4.5 kV) to the field wires and adequate negative potential to field shapers. Figure 2.14 shows contours of the equipotential and electric field strength of the IDC. Since the IDCs work in the strong magnetic field, the effect of the Lorents force becomes noticeable. The electric fields of IDCs are inclined by 5.5° to the drift direction so as to compensate for the Lorentz angle. The shape of the ODC's electric field is almost the same as the IDC's, with the exception that the Lorentz angle is negligibly small.

Both chambers are filled with the same gas mixture used in the JET chamber (90% CO_2, 10% Ar) because of the same reason as JET chamber.

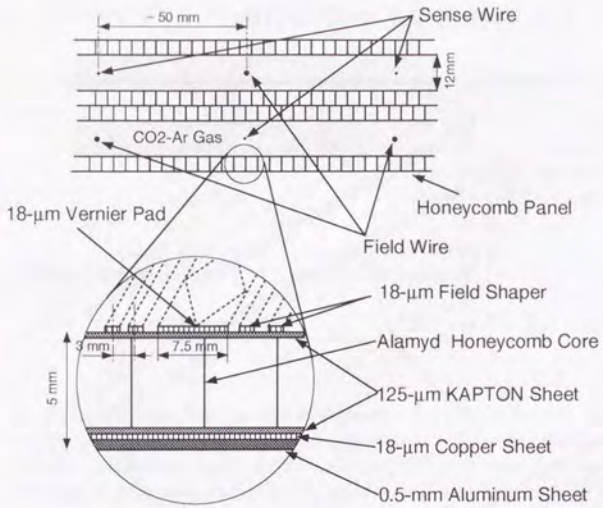

Figure 2.13: Diagram showing a cross-sectional view of the IDC and ODC in $r\phi$ plane.

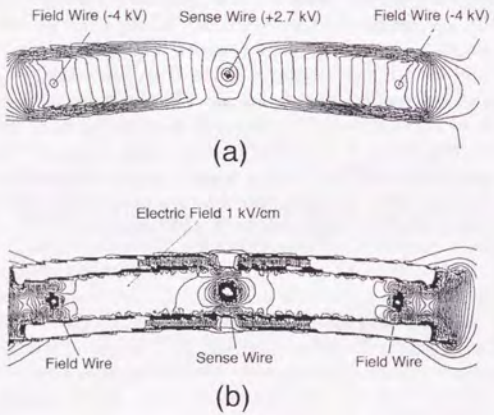

Figure 2.14: (a) Equipotential and (b) electric field strength contours of the IDC.

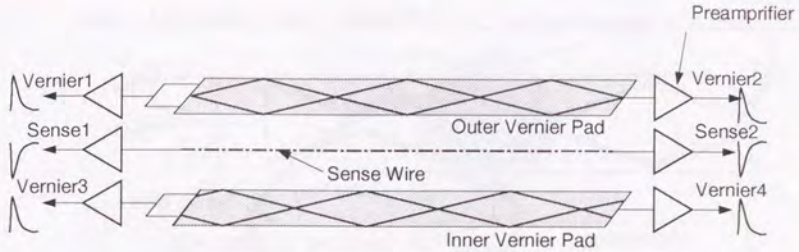

Figure 2.15: Read-out scheme for IDC and ODC signals.

2.4.2 Read-out scheme

The chamber signals from the sense wires and vernier pads are both amplified by preamplifiers mounted on an aluminum plate attached to the end-plate. Figure 2.15 shows a diagram depicting the read-out scheme of the IDC and ODC, where two signals are read from each sense wire, and four from each corresponding pair of vernier pads. Because of limitation of the number of read-out electronics, sense wire signal of IDC is read from one end only. Thus, a total of five or six signals are obtained per IDC or ODC sense wire. In order to achieve the two functions of IDC/ODC, i.e. tracking devices and trigger chambers, these signals are distributed and utilized as follows;

IDC sense wire: IDC sense wire signals are amplified and discriminated among amplifier and discriminator (AMP/DISCRI) modules, and then fed into the coincidence modules. If the two signals from the two nearest wires in outer and inner layers coincide, the discriminated signals are fed to the track trigger (TT) module, which performs a rapid analysis of track character by using the signals not only from IDCs but also from ODCs and generates multiple trigger signals (see Section 2.7.2).

IDC vernier pad: These signals are converted into timing and charge information by 28.5-MHz FADC modules and compressors in the same manner as the signals from the JET sense wires. Hit positions in the $r\phi$ plane and along z-axis are respectively determined using these information.

ODC sense wire: ODC sense wire signals are amplified and discriminated in AMP/DISCRI modules and then fed into the coincidence modules to generate the trigger signal together with the signals from IDC's sense wires. ODC sense wire signals are also fed to the TDC modules which convert their timing into 12-bit digits. This timing information is utilized for determining the hit position in the $r\phi$ plane.

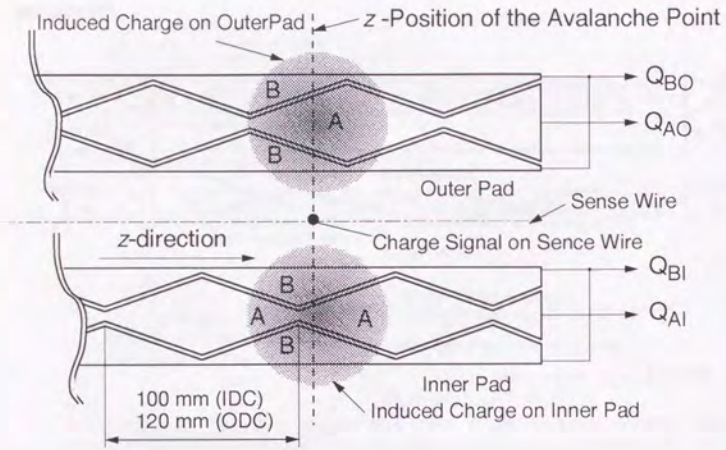

Figure 2.16: Corresponding sets of vernier pads.

ODC vernier pad: ODC vernier signals are processed by the ADC modules which integrate their charge during a 500-ns gate and convert them into 12-bit digits. A hit position in the ODC along the z-axis is determined by using this charge information.

The hit positions of the IDC (ODC) in the $r\phi$ plane are determined using the measured drift time. Briefly, the drift velocity is calibrated using the sum of the drift times of the inner and outer layers of the IDC (ODC), after which the polynomial corrections are applied to minimize errors in the tracks.

The hit position along z-axis is measured using the signals generated on the corresponding sets of vernier pads, i.e. , each pad is situated on the inner and outer KAPTON sheet such that they surround one sense wire. Each set is cut as shown in Figure 2.16, having a cycle of 100 mm for the IDC (120 mm for the ODC). The corresponding set of pads are situated such that one is shifted along z-direction by a quarter cycle with respect to another.

When the drifted electrons avalanche near a sense wire and deposit their charge on it, induced signals are generated on the corresponding set of pads. The charge on each pad is divided into the two parts (A and B) of the pad and the both charge are separately read out. We define the normalized charge ratio of A and B for each pad as:

$$\varepsilon_{\mathrm{I(O)}} = \frac{Q_{\mathrm{AI(O)}} - Q_{\mathrm{BI(O)}}}{Q_{\mathrm{AI(O)}} + Q_{\mathrm{BI(O)}}}$$

where $Q_{\mathrm{AI(O)}}$, $Q_{\mathrm{BI(O)}}$ are the charge on A and B for inner pad (outer pad). Each ε parameter is linearly related to the z-axis position of the avalanche point. Figure 2.17

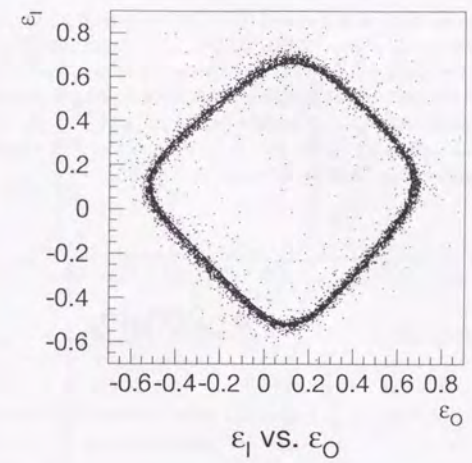

Figure 2.17: Scatter plot of the ε parameter of the inner and outer pad.

shows the scatter plot of the ε parameter. One cycle around the round square locus represents a movement of 100 mm (120 mm) along z-axis. The line in the figure shows the ε_{I} and ε_{O} calculated numerically for various z-position. We can then derive the hit position along the z-coordinate by comparing the measured ε pair to the numerical calculation. The spread of the measured ε values around the numerical line provide the estimation of the z-axis resolution (Fig 2.20).

2.4.3 Performance

The overall resolution of the $r\phi$ plane is estimated to be 200 μm based on the residuals obtained from the fitted track (Figure 2.18). Figure 2.19 shows the IDC's $r\phi$ resolution as a function of the drift distance (a) and the angle of the track trajectory with respect to the axial direction (b), where both resolutions are gradually degraded according to the drift distance and angle.

Once the coarse z-position obtained by the charge division of the JET chamber, absolute z-position can be determined by the precision of 350 μm.

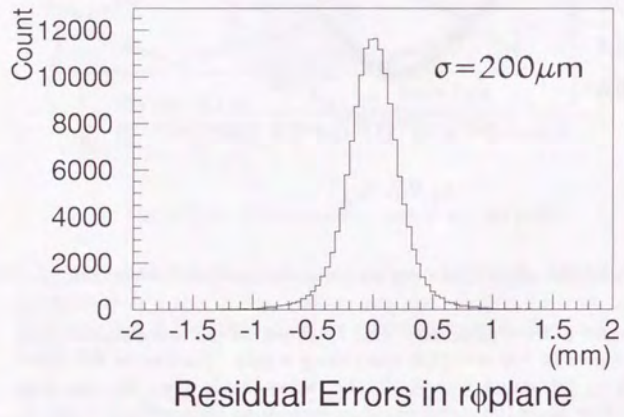

Figure 2.18: Residual distribution of the IDC $r\phi$ hits.

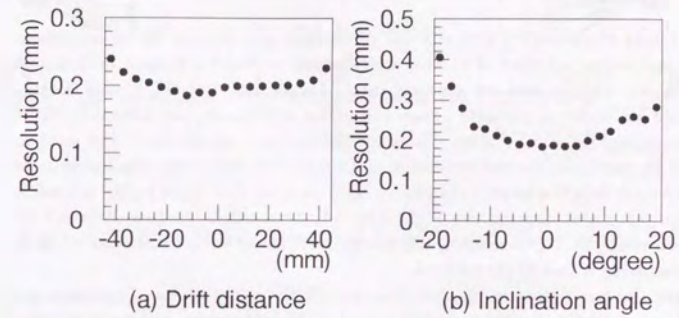

Figure 2.19: IDC $r\phi$ resolution as a function of (a) drift distance, and (b) angle ϕ with respect to the axial direction.

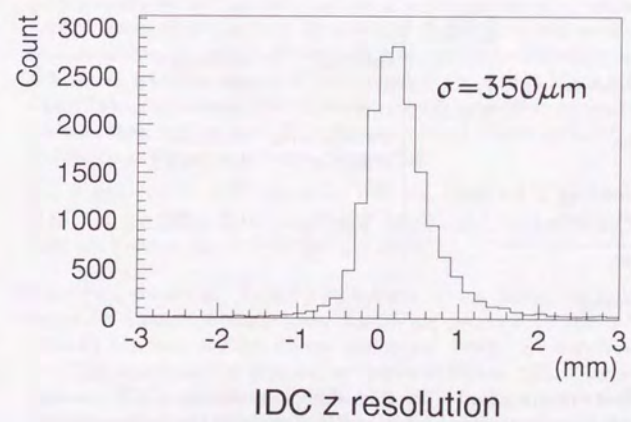

Figure 2.20: Spatial resolution of the z-coordinate measurement in the IDC.

2.5 Time of Flight Hodoscope

2.5.1 Structure

Time of Flight Hodoscope (TOF) is the outermost detector in BESS spectrometer. The hodoscope consists of plastic scintillation counters arranged cylindrically just outside the ODCs, and are grouped into 2 layers, i.e. 'top TOF' and 'bottom TOF'. Once a cosmic ray particle passes through a scintillator, the ionization loss of the energy is converted into light. The scintillation light travels down the scintillator paddle by multiple internal reflection and finally reaches photo-multiplier tubes (PMTs) on each lengthwise end via plastic light guides. This light signal is used for three purposes: (a)measuring the flight time of the incident particle between two scintillation counters, (b)measuring the energy lost inside the scintillation counters, and (c)generating a fast trigger signal.

Between the two flights in '94 and '95, new TOF system replaced previous one. Table 2.4 summarize the main specifications of TOF hodoscope, and each system is expounded below mainly about differences.

Table 2.4: Main specifications of TOF hodoscope.

		'93 & '94	'95
Scintillator	type	NE102A[a]	BC404[b]
	area	110 × 20 cm^2	95 × 10 cm^2
	thickness	2 cm	2 cm
# of counters	Top	4	8
	Bottom	6	12
Position (radius)		660 mm	670 mm
Covering angle (ϕ-direction)	Top	67°	68°
	Bottom	101°	102°
Light guide shape		Twisted strip	Fish tail
PMT type		H2611SXA[c]	H2611SXA
PMT angle to z-axis		60°	0°
Over-all time resolution		300 p sec	100 p sec

[a]Nuclear Instrument
[b]BICRON
[c]Hamamatsu Photonics

In '93 and '94 instrumentation: The time of Flight hodoscope (TOF) has four and six scintillation counters at the top and the bottom of the detector respectively. The NE102A scintillator (NE TECHNOLOGY LIMITED) is adopted, whose long light attenuation length of 2.5 m helps to minimize positional dependency over a long counter. The dimensions of each scintillator paddle are 110 cm × 20 cm × 2 cm. The rectangular surface at the end of the radiator

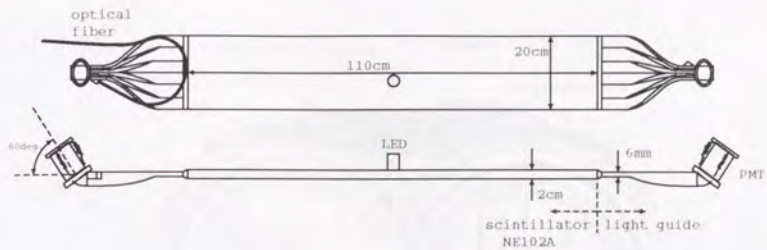

Figure 2.21: Time of flight counter of BESS '93 and '94 instrument.

is imaged onto the photocatode surface by means of bent transparent plastic strips ,twisted-strip light guide. Since the PMTs are operated in the magnetic field of 1.8 kG, where ordinary PMTs can not work, there used magnetic field resistant PMTs, H2611SXA (Hamamatsu photonics), which has 19 stages of proximity fine-mesh type dynodes instead of usual box type. Besides, in order to reduce a deterioration in the performance of the PMT, the axis of it is aligned with the field direction within 15 degrees, or at an angle of 60 degrees to the z-axis. Figure 2.21 shows the schematic view of the single TOF counter. The pretest of PMT in the 1.8 kG reveals that the PMT gain increases by at most 10% and the timing shifts by 100 p sec, however, no degradation in the timing resolution is observed. Various high voltage values between 1.8 kV and 2.3 kV are applied to adjust the gains of all PMTs to the same value. Each counter is wrapped with a 0.1 mm thick aluminized mylar sheet for good light reflections, and then wrapped doubly with 0.1 mm thick black vinyl sheets to shield light from outside and to avoid crosstalk between two adjacent counters. Over-all time resolution of 270 p sec is achieved. These paddles are placed at the radius of 66 cm as shown in Figure 2.22.

For a daily check and calibration use, ere equipped a light-emitting-diode (LED) at the center of the scintillator paddle, and the connector for the laser light are fixed on the side of the light guide.

In '95 instrumentation: In order to achieve better timing resolution, detailed computer simulation study using lay-tracing program GUIDE 7 [16] and repeated beam tests at KEK PS was performed. From the careful investigations, new TOF counters was designed as shown in Figure 2.23. The dimensions of each scintillator paddle are 95 cm × 10 cm × 2 cm, which is half as wide as old paddle and a little shorter. The BC404 scintillator is adopted as a radiating medium. The main advantages of BC404 over NE102A is that the light pulse of the scintillator is intense and short. This faster decay time scintillator provides the smaller amount of time-spread in timing measurement. Some technical data are listed in Table 2.5.

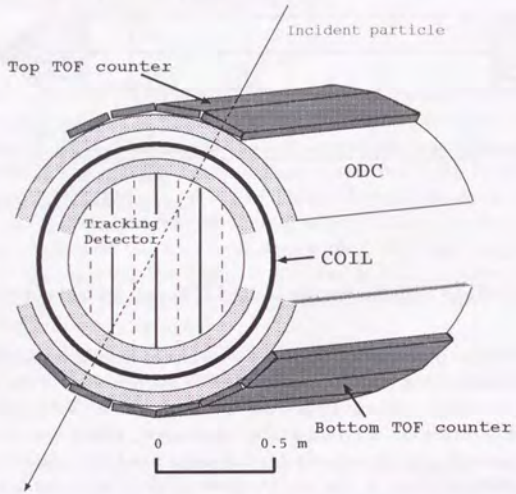

Figure 2.22: Layout of time of flight hodoscope in BESS '93 and '94 instrument.

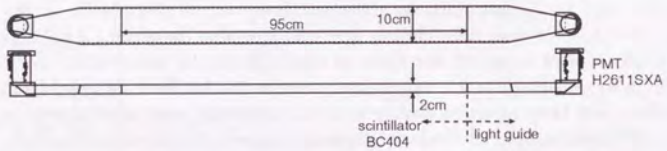

Figure 2.23: Time of flight counter of BESS '95 instrument.

Table 2.5: Main specifications of TOF hodoscope.

	NE102A	BC404
Base	Polyvinyltoluene	Polyvinyltoluene
Density	1.032	1.032
Refractive Index	1.58	1.58
Light Output (% Anthoracene)	65	68
Decay Time	2.4 n sec	1.8 n sec
Pulse Width (FWHM)	2.7 n sec	2.2 n sec
Light Attenuation Length	250 cm	140 cm
Wavelength of Max. Emission	423 nm	408 nm

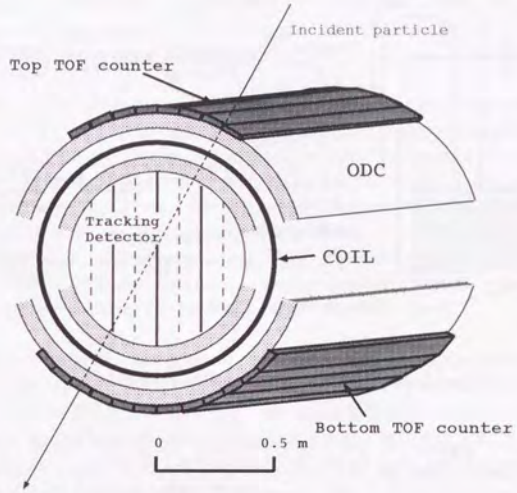

Figure 2.24: Layout of time of flight hodoscope in BESS '95 instrument.

The light guide is changed to fish-tail types from twisted-strip, and now the axis of PMTs is parallel to the flux line of the magnetic field and perpendicular to the lengthwise direction of the counter. The same types of photomultipier as '93 and '94 instrumentation, i.e. H2611SXA are employed again. Appropriate high voltage values between 1.6 kV and 2.1 kV are applied to the PMTs to adjust the gains of all PMTs. The scintillator part of a new TOF paddle is wrapped with white reflector of Millipore sheet and the light guides at both ends are enveloped in one layer of aluminized mylar to realize good efficiency of light reflection. Furthermore, a part of the light guide nearest the PMT is covered with one layer of silvered mylar. And then the entire counter is wrapped doubly with 0.1mm thick black vinyl sheets like the old TOF counters. Over-all time resolution of 110 p sec is achieved. Eight counters for the top and twelve counters for bottom are used as shown in Figure 2.24.

2.5.2 Read-out scheme

Each PMT outputs three signals, witch are extracted separately from the anode, 19th dynode, and 18th dynode, to avoid interference among them. As shown in Figure 2.25), these three signal are utilized for three different purposes, i.e. a timing measurement, a fast trigger and a charge measurement. Each signals are processed in the following ways:

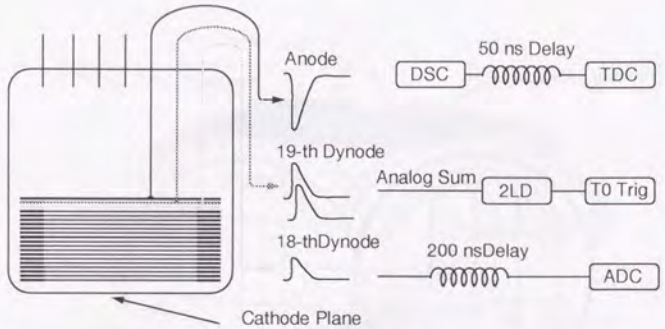

Figure 2.25: Read-out scheme PMT signals

Anode: The anode signals are used for generating the STOP signal in the timing measurement. They are discriminated by a CAMAC discriminator (DSC) module and fed into the START inputs of CAMAC time-to-digital converter (TDC) through a 50-n sec delay cable. The DSC module offers a variable threshold level as low as -5 mV, which can be programmed in 0.23 mV step remotely via CAMAC command . The threshold level is set to -10 mV ('93) and 15 mV ('94 and '95), which realizes good timing resolution with a good reduction in the probability of spurious output signal due to noise of the electronics. Modified versions of commercial TDC (Lecroy 2208) are utilized for '93 and '94 with 50 psec bin width and 11-bit range. In '95 custom-made low-power TDC with 25 psec bin width was introduced along with the new TOF hodoscope. Since inductive parts are used in the oscillator circuit, the timing conversion gain is shifted by 2.5% in the actual operating field, but there is no effect on TDC resolution and linearity. The timing resolution of 70 p sec and the integral non-linearity of 0.1% at maximum to full scale are measured by the pulser tests.

19-th dynode: The 19-th dynode signals are used for generating a first level trigger signal. Two signals from a pair of PMTs viewing the same counter are sumed up after integration with time constant of 20 n sec to reduce the position dependence of the signal amplitude. Then the summed signals are fed into the two-level discriminator (2LD) modules, which has a capability of setting two thresholds for each channels. One threshold is set to 30 mV, which corresponds to 30 % of the minimum ionizing pulses and is called 'low-threshold (LOW)'. The other is set to 150 mV ('93) and 160 $\sim$ 250 mV ('94 and '95) for the multiple charged particles, which is called 'high-threshold (HIGH)'. Combining the information of thresholds and of the position of hit counter (top or bottom), four categories of signals ere generated , i.e. top LOW, top HIGH, bottom LOW and bottom HIGH. The resultant four signals are fed into the T0 trigger module to initiate a fast trigger pulse including the START signal for TDC. Detailed trigger scheme will be described later in Section2.7.

18-th dynode: The 18-th dynode signals are utilized for the charge measurement. They are fed to a integrating-type Analog-to-Digital Converter (ADC) module through a 200 n sec analog delay line, and are integrated during the gate width of 250 n sec. The input sensitivity of the ADC is 0.6 pC/count for a dynamic range of 12-bits with ± 1 count integral-linearity. The ADC range corresponds to the 100 times of the average charge expected from the minimum ionizing particles vertically incident. The intrinsic resolution of the charge measurement is 10% for minimum ionizing particles, which is dominated by photo-electron statistics in the PMT.

The gain and timing of each counter were calibrated using the test beams from the proton synchrotron at KEK before the installation. Protons and pions with 1 GeV/c was used to determine the high-voltage applied to each counter and parameters for a time-walk correction. After installation into the BESS instrument, the gain and the timing are monitored and calibrated both on the ground and in the flight situation by following three ways:

1. The laser light pulsar (Hamamatsu PLP-02) is used for the precise measurement of the TDC conversion gain and timing offset for each counter in the actual operating condition. The output light has a wave length of 410 nm and is led into the counter through a 1-mm-diameter quartz fiber. The excellent stability of the pulse height and the timing of laser pulse enable to calibrate the timing and gain of each counter, though this calibration scheme is not available when the end-cap is closed.

2. The blue LED light is also used to monitor the gain and timing of the counters. Although LED signals have slower rise-time and less stability than the laser signals, there are two advantages in the calibration with the LED. Calibration can be performed even after the pressure vessel closed. PMTs at both ends are simultaneously calibrated and the their gain can be relatively adjusted.

3. In the flight situation, cosmic-rays are used to determine all calibration parameters used in the off-line analysis. In order to avoid fluctuations of the gain and the timing according to the temperature changing during the flight, the flight data is divided into several RUNs and calibrate them in the individual run.

Detailed study and cross-checks among the above three methods in '93 and '94 revealed that all the monitoring and calibration can be performed using cosmic rays both on the ground and in the flight situation. Therefore calibration in '95 are performed by using cosmic rays.

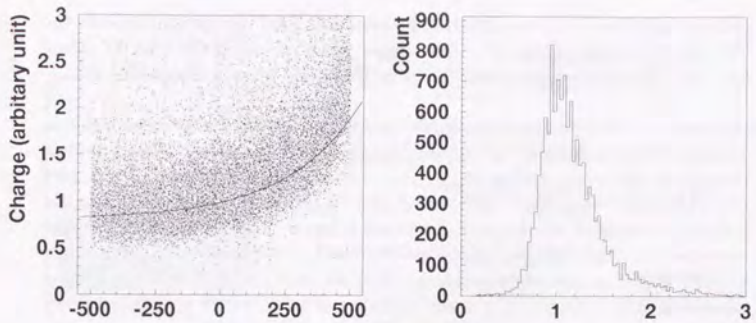

Figure 2.26: (a) z-position dependence of the PMT charge measured. (b) Charge distribution at the center of the counter ($z = 0$) ('93).

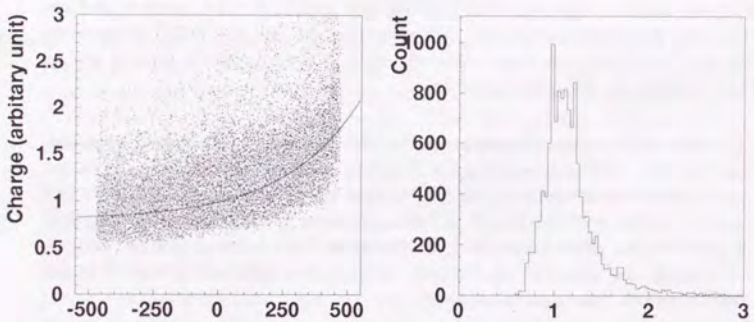

Figure 2.27: (a) z-position dependence of the PMT charge measured. (b) Charge distribution at the center of the counter ($z = 0$) ('95).

2.5.3 Performance

Figure 2.26 and 2.27 show the distributions of the PMT charge (ADC values) for two types of TOF hodoscopes measured by the proton samples with rigidity more than 3 GV. Left-side figures show z-dependence of the charge on which the fitted curve using equation $a + be^{cz}$ (a,b, and c are parameters) is superimposed. Right-hand figures show the charge distribution at z =0. The charge resolution determined from the distribution below the peak is about 10% (6%) at the center of the counter, which means that about forty (one-hundred-twenty) photo-electrons are obtained for relativistic protons in '93 and '94 ('95).

Figure 2.28 and 2.30 show the residuals of measured Time Of Flight from the expected one for proton and helium sample in '93 and '95 flight data. These are

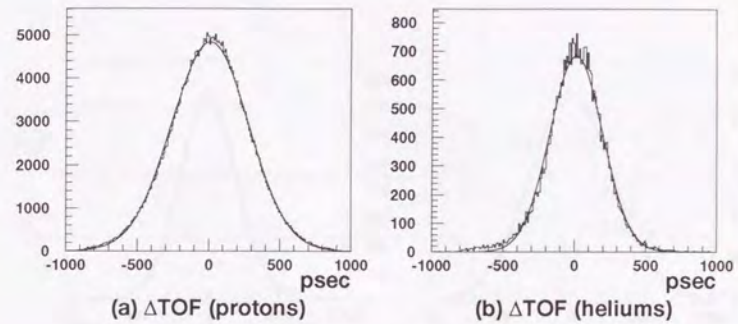

Figure 2.28: ΔTOF (a) for proton sample and (b) for helium sample ('93).

calculated by following equation.

$$\Delta\text{TOF} = \text{TOF(directly measured)} - \text{(path length)/velocity} \quad (2.1)$$

$$\text{velocity} = c(p/E) \quad (2.2)$$

where c is the light velocity, p is the measured momentum, and E is the energy calculated from equation $E = \sqrt{p^2 + \text{mass}^2}$. The curves in the figure are the results of Gaussian fit. For helium sample the rigidity region is restricted in greater then 7 GV in order to decrease the effect of ^{3}He mixing, although there still exists a slight discrepancy from the Gaussian in negative region. The resultant sigmas for '93 ('95) flight data are 270 ps (110 ps) for the proton sample and 190 ps (100 ps) for the helium sample, respectively.

The performance of the TOF hodoscope is summarized in Table 2.6

Table 2.6: Performance of TOF hodoscope.

		'93 & '94	'95
# of photo-electron	(for proton)	40	120
Charge resolution	(for proton)	10%	6%
Time resolution	(for proton)	270 p sec	110 p sec
Time resolution	(for helium)	190 p sec	100 p sec

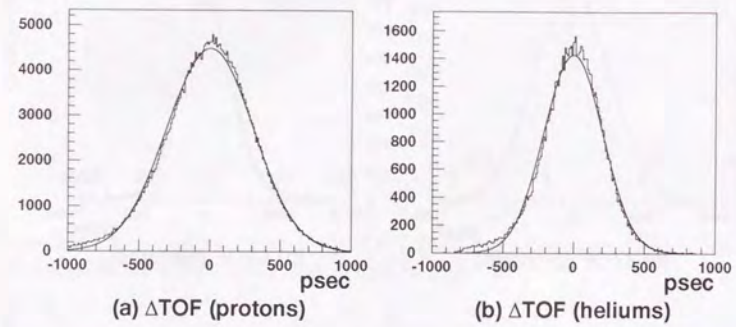

Figure 2.29: ΔTOF (a) for proton sample and (b) for helium sample ('94).

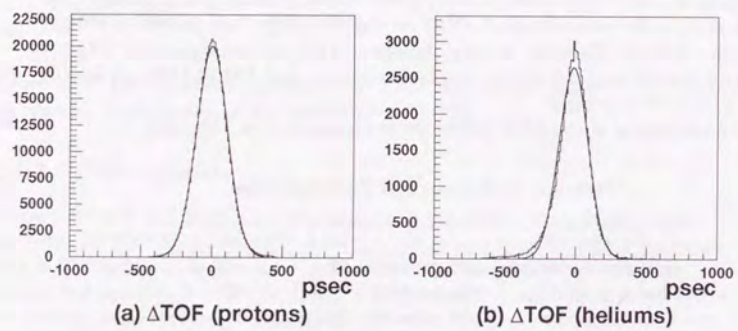

Figure 2.30: ΔTOF (a) for proton sample and (b) for helium sample ('95).

2.6 Čerenkov counter

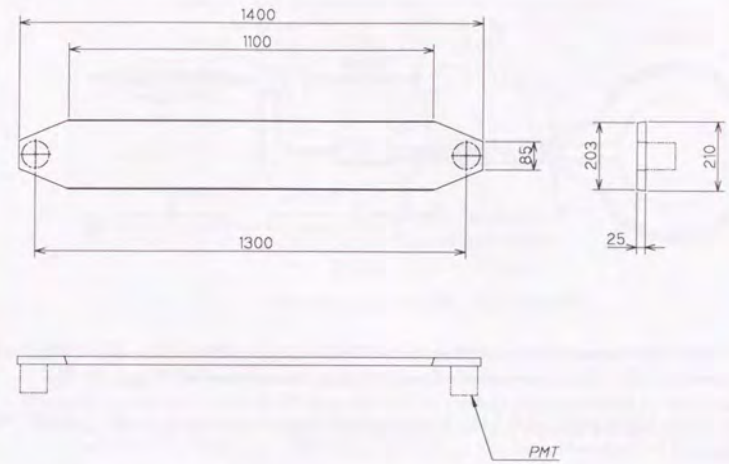

Figure 2.31: Čerenkov counter of BESS instrument.

Čerenkov counter is a so called particle identifier, which can be dispensed with, but will grately help to identify the particle at some energy range.

Čerenkov counter is originally designed in order to discriminate $\bar{p}$ from π^-, μ^- or electron up to around 1 GeV. Figure 2.31 shows a schematic view of a Čerenkov counter. Its dimensions are 1400 mm × 210 mm × 25 mm with a fiducial area of 1400 mm × 210 mm. UVT acrylic plastic with refractive index $n = 1.52$ is used as a radiator and is wrapped in white diffusive reflector of Millipore sheets for a good efficiency of light reflection. Each counter is viewed on both ends by a fine-mesh type PMT (Hamamatsu R5542S), which is the same type PMT as used for TOF except for a larger photocathod area of 64 mmϕ. Originally, the pressure vessel of BESS '94 instrument was not designed to carry Čerenkov counter inside. In a result, it was installed outside to be operated in vacuum. Three paddles of Čerenkov counter were arranged cylindrically around the vessel at a radius of 820 mm. In BESS '95 instrument, the pressure vessel was extended so that the Čerenkov counter was installed inside. In a result, the counter was arranged much closer to the the bottom TOF counter, where no more aluminum vessel wall of 2-mm thickness inside which cosmic ray particle may interact.

The refractive index $n = 1.52$ leads to the threshold momenta of 0.82 GeV/c for proton/antiproton. The Čerenkov counter was utilized for antiproton identification.

In future, the Čerenkov counters combined with a lead plate of a few radiation length thick will be helpful for electron/positron identification.

2.7 Trigger

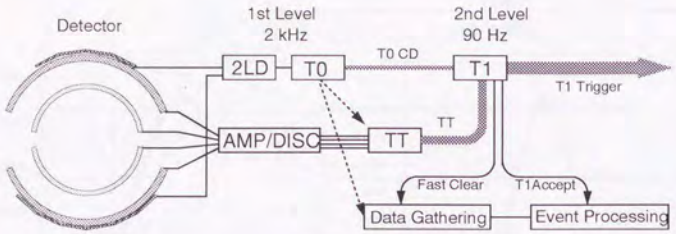

Figure 2.32: BESS trigger scheme

Because of a large geometrical acceptance, a primary trigger rate of the BESS detector exceeds 2 kHz. This is far above the maximum storage rate of about 200 Hz. The main part of BESS trigger system in '93, '94 and '95 is tuned up to a primary objective to search for anti-proton and anti-helium while rejecting most of proton and helium.

The trigger system consists of two levels (Figure 2.32). The first level is a fast "T0 trigger" where the combined signal of the top and the bottom scintillators initiates data acquisition cycle. The second level is a "T1 Trigger" where event reduction is performed through a "track trigger" (TT) or "count down" (CD) logic. The TT scheme selects preferably negative-charged particles judging from the chamber hit pattern, while the CD logic simply reduces the event rate by the preset ratio (1/140 for '93, 1/60,1/120 for '94 and 1/90 for '95) irrespective of the event configuration. The CD trigger therefore provides an unbiased sample of the T0 trigger, which can be utilized in determining the TT efficiency. In this thesis, the analysis is narrowed down to CD trigger events. If the event is judged to be accepted by either the TT or CD logic, the T1 trigger approves further data processing. Otherwise the data acquisition cycle is discontinued and all electronics are cleared for the next cycle.

2.7.1 T0 Trigger

A "T0 Trigger" is the first level trigger generated by a CAMAC T0 trigger module, which is the primal process of data handling. The T0 trigger module has five signal inputs for "TOF Top LOW", "TOF Top HIGH", "TOF Bottom LOW", "TOF Bottom HIGH" and "External Clock". As described in section 2.5, 2LD modules are employed to generate above four TOF signals. When a single (multiple) charge particle passed through one of the top (bottom) TOF scintillation counter, "Top (Bottom) Low (High)" signal is output. The T0 trigger module ensure that specific combinations of above five input signals have occured and generate four modes of T0 trigger signals, i.e. "T0 Low", "T0 High", "T0 gamma" and "T0 external". Each of them plays following roles:

Table 2.7: T0 trigger logic.

	Top		Bottom		External
T0 Mode	Low	High	Low	High	Clock
T0 Low	1	*	1	*	*
T0 High	*	1	*	1	*
T0 gamma	0	0	1	*	*
T0 external	*	*	*	*	1

1 : Signal should be asserted.
0 : Signal should be negated.
* : Signal is not concerned.

T0 Low: This mode aims for single-charged particles. It requires that both top and bottom TOF scintillator signals exceed the low threshold of the 2LD.

T0 High: This mode aims for multiple charged particles. It requires that both top and bottom TOF scintillator signals exceed the high threshold of the 2LD.

T0 gamma: This mode aims for gamma rays. Gamma-rays can be detected when they are converted to e^+e^- pair at the upper part of the MAG. To accept the events with such a configuration, this mode requires that there is null hit in top scintillators and at least one hit in bottom scintillators.

T0 external: This mode is generated synchronously by the external clock pulse. It is only used for the calibration.

Table 2.7 summarize the T0 trigger logic.

Logical-OR signal of those four modes initiates data gathering and the track trigger process. The T0 trigger module then locks out the further trigger process until the data acquisition cycle is completed.

The T0 trigger module is equipped with the CD logic for all modes to reduce the trigger rate unconditionally. If the count down number N_{cd} is set for a certain mode, trigger output comes once every N_{cd}. In all science flights, a countdown number of 256 was selected for the "T0 gamma" mode to reduce the event rate from 20 kHz to 80 Hz. And for "T0 Low" and "To High", the count down number is unity to accept all events at this level.

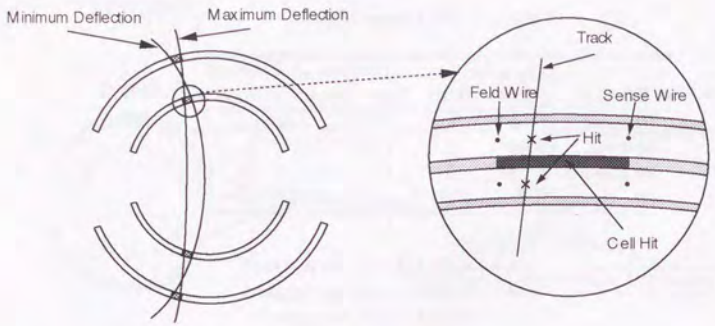

Figure 2.33: Basic scheme the track trigger

2.7.2 Track Trigger

The Track Trigger module generates a specific 8-bits TT data word in response to the hit pattern of IDCs and ODCs. Fig 2.33 shows the basic concept of the TT.

First every signal from sense wire of IDC and ODC is discriminated and then judged whether two signals from the two nearest wires in different two layers happened coincidently or not. If the coincidence is approved, a "hit-cell" signal is generated. Requiring the coincidence in both layers helps to eliminate spurious hits caused by electronics noise or local radio-active sources. 30 and 22 cell-hit signals are generated in total for each ODC and IDC, respectively. The TT module has a fast look-up table ,in which the patterns of "interesting signals" are prescribed, and realizes pre-programmed response to the "hit-cell" signals in two stages; hit-pattern selection and deflection ($\equiv$rigidity^{-1}) selection as follows:

hit-pattern selection

A "number of hits generator" shown in Figure 2.34 calculates the total number of hit-cells for each chamber and puts a certain mark on the "hit-cell" signal. The certain mark is a "hit-cell pattern" which is expressed by a series four integers like (1123). Each integer means the number of hit-cells in the upper ODC (ODC1), upper IDC (IDC1), lower IDC (IDC2), and lower ODC (ODC2) respectively. The hit-cell patterns are divided into the following eight modes:

Mode 1: $\bar{p}$–clear — A mode to select anti-protons. The numbers of hit cells in the four drift chambers are strictly limited.

Mode 2: $\bar{p}$–dirty — A mode to select anti-protons. The numbers of hit cells in the four drift chambers are less limited.

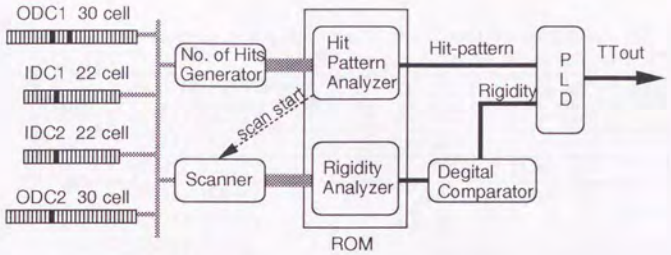

Figure 2.34: Block diagram of TT process.

Mode 3: $\bar{He}$–clear — A mode to select anti-heliums. The numbers of hit cells in the four drift chambers are strictly limited.

Mode 4: $\bar{He}$–dirty — A mode to select anti-heliums. The numbers of hit cells in the four drift chambers are less restricted.

Mode 5: Missing — A mode to select negatively charged particles with only three hit cells in four chambers. The chambers have some 'dead' region near the sense wires for the signals of the hits near the wires are fed into the electronics earlier than the trigger activates them. The events of negatively charged particles with such a 'missing hit' can be selected here.

Mode 6: Multi-clear — A mode to select negatively charged particles which could not selected the modes above. This time extra hits due to noise or interactions are considered.

Mode 7: Multi-dirty — The same as Mode 6. The number of extra hits are less restricted.

Mode 8: Gamma — A mode to select gamma-ray events in which the incident gamma-ray is converted into a electron-positron pair, making hits in two IDCs and the bottom ODC.

The number of hits generator feeds the hit-pattern into a "hit-pattern analyzer". The hit-pattern analyzer scans a "Trigger Mode table" stored in a half of a 2-M byte read-only memory (ROM), and checks if the hit-pattern agrees with same of the table contents. The contents of the trigger mode table are acceptable hit-patterns for each mode as shown in Table 2.8. In this stage, the hit-cell signals with too few or too many hit cells are discarded, and most of the events with shower particles or no tracks in JET chamber are rejected.

Table 2.8: The conditions of the Track Trigger hit-pattern selection. Suffix "p" means that a permutation of these numbers is allowed.

Mode	Category	BESS-93	BESS-94 & 95
1	$\bar{p}$-clear	(1111)	(1111), (1112)
2	$\bar{p}$-dirty	$(1112)_p$	(1113), (1122)
3	$\bar{He}$-clear	(1111)	(1111), (1112)
4	$\bar{He}$-dirty	$(1112)_p$	(1113), (1122) (1123), (1222) (1223), (2222) (1133)
5	Missing	$(0111)_p$	(1111), (1112)
6	Multi-clear	(111i), (i=3,4) (112j), (j=2,3,4)	$(11ij)_p$, (i,j=1,2,3,4)
7	Multi-dirty	$(2ijk)_p$, (i=1,2) (j=1,2,3), (k=1,2,3,4) except for $(2111)_p$	—
8	Gamma	(0ijk) (i,j,k=1,2)	$0(ijk)_p$ (i,j,k=1,2)

deflection selection

The events that have passed through the hit-pattern selection are then subject to the deflection selection. If the hit-pattern is accepted, a "scan-start" signal is sent to the scanner to initiate the deflection analysis (Figure 2.34). The hit-cell signals gives coarse position information with precision of a cell size, i.e. , about 50 mm, and a combination of three or four hit-cell positions enables to estimate a rigidity of the track roughly. The two tracks in Figure 2.33 illustrate the maximum and the minimum possible deflection for a certain combination of hit-cells. A mean value of these two deflections is defined as "deflection for the hit-cell combination". All possible combinations of hit-cells are scanned and fed to the rigidity analyzer, which is the other half of the ROM look-up table. By calculating the deflection for all hit-cell combinations and storing them in the look-up table beforehand, a quick rigidity analysis is possible without any time-consuming calculation. The output deflection is digitally compared to the seven threshold values, each of which corresponds to the hit-pattern category, except that the thresholds for Multi-clear and Multi-dirty are common. If the deflection is above some of the thresholds, i.e., the track has more negative deflection than the threshold, TT signals are generated. The resultant eight signals are fed into the T1 trigger module to be combined with charge information from the TOF.

Figure 2.35 shows the efficiency of the rigidity selection as a function of deflection calculated by the simulation. The threshold values indicate the deflections where the efficiency become 50%. The left figure is for the threshold used for the $\bar{p}$ selection in the '93 flight. The right figure is for the threshold used for an anti-helium selection. The curve for the $\bar{p}$ selection is set being shifted to the negative direction compared

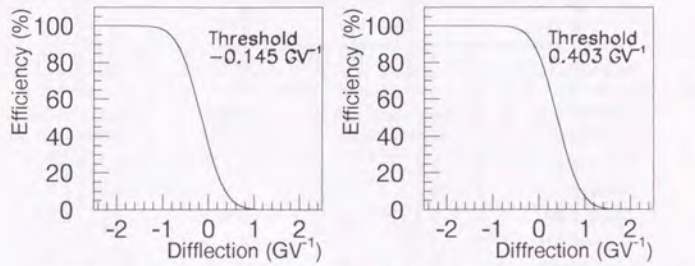

(a) Efficiency for antiprotons (b) Efficiency for antiheliums

Figure 2.35: Track trigger efficiency (a) for an $\bar{p}$ search (b) for an anti-helium search.

to that for the anti-helium selection because a large number of protons should be cut more tightly by the rigidity selection.

2.7.3 T1 Trigger and Fast Clear

The TT only concerns the number of hit-cells and the deflection of the track. The T1 trigger module combines the charge information from the T0 trigger module and the track information from the TT module in order to output trigger signals "biased" toward negative charged particles. In one-to-one correspondence to four modes of T0 trigger signals, the T1 trigger module also generates four sorts of "unbiased" trigger signals; "T0 Low CD", "T0 High CD", "T0 Gamma CD" and "T0 External CD". These signals bypass the TT selection but undergo a CD logic as is done in the T0 trigger module. In total, twelve kinds of trigger signals are generated as shown in Table 2.9. It is recorded as a "trigger bits" event by event which kind of trigger signal is generated. Finally, as a Logical-OR signal of these twelve signals, the T1 trigger module outputs "T1 Trigger" which permits the data to be recorded.

If no T1 trigger signal is generated, a fast clear signal is sent to a "fast clear" module and is distributed to all FADC and CAMAC modules to allow all the digitizers to stop the cycle and to be cleared.

And the T1 trigger module end up its task by unlocking the T0 trigger module to accept the next event.

Table 2.9: T0 trigger logic.

	T1 Mode	T0 Low	T0 High	T0 Gamma	T0 Ext.	TT	CD
Biased	$\bar{p}$-clear	1	*	*	*	1	1
	$\bar{p}$-dirty	1	*	*	*	1	1
	He-clear	*	1	*	*	1	1
	He-dirty	*	1	*	*	1	1
	Missing	1	1	*	*	1	1
	Multi-clear	1	1	*	*	1	1
	Multi-dirty	1	1	*	*	1	1
	Gamma	*	*	1	*	1	1
Unbiased	T0 Low CD	1	*	*	*	*	1
	T0 High CD	*	1	*	*	*	1
	T0 gamma CD	*	*	1	*	*	1
	T0 external CD	*	*	*	1	*	1

1 : Signal should be asserted.
0 : Signal should be negated.
* : Signal is not concerned.

2.8 Data Acquisition System

Because of a large geometrical acceptance, a T0 trigger rate amounts to about 2kHz. And a large number of readout signals makes event data size large, about 1.2k bytes per event on average. The data acquisition system equipped for BESS is required to handle these data efficiently. Another requirement imposed on the BESS data acquisition system (DAQ) is to reduce its power consumption. A larger power consumption demands more batteries resulting in a smaller margin of the weight suspended from a balloon, or shortens the exposure time of the experiment. It also produces a larger amount of heat in the instrument, which may cause damage to its detector or electronics and cause a cooling problem. In order to overcome the above problems, the BESS DAQ system is specialized for this balloon-borne experiment and most of the electronics are custom-made to manage both minimizing power consumption and keeping the processing speed fast. Figure 2.36 shows a general scheme of the BESS DAQ. Four subsystems, i.e. , event-process subsystem, data-storage subsystem, monitoring subsystem, and communication subsystem, function for individual purposes. All the subsystems are linked with each other by a serial bus line composing a local network based on Corvus Omni-net protocol. A multi-processor and pipe-line scheme enable the DAQ system to manage the event rate of 1 kHz and to store the data up to 10G bytes with a recording rate of 500k bytes/s. In following sections, each component is described in detail.

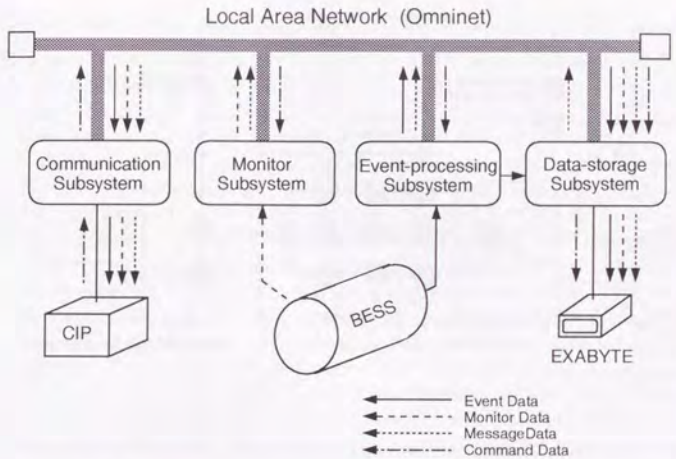

Figure 2.36: Schematic diagram of the data acquisition system

2.8.1 Event-Process Subsystem

Figure 2.37 shows a block diagram of the Event-Process Subsystem. The shadowed boxes stand for transputers (INMOS Ltd.). The Event-Process Subsystem, composed of FADC, CAMAC, event builder (EVB), and transputer bank, networks twenty transputers in total. Each transputer has a processing speed of 20 MIPS and all the processors are mutually connected via four point-to-point serial links equipped in each transputer which have maximum transmitting rate of 1 M byte/s. The data transmission by point-to-point links has an advantage that no arbitration method is needed. It makes a special feature of using multi transuputers, all of which work concurrently and cooperatively to realize a fast event processing. A parallel processing is achieved in this multi-transputer system, so any commands can be received or issued while gathering or recording event data.

CAMAC

All the CAMAC instrument modules are housed in two CAMAC crates. Each crate is controlled by an intelligent crate controller having a built-in transputer [17]. Thanks to the transputer's architecture, those two crate controllers are networked by connecting the serial links. Individual crate controllers control front-end CAMAC modules, operate in parallel, and interpret or issue commands. The data digitized at the CAMAC modules in two crates are read concurrently and autonomously.

In the crates, the following modules are installed.

- TOF read-out electronics; Discriminators, TDCs, and ADCs

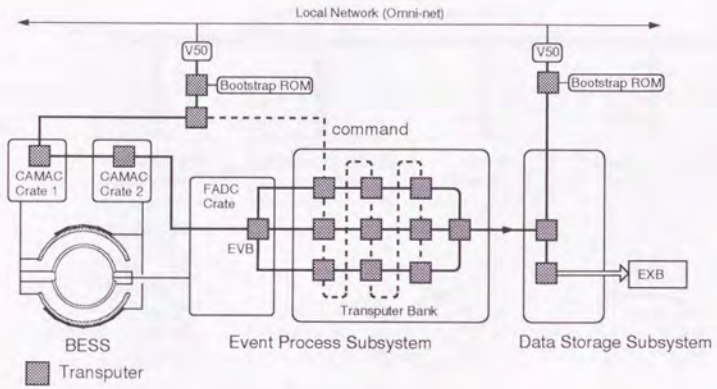

Figure 2.37: The block diagram of the Data Process and the Data Storage subsystem. A net work of transputers are constructed for the main function of the subsystems.

Signals from TOF counters are converted to logic pulses to digitize them into timing and charge information.

- ODC read-out electronics; Discriminators, TDCs, and ADCs
  These modules digitize the signal from ODCs.
- Trigger modules; Discriminators, T0, TT and T1 modules
  Trigger parameters such as CD numbers or TT thresholds are programmed and monitored remotely via CAMAC commands.
- 24-bit scalars
  Two 12-channel 24-channel scalars are installed to count the various triggers. These numbers are used to monitor the trigger status and to evaluate trigger efficiencies.
- Event-timing module
  An event-timing module includes a milli-second clock and measure the event-timing with 0.1-ms precision.
- Gate generators
  Gate generators are passive modules, i.e. , not controlled by CAMAC. They generate the pulses with adequate widths and delays for use in other modules such as ADCs or TDCs.

The size of CAMAC data per one event amounts to about 300 bytes. All data from above modules are transmitted to the network where they are merged into the event structure (event-building process).

FADC

FADC system is comprised of a crate controller, FADC modules, and a compressor module installed in a triple-height VME crate. The FADC modules read signals from sense wires of JET chamber and vernier pads of IDCs. Each FADC module has sixteen inputs and fifteen (sixteen) FADC modules are installed in '93 ('94 and '95) flight. The FADC system is capable of simultaneously digitizing total 240 (256) waveforms of chamber signals into 8-bit data at the sampling frequency of 28.5 MHz with a record length of 512 samples. The digitized data are accumulated in the fast-in-fast-out (FIFO) memories after the treatment with real-time zero-suppression process. The compressor module successively reads FIFOs, squeezes the accumulated data into a 8-byte formated string and write them to another FIFOs on the compressor module. In this data compression sequence, the data size is reduced by a factor of 3 within 200 μsec. The FADC and compressor modules are controlled by transputers. If the crate controller receives the T1 trigger signals, the transputer transfers the data from the FIFOs to the Event Builder via the internal memory bus, since the Event Builder is a process running in the transputer on the FADC crate controller. Otherwise when a fast clear signal is received, then all modules are reset to be ready for next digitizing process. The FADC data amounts to about 700-900 bytes per an event.

Event Builder (EVB)

The data collected concurrently and autonomously in the two CAMAC crates and the FADC crate are transferred to the Event Builder via the serial links and the internal memory bus respectively. The Event Builder gathers all the data, and merges them into the event frame. The event building process completes within 1.2 ms from the T0 trigger for one typical event data of 1.0-1.2 kbytes. The event-building processes can be executed in parallel with the data-gathering process, which are controlled independently by the CAMAC and FADC crate-controller. After packing the data, the Event Builder clears the CAMAC and FADC modules using the Fast Clear circuit to prepare for the next event. Then, one of three data transferring processes running on a transputer sends the event frame to the transputer bank through the corresponding serial link for further processing.

Transputer Bank

The main role of the transputer bank is to clean up and sieve the event data using the whole detector information. There arranged nine transputers in a three-by-three matrix way, and the identical process is running in each. The event frame sent from the EVB flows through the transputer bank from the up-stream to the down-stream. In case the up-stream transputer is busy, the event data is passed to the down-stream transputer in sequence. In this way, up to nine event frames can be processed at the same time. A filtering process removes the so called junk events, which suffer inconsistency between the positions of hits in ODC and TOF, and/or have too much or null hits in JET chamber and IDC. In this process, also removed

the overflowed TDC data which do not contain hit informations to reduce the event data size. About 2% of the events were classified into this category to be removed. The whole process completes within at most 20 ms and the transputer bank can handle 450 events per second. Finally, the filtered data are sent to communication and data storage subsystem to be transmitted to a ground station or recorded in a magnetic tape.

In addition to the filtering process itself, one of the transputer makes various histograms concerning these processes. The resultant histograms are sent to the ground together with CAMAC scalar data in a second interval. These histograms are utilized to watch the status of the triggers and event filtering.

2.8.2 Monitor Subsystem

A monitor subsystem has two components; a digitizing module. and a controller module governed by a NEC V40 (μPD70208) CPU constructed in a STD-bus crate. This subsystem handles the house-keeping data from the sensors. The digitizing module has 64 individual inputs. Each channel has a differential-amplifier and one analog-to-digital converter is employed to digitize all the sensor signals. Measured points are temperatures (16 points), pressures (10 points), a magnet status (16 points), a chamber high voltage status (10 points), and solar sensors and clinometers. The digitized data are sent to the communication subsystem as telemetry data, and to the Data storage subsystem so as to be recorded in the magnetic tapes.

2.8.3 Communication Subsystem

The Communication subsystem is constructed in a STD-bus crate and controlled by a NEC V40 (μPD70208) CPU. It interfaces the command/telemetry device (CIP) with the Omni-net bus to manage communication between the ground station and the payload. Once a command is transmitted from the ground station to the payload, it is received by CIP, where the command is converted into a 16-bit data words, and is distributed to each subsystems by the communication subsystem. The command words are sent at a rate of 1 word/sec. On the other hand, the telemetry data gathered by the communication subsystem via the Omni-net, such as sampled event data, monitor data and messages, are fed to the CIP and then sent to the ground station over a radio link. The capacity of the transmission is 10 k byte/sec.

2.8.4 Data-Storage Subsystem

All the processed data are sent to the data-storage subsystem and recorded into magnetic tapes.

The monitor- and the message-data are transferred via Omni-net. A NEC V50 (μPD70216) CPU is employed for this communication. While the event-data are gathered via three of four serial links equipped in a transputer, which networks the event-process subsystem and the data-storage subsystem. Transputer modules are employed for the main tasks of the data storage, one of which was a module

specialized for the SCSI bus control. Two EXABYTE EXB-8500 (8505) 8mm tape recorders are employed as the storage devices in '93 ('94 and '95). The capacity of the tapes is 5 Gbytes each, providing 10 Gbytes of storage capacity in two tapes. The maximum data recording speed was 500 kbytes/s.

2.9 Overall Performance

The overall quality of the BESS detector performance can be checked using the events that passed the event selection.

2.9.1 Rigidity Spectrometer

The fitting errors of the rigidity measurement were obtained in the final combined $r\phi$-fitting process. Figure 2.38 and 2.39 shows the fitting error of the $1/R_t$. In Figure 2.38 the area of box corresponds to the number of events, and the histograms in Figure 2.39 are the projection onto y axis around 1 GV, 3 GV, 10 GV and above 10 GV. All the histograms have a clear peak around $\Delta(1/R_t) \sim 0.05$. and it is almost constant in the entire rigidity range. According to the following relation,

$$\Delta\left(\frac{1}{R_t}\right) = \frac{\Delta(R_t)}{R_t^2} = \frac{\Delta(R_t)}{R_t}\frac{1}{R_t},$$

the $\Delta(1/R_t)$ is decomposed into fractional errors of rigidity ($\Delta(R_t)/R_t$) and inverse rigidity ($1/R_t$). The value of 0.005 thus indicates the particles with the transverse rigidity of up to 200 GV are at least 1σ away from the particles with the opposite charge.

2.9.2 Time of Flight System

The performance of the TOF system was examined using the measured rigidity of the incident particle.

TOF measurement

Figure 2.40 shows the distribution of $1/\beta$ around 0.9 GV. Since $1/\beta$ is related to $(m/Q)^2$, light particle (e, μ, π), proton and deutron/Helium are clearly separated. The standard deviation of $1/\beta$ distribution for proton is about 0.06 in '93/'94 data and 0.03 in '95.

dE/dx measurement

Figure 2.41 shows the distributions of measured dE/dx for protons at the top (left half) and bottom (right half) TOF scintillators. These distributions are well approximated by Vavilov distribution below 5 GV and by Landau distribution above 5 GV. It is noted that the top and the bottom scintillators show different dE/dx behavior in the low rigidity region, where the energy loss in the detector becomes significant.

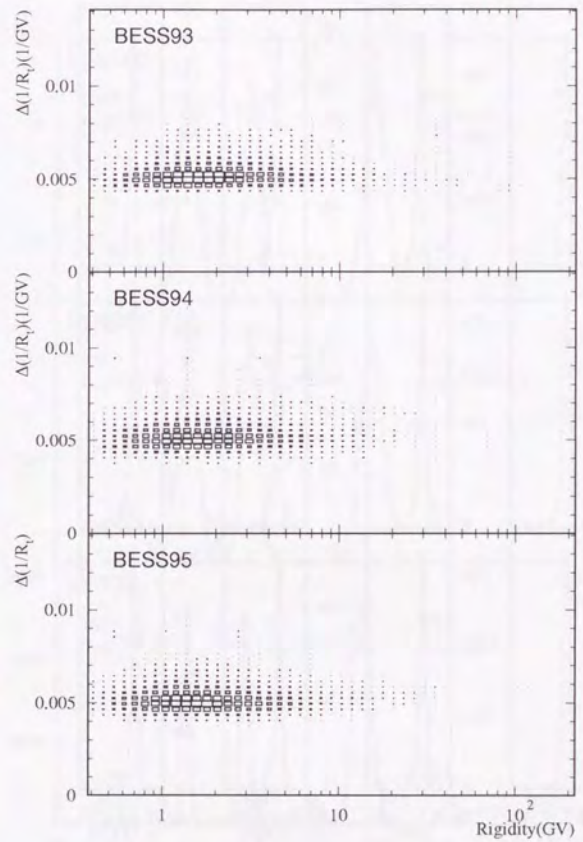

Figure 2.38: The error of $1/R_t$ vs $1/R_t$ in the $r\phi$ fitting.

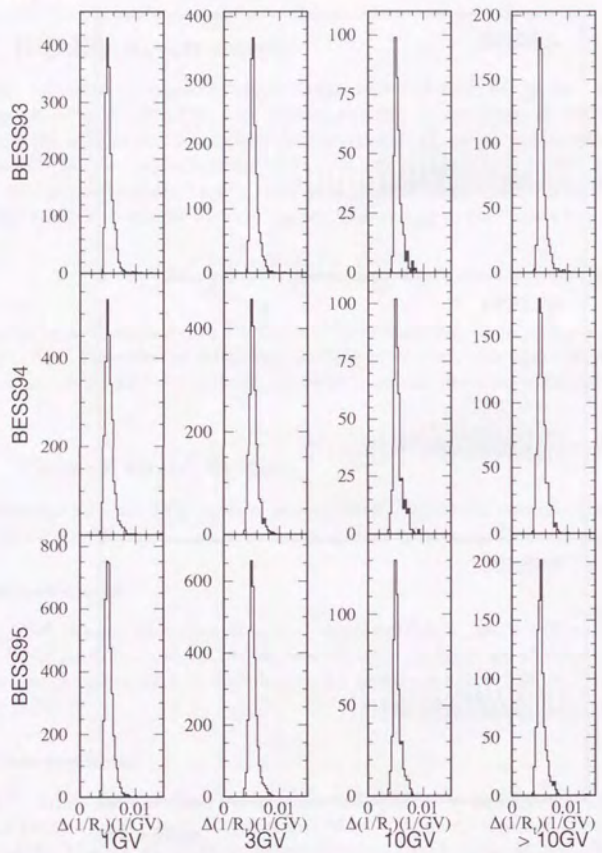

Figure 2.39: The error of $1/R_t$ in the $r\phi$ fitting around 1 GV, 3 GV, 10 GV and above 10 GV.

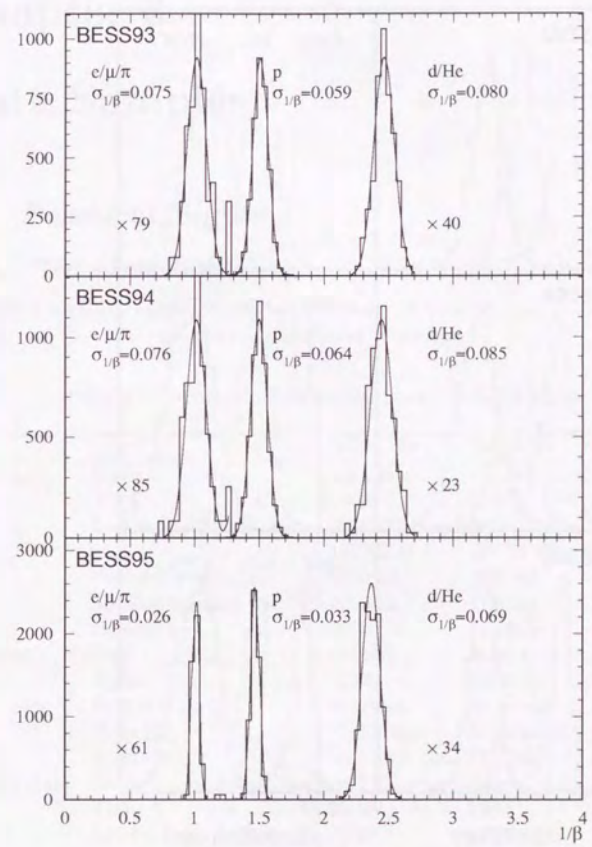

Figure 2.40: $1/\beta$ distribution around 0.9 GV.

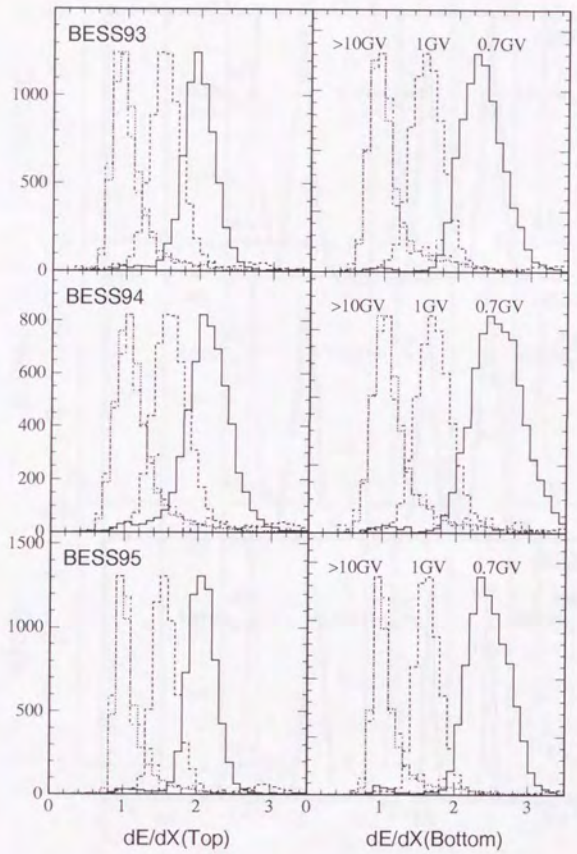

Figure 2.41: dE/dx distribution for protons. solid line:0.7 GV, dashed line:1 GV, doted line:10 GV and dotted-dashed line:100 GV.

Chapter 3

Data Samples

3.1 Scientific flights

3.1.1 Technical Ballooning

The BESS scientific balloon flights were carried out in northern Canada in summer '93 '94, and '95. Table 3.1 gives summaries of three flights.

Table 3.1: Technicalbalooning conditions in BESS flights.

		BESS-'93	BESS-'94	BESS-'95
Launching	Date	Jul. 26	Jul. 31	Jul. 25
	Time	19:20	21:30	21:04
	Location	56°48'N	56°48'N	56°48'N
		101°25'W	101°25'W	101°25'W
	Payload weight	2060 kg	2060 kg	2190 kg
	Total suspended weight	2700 kg	2700 kg	2700 kg
	Balloon size	29 MCF	29 MCF	29 MCF
Floating	Date	Jul. 26	Aug. 1	Jul. 26
	Time	22:30	2:30	0:30
	Period	17 hours	20 hours	20 hours
	Period	17.5 hours	17 hours	20 hours
	Altitude	35 – 36.5 km	35 – 36 km	35 – 36 km
Termination	Date	Jul. 27	Aug. 1	Jul. 26
	Time	15:47	19:45	20:00
	Impact time	16:30	20:20	20:45
	Location	57°52'N	55°89'N	55°32'N
		117°30'W	114°06'W	115°06'W

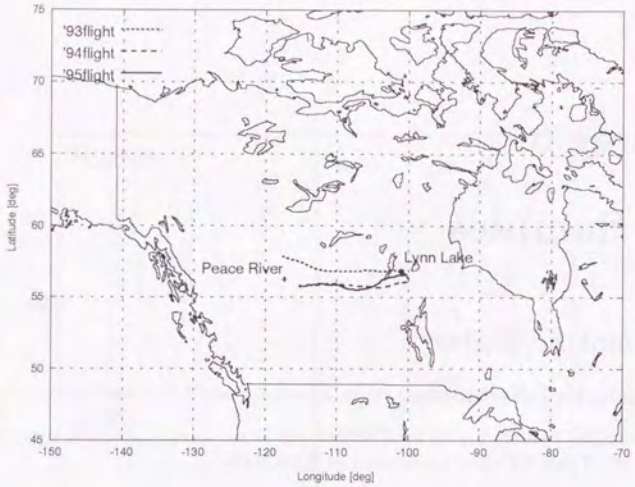

Figure 3.1: Flight trajectories for BESS '93, '94 and '95

The BESS spectrometer was launched from Lynn Lake Manitoba in the evening toward the end of July. It was suspended from a $8.3 \times 10^5 m^3$ ($2.9 \times 10^7 ft^3$) balloon filled with helium and achieved a float altitude of 36 km, corresponding to 5 g/cm^2 of residual atmosphere. The payload shifted to the west with the wind as shown in Figure 3.1.

The environment in the pressure vessel was kept in good state, as shown in Figure 3.2, 3.3 and 3.4. The temperature of JET drift chamber was within 9.5 °C and 35.8 °C and the pressure was 1120 g/cm^2 and 1200 g/cm^2 in case of '93. The scientific observation was carried out from midnight to next afternoon. The ballooning was terminated in the evening around Peace River, Albata, and the BESS payload came down by a parachute. It was safely recovered within a few days.

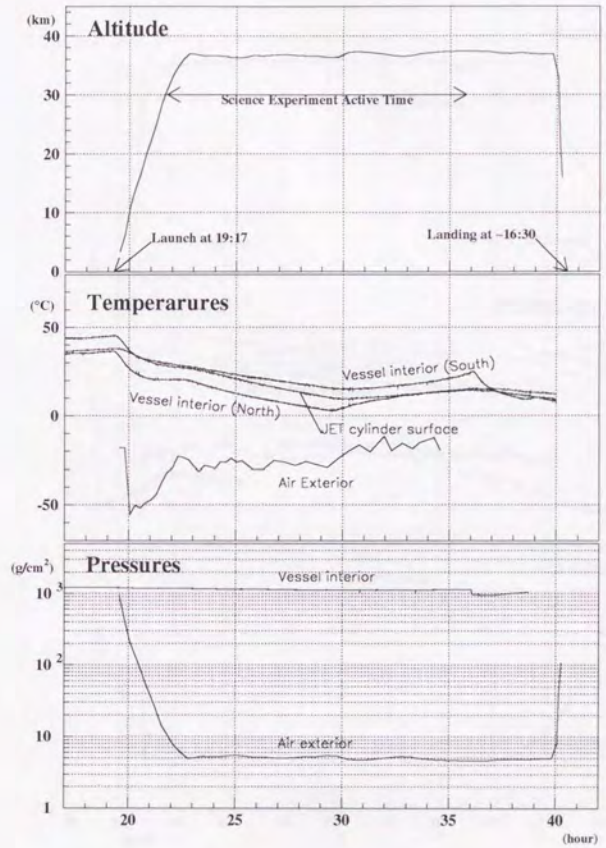

Figure 3.2: House-keeping data on altitude, temperatures and pressures in BESS '93 flight.

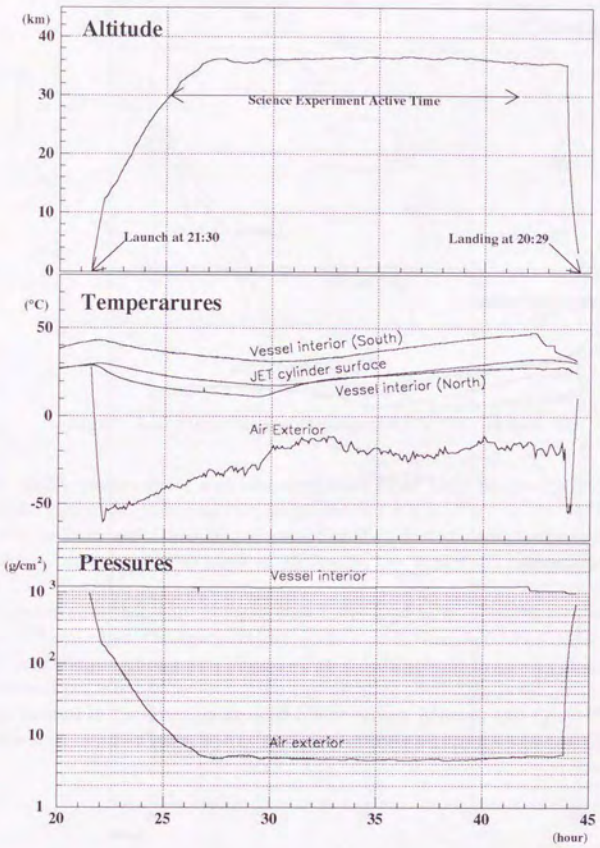

Figure 3.3: House-keeping data on altitude, temperatures and pressures in BESS '94 flight.

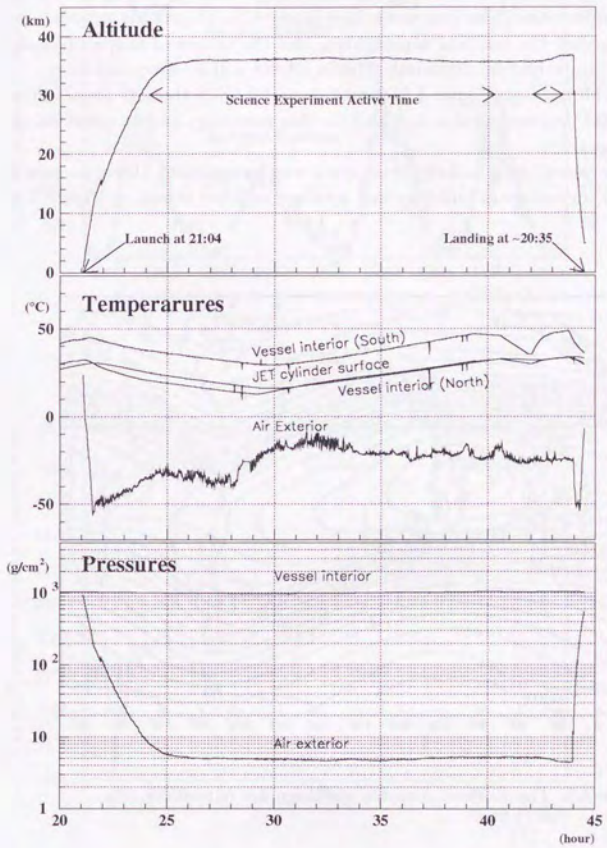

Figure 3.4: House-keeping data on altitude, temperatures and pressures in BESS '95 flight.

3.1.2 Residual Atmosphere, Rigidity Cutoff and Solar Activity

During all the data taking periods, the payload kept a float altitude of 36 km, which corresponds to 5 g/cm^2 of residual atmosphere above as shown in Figure 3.2, 3.3 and 3.4. Both interaction loss and secondary production of protons may happen while passing through the residual atmosphere, and the observed shape of cosmic ray proton spectrum might be distorted. Theses effects will be discussed later.

Magnetic cut-off rigidity (Figure 3.5) varied around 0.4 GV through three flights, but it stayed below instrumental cutoff and ,in this meaning, has no effect on observed proton spectrum.

In these three years, solar activity was on its way to approach the minimum as can be seen from the sunspots numbers and neutron monitor shown in Figure 3.6.

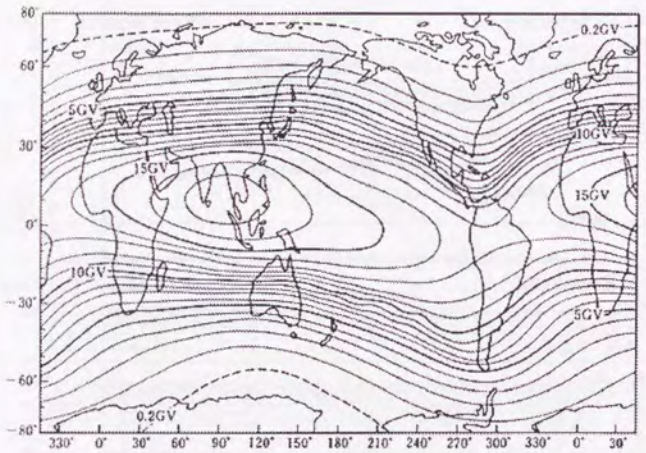

Figure 3.5: The contour map for geomagnetic cut-off rigidity.

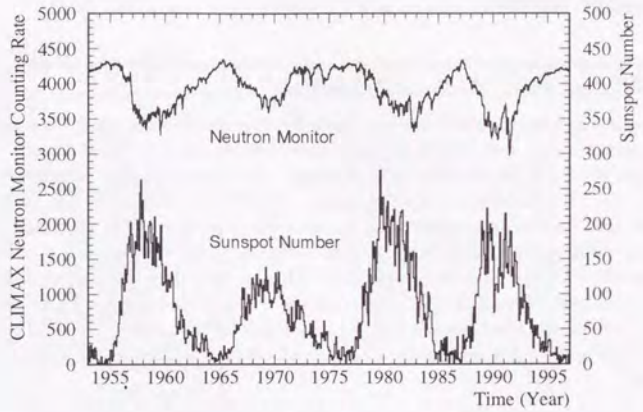

(a)

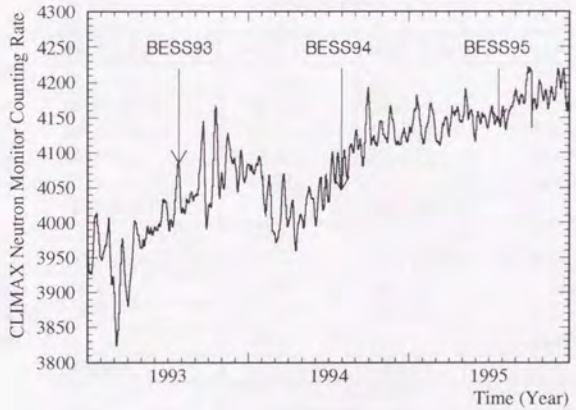

(b)

Figure 3.6: Solar activity; (a):Counting rate of CLIMAX neutron monitor and sunspot number (monthly average), (b):Counting rate of CLIMAX neutron monitor (7 day average).

3.1.3 Trigger Status

The BESS instrument was activated for 14, 15 and 18 hours in '93, '94 and '95 flight including runs for the trigger studies, and calibration runs.

Trigger parameters such as CD number and TT thresholds were optimized to achieve the desired trigger rate, based on the trigger rate obtained in the short pilot run just before the level flight. The actual trigger rate was adjusted to around 100 Hz while the T0 coincidence rate was about 2.3 kHz A calibration run of 5 to 10 minutes was carried out every hour to re-adjust the thresholds for FADC data zero-suppression as low as possible, not to suffer from the dependence of the pedestal value of FADC outputs on temperature. During each data acquisition run 10^8 charged cosmic ray rays made coincidence at the T0 level and 3.6×10^6, 4.8×10^6 and 4.6×10^6 events were recorded in '93, '94 and '95 flight, respectively. The amount of the data recorded during the experiments were 4.5 Gbytes, 6.5 Gbytes and 8.0 Gbytes.

Table 3.2 summarizes the T0 trigger, and Table 3.3 summarizes the T1 trigger.

Table 3.2: T0 trigger rate.

T0 Mode	Accepted Rate	Count Down	T0 Trigger Rate
BESS-'93			
T0 Low	2.3 kHz	1/1	1.7 kHz
T0 High	660 Hz	1/1	610 Hz
T0 gamma	19 kHz	1/256	75 Hz
T0 external	—	(OFF)	—
Total	22 kHz		2.4 kHz
BESS-'94			
T0 Low	2.2 kHz	1/1	2.2 kHz
T0 High	340 Hz	1/1	340 Hz
T0 gamma	18 kHz	1/256	70 Hz
T0 external	—	(OFF)	—
Total	21 kHz		2.6 kHz
BESS-'95			
T0 Low	2.0 kHz	1/1	2.0 kHz
T0 High	260 Hz	1/1	260 Hz
T0 gamma	18 kHz	1/256	70 Hz
T0 external	—	(OFF)	—
Total	20 kHz		2.3 kHz

Table 3.3: The settings of the T1 Trigger and the trigger rate.

	T1 Mode	Accepted Rate		Count Down		T1 Trigger Rate	
BESS-'93							
Biased	$\bar{p}$-clear		12 Hz		1/1		12 Hz
	$\bar{p}$-dirty		18 Hz		1/1		18 Hz
	$\bar{He}$-clear		3 Hz		1/1		3 Hz
	$\bar{He}$-dirty		6 Hz		1/1		6 Hz
	Missing		3 Hz		1/1		3 Hz
	Multi-clear		16 Hz		1/1		16 Hz
	Multi-dirty		8 Hz		1/1		8 Hz
	Gamma		1 Hz		1/1		1 Hz
Unbiased	T0 Low CD		1.7 kHz		1/140		12 Hz
	T0 High CD		500 Hz		1/40		12 Hz
	T0 gamma CD		50 Hz		1/100		0.5 Hz
	T0 external CD		—		(OFF)		—
Total			2.3 kHz				92Hz
BESS-'94 (First & Last half)							
Biased	$\bar{p}$-clear	30 Hz	21 Hz	1/1	1/1	30	21 Hz
	$\bar{p}$-dirty	14 Hz	10 Hz	1/1	1/1	14 Hz	10 Hz
	$\bar{He}$-clear	11 Hz	10 Hz	1/1	1/1	11 Hz	10 Hz
	$\bar{He}$-dirty	8 Hz	7 Hz	1/1	1/1	8 Hz	7 Hz
	Missing	9 Hz	10 Hz	1/1	1/1	9 Hz	10 Hz
	Multi-clear	32 Hz	24 Hz	1/1	1/1	32 Hz	24 Hz
	Multi-dirty	—	—	(OFF)	(OFF)	—	—
	Gamma	1 Hz	1 Hz	1/1	1/1	1 Hz	1 Hz
Unbiased	T0 Low CD	1.4 kHz	1.6 kHz	1/60	1/120	23 Hz	13 Hz
	T0 High CD	200 Hz	220 Hz	1/15	1/30	14 Hz	7 Hz
	T0 gamma CD	40 Hz	40 Hz	1/100	1/100	0.4 Hz	0.4 Hz
	T0 external CD	—	—	(OFF)	(OFF)	—	—
Total		1.7 kHz	1.9 kHz			142Hz	103 Hz
BESS-'95							
Biased	$\bar{p}$-clear		34 Hz		1/1		34 Hz
	$\bar{p}$-dirty		27 Hz		1/1		27 Hz
	$\bar{He}$-clear		11 Hz		1/1		11 Hz
	$\bar{He}$-dirty		10 Hz		1/1		10 Hz
	Missing		0.1 Hz		1/100		0.1 Hz
	Multi-clear		16 Hz		1/3		16 Hz
	Multi-dirty		—		(OFF)		—
	Gamma		1 Hz		1/10		0.1 Hz
Unbiased	T0 Low CD		1.2 kHz		1/90		13 Hz
	T0 High CD		260 Hz		1/20		8 Hz
	T0 gamma CD		43 Hz		1/256		0.2 Hz
	T0 external CD		—		(OFF)		—
Total			1.6 kHz				119Hz

3.2 Event Reconstruction

3.2.1 Data Extraction

The data acquisition was stopped every hour to take calibration data, and this procedure divides each flight data into several RUNs.

Table 3.4 summarizes the number of events in each run in each flight, where T0 is the number of the T0 triggers at the first level, T1 is the number of the T1 trigger, i.e. the number of the events the data acquisition system collected. The right half of the table shows the trigger modes of the recorded data, each of which corresponds to the T1 Trigger mode in Table 2.9.

The first step of the off-line data processing is to decompress the raw recorded data and extract track hits informations in each detector component together with trigger conditions. The event frames has different sizes varying from several hundred to three kilo bytes depending on the number of hits in detectors, and variable length data format is needed. The ZEBRA [18] system of CERN program library is employed to store the event data, since its dynamic data structuring capability is suitable for our purpose. The HEPDB [19] database management package of CERN program library, which is available in the ZEBRA system, is employed to store the geometries of the detector components, the read-out channel assignment tables and the calibration parameters.

The off-line calibrations were made on each run to derive temperature-dependent or pressure-dependent parameters, such as timing offsets in TOF measurement and drift velocity in the drift chambers. Primary calibrations were performed to obtain pedestals and gain factors. After initial calibrations, pattern recognition was performed using the hits of JET chamber to find tracks of the incident particles and track information banks are formed. The track impact point at IDC, ODC and TOF were calculated by extrapolating the fitted trajectory of the track, and linked to the track information bank. Thus, all informations of the hits and the track can be retrieved by accessing the track information bank.

Detailed calibrations were performed using the track informations retrieved as above. In order to speed up subsequent process, the informations of the track and associated hits were then stored into data summary files, which are flat files consisting of fixed length records. The results of the calibrations were put into the database, and the pattern recognition and track fitting were performed in the ZEBRA-based system again. The final data summary files for the physics analysis were then obtained from the re-created track information banks.

Table 3.4: The data amount in the BESS flights.

run #	time ($\times 10^3$s)	T0 ($\times 10^6$)	T1 ($\times 10^5$)	Record ($\times 10^5$)	T0 L ($\times 10^4$)	T0 H ($\times 10^4$)	MT p ($\times 10^4$)	MT He ($\times 10^4$)
93-13	3.29	5.82	2.89	2.84	4.09	4.19	10.14	2.87
14	2.80	4.95	2.45	2.41	3.49	3.57	8.74	2.49
15	3.80	6.70	3.31	3.25	4.71	4.81	11.75	3.29
16	2.90	5.11	2.51	2.48	3.60	3.66	8.88	2.46
17	3.54	6.25	2.98	2.94	4.40	4.46	10.45	2.83
18	4.21	7.38	3.50	3.44	5.22	5.24	12.12	3.21
19	4.06	6.93	3.44	3.39	4.89	4.90	11.21	2.77
20	4.58	7.73	3.90	3.83	5.47	5.48	13.65	3.65
21	3.46	5.89	3.09	3.04	4.15	4.14	10.83	3.02
22	2.16	3.67	1.93	1.90	2.59	2.55	6.73	1.93
23	3.53	5.41	2.88	3.15	4.24	4.18	11.15	3.22
24	4.06	6.89	3.74	3.68	4.85	4.74	13.54	3.95
93-total	42.39	72.73	36.63	36.35	51.71	51.92	129.19	35.68
94-6	3.81	5.51	5.37	5.26	9.29	5.32	20.54	6.13
7	3.21	4.66	4.55	4.45	7.85	4.56	17.14	5.27
8	3.04	4.42	4.31	4.22	7.46	4.30	16.15	4.95
9	3.32	4.72	4.62	4.52	7.95	4.62	17.18	5.41
10	3.74	5.41	5.24	5.11	9.12	5.30	19.03	6.09
13	2.16	3.16	3.01	2.93	5.31	3.08	10.54	3.57
15	3.11	4.98	3.24	3.18	4.12	2.36	15.90	5.86
16	5.44	8.76	5.54	5.45	7.24	4.06	26.92	10.21
17	3.14	5.00	3.14	3.08	4.12	2.28	15.11	5.86
18	2.34	3.80	2.36	2.32	3.13	1.69	11.39	4.40
19	3.50	5.67	3.52	3.45	4.70	2.51	16.91	6.58
20	3.27	5.33	3.30	3.24	4.41	2.33	15.90	6.14
94-total	40.08	61.43	48.18	47.21	74.70	42.41	202.71	70.47
95-7	3.26	4.41	3.59	3.57	4.87	2.62	21.15	7.12
8	3.41	4.52	3.68	3.66	4.99	2.73	21.67	7.39
9	2.56	3.12	2.55	2.53	3.43	1.92	14.91	5.15
10	2.56	3.10	2.50	2.47	3.41	1.92	14.47	5.01
11	3.91	4.82	3.89	3.87	5.33	3.02	22.56	7.91
12	4.41	4.15	3.35	3.33	4.57	2.59	19.41	6.90
13	3.11	3.82	3.07	3.05	4.20	2.36	17.75	6.31
14	0.48	0.61	0.49	0.49	0.68	0.37	2.85	.99
15	3.61	4.77	3.81	3.79	5.26	2.86	22.13	7.76
16	3.20	4.39	3.49	3.47	4.85	2.60	20.25	7.07
17	3.32	4.42	3.53	3.51	4.88	2.57	20.48	7.14
18	3.34	3.94	3.13	3.08	4.35	2.24	17.96	6.22
19	5.31	3.89	3.07	3.00	4.29	2.15	17.50	6.00
20	2.88	4.08	3.21	3.17	4.49	2.21	18.57	6.31
22	2.35	3.31	2.60	2.56	3.63	1.78	15.07	5.13
95-total	47.70	57.34	45.97	45.56	63.24	33.96	266.74	92.41

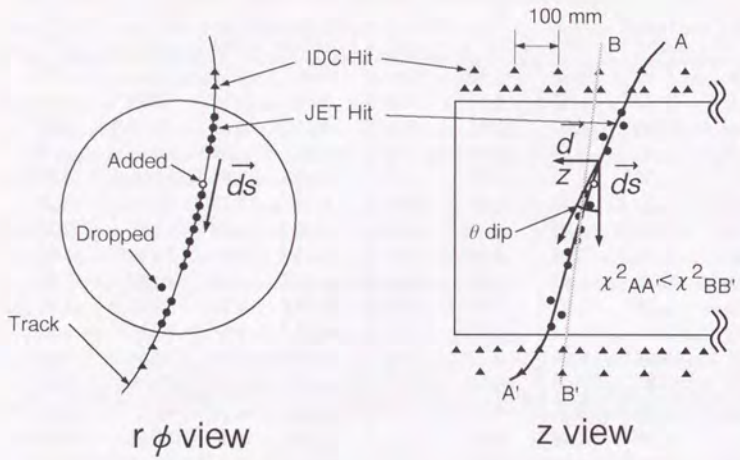

Figure 3.7: Method of the rigidity measurement.

3.2.2 Track Reconstruction

The hit position in the $r\phi$-plane is calculated by its drift time and the drift velocity. Although the drift length x and the drift time t are nearly proportional, some nonlinear effects exist due to the distortion of the electric field. Such nonlinearity was corrected by a three-order polynomial function fitted to the deviation of the hit positions.

The rigidity of a particle was determined by the JET and IDC drift chambers. First the transverse rigidity (R_t), the rigidity component perpendicular to the magnetic field direction, was determined by circular fitting in the $r\phi$-plane (Figure 3.7).

In order to select the hits used in the trajectory fitting, the following algorithm was employed.

1. Select 'good' hits, which are defined as hits with enough charge and width.

2. Find trajectories by connecting the 'good' hits in JET chamber and perform circular fitting.

3. Extrapolate each of the trajectories to IDCs to find 'good' IDC hits near the trajectory, and associate to the track.

4. Perform trajectory fitting again using all hit points in the JET and IDCs which are associated to the track. "Karimaki method"[20] are applied for the fitting algorithm at this stage.

5. Scan all of 'good' hits in JET chamber and check if they are close enough to the track, i.e. within the distance 5 times of the position resolution, 5σ. Only the hits passing this check are used in the following processes.

6. Repeat step-4 and -5 twice.

The resultant R_t should be then corrected to cancel out the effect of non-uniformity of the magnetic field. Monte Carlo calculations with the computed magnetic field provides the correction factor to the rigidity of various trajectories as functions of the track position, the inclination and the rigidity. According to the simulation, this correction should reproduce the original rigidities within a typical accuracy of $\pm$ 0.2% for the tracks within the limited fiducial volume finally to be utilized for the flux measurement.

To convert R_t into the total rigidity (R), the dip angle θ_{dip} is obtained by fitting in the yz-plane as shown in Figure 3.7, where θ_{dip} is defined as an angle between the $r\phi$-component ($\vec{ds}$) and the z-component ($\vec{dz}$) of R. A similar iterative procedure as used in the $r\phi$ fitting is utilized to eliminate irrelevant hits. The selected hits are fitted to a sine-curve. Since the IDCs provide the only z positions modulo 100mm, all possible combinations of the IDC hits are examined. The resultant θ_{dip} are obtained from the combination having minimum χ^2 value in this fitting procedure.

Finally rigidity R are derived from R_t and θ_{dip} as,

$$R = \frac{R_t}{\cos\theta_{dip}}.$$

3.2.3 Time of Flight Measurement

Figure 3.8 illustrates the measurement scheme of time-of-flight (TOF). The TOF between top and bottom TOF hodoscopes is calculated for each track by the following procedure. We use here the suffix 'elec' for the PMT on the side of the electronics and the suffix 'tank' for the PMT on the side of the helium reservoir tank.

1. Correct a timing walk using the charge information for each PMT. We use the following formulae:

$$\hat{t}_{elec} = t_{elec} - a_i/\sqrt{q_{elec}},$$

and

$$\hat{t}_{tank} = t_{tank} - a_i/\sqrt{q_{tank}},$$

where $t_{elec,tank}$ is the measured timing, $\hat{t}_{elec,tank}$ the timing after the correction, q the measured charge of the PMT, and a_i is the parameter of the ith PMT. Parameter a was determined by the beam test.

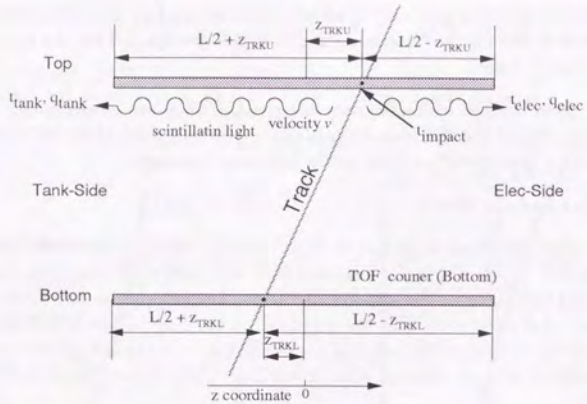

Figure 3.8: Method of the TOF measurement.

2. Derive the timing that the particle passed through the counter (t_{impact}) from the corrected timing of each PMT. Using the z-impact point (z_{trku}, z_{trkl}) of the particle which is calculated by extrapolating the combined track, t_{impact} is obtained for elec-side as,

$$t_{elec}^{impact} = \hat{t}_{elec} - \frac{\frac{L}{2} - z_{trku,trkl}}{v_{eff}} - t_{offset}(z_{trku,trkl}),$$

and for tank-side as,

$$t_{tank}^{impact} = \hat{t}_{tank} - \frac{\frac{L}{2} + z_{trku,trkl}}{v_{eff}} - t_{offset}(z_{trku,trkl}),$$

where v_{eff} is the effective light velocity in the counter and L is the length of the counter including the light guides. The second term is the propagation time for the scintillation light to reach each PMT. The last term $t_{offset}(z)$ is the timing offset as a function of the z position. This is introduced to correct the velocity variation depending on the z position and is determined by calibration for each counter. The averaged impact time of the counter is then obtained as;

$$t_{impact} = \left(\frac{t_{impact\_elec}}{\sigma_{elec}(z)^2} + \frac{t_{impact\_tank}}{\sigma_{tank}(z)^2}\right) \Big/ \left(\frac{1}{\sigma_{elec}(z)^2} + \frac{1}{\sigma_{tank}(z)^2}\right),$$

where $\sigma(z)$ is the timing resolution of each PMT as a function of z.

3. The value t_{impact} is individually calculated for both top and bottom counters, and then the TOF is obtained as the time difference between them.

The $\beta \equiv v/c$ of the particle can be determined from the TOF and the path length derived from the trajectory.

3.2.4 dE/dx Measurement

The energy deposit of a particle, dE/dx, in a scintillator is derived from the pulse size of the PMT output, which is measured by ADC as a charge.

1. Subtract the pedestal value from the ADC count and correct it for the gain of PMT and ADC.

$$q = (\text{count} - \text{pedestal})/\text{gain}$$

The gain is determined by the calibration to normalize the energy deposit dE/dx of energetic protons to be 1.

2. Correct the z dependence of the signal amplitude due to the attenuation or loss of scintillation light using the z-impact position of the track. The detailed study shows that the measured charge $q_{measured}$ has the z-dependence as follows:

$$q_{measured} \simeq (a + be^{cz})dE \ ,$$

where a,b and c are parameters that should be determined by the calibration, and dE is the deposited energy.

3. Average the energy deposit dE derived from the PMT signals of two ends.

4. Divide the average energy deposit by the path length in the scintillator through which the particle passed. This gives dE/dx in the TOF counters.

3.3 Simulation

Monte Carlo (M.C.) simulations were performed in the analysis for the following purposes:

- We use the M.C. to simulate the behavior of protons both in the atmosphere and in the instrument.
- Although the solenoid coil produced an almost uniform magnetic field, we should take account of the slight non-uniformity in order to make a precise rigidity measurement. Simulating the magnetic field and tracing the path of the incident particles by small steps, we can find the relation between the true rigidity and the measured rigidity determined by the curvature of the circular fit.

We have built a simulation model of the BESS instrument based on the GEANT/GHEISHA [21] code, by assembling every detector components, support frames and other materials which are defined with the actual dimensions and material components. The model reproduces the material distribution in detail.

Figure 3.9 shows the view of the simulated BESS instrument.

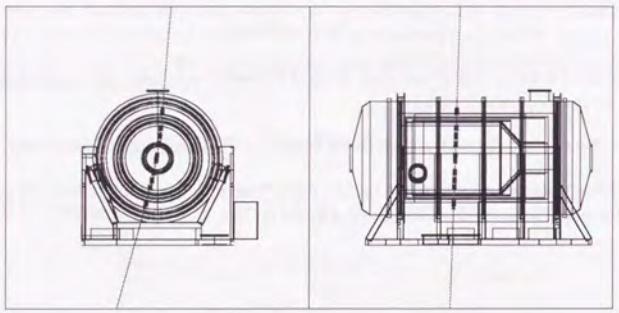

Figure 3.9: Simulated BESS detector

Chapter 4

Data Analysis

4.1 Global Efficiency Check by Event Scan

A distinctive advantage of BESS detector is the large number of readout points (1+1 in TOF, 2+2 in ODCs, 2+2 in IDCs, 24 in JET per one track at maximum), which gives high capability in finding and reconstructing tracks. No cosmic rays that passed through BESS detector will be "missed". In order to confirm this advantage, we scanned five hundreds events randomly for each flight. One, five and ten events were found in '93, '94 and '95 data, respectively, in which reconstruction of the track failed. Among them, dominant portion (zero, three and seven events among five hundreds events for '93, '94 and '95,respectively) was due to the too large event data size. As is described in Section 2.8, events that have too many hits in the chambers are discarded to ensure high speed data taking. As a result of event scan, it is concluded that 98.9% of the cosmic rays which passed through BESS detector can been "seen". Hence, the analysis is restricted to single track events.

4.2 Event Selections

4.2.1 Pre-selection

Pre-selection defines the population or "starting sample" which undergoes succeeding analysis.

Good single track selection

In order to eliminate "empty" events and the events with multi-tracks, the following cuts were applied to select good single track events.

I. $N_{\mathrm{TOF(Top)}} = 1$, $N_{\mathrm{TOF(Bottom)}} = 1$.
There should be one and only one hit in the scintillation counters both at the top and at the bottom.

II. $N_{\mathrm{Track}} = 1$.
The number of tracks with 10 or more hits found in JET chamber should be

one and only one.

Downward movement

Since we are going to derive the flux of protons at the top of the atmosphere, the further analysis are limited to the events with downward moving particles.

I. $\beta > 0$.

Fiducial Volume Cut

Though BESS has large geometrical acceptance, there is some non-uniformity in its performance. For example, if the cosmic ray particle passed near the edge of the JET chamber, only a few hits might be recorded and the accuracy of the determination of its rigidity is decreased. In order to avoid these kinds of inaccuracy, fiducial volume was defined by applying the following two conditions. These conditions are common to all three flights.

I. $|z_{\mathrm{Track@TOF(Top)}}| < 430$ mm, $|z_{\mathrm{Track@TOF(Bottom)}}| < 430$ mm.
This condition requests that the incident particle should pass through well inside the fiducial z-region of TOF scintillators. The measurements show odd behavior in small regions at the ends of the TOF counters. This is because some of the incident particles do not pass through the scintillator but through the light guide while the position calculated from the extrapolation of the fitted trajectories are within the scintillator.

II. $N_{\mathrm{Expect}} \geq 24$.
The number of hits in JET chamber expected from the trajectory (N_{Expect}) is 24. This cut defines the fiducial region of the JET chamber to the central four column shown in Figure 2.7, and eliminates the track which scratches the outermost region, where the position measurement is less accurate than the central region due to the distortion of the electric field.

This fiducial volume cut reduces geometrical acceptance to around 0.1 $\mathrm{m^2sr}$.

4.2.2 Proton-like event selection

After the selections described above, the distributions of $\mathrm{d}E/\mathrm{d}x$ and $1/\beta$ vs rigidity are shown in Figures 4.1 and 4.2, respectively. These figures indicate that protons can be identified already. We selected "the starting sample" of the proton events at this stage using $\mathrm{d}E/\mathrm{d}x$ in scintillation counters under the condition of positive rigidity, and call them "proton-like" events. This "proton-like" events selection is shown in Figure 4.3. Because of the high performance of BESS, "proton like" events include almost all the proton events with negligible amount of backgrounds.

This "proton-like" events thus selected may be used to determine the proton spectrum at least at low rigidity, because the rigidity measurements of these loosely

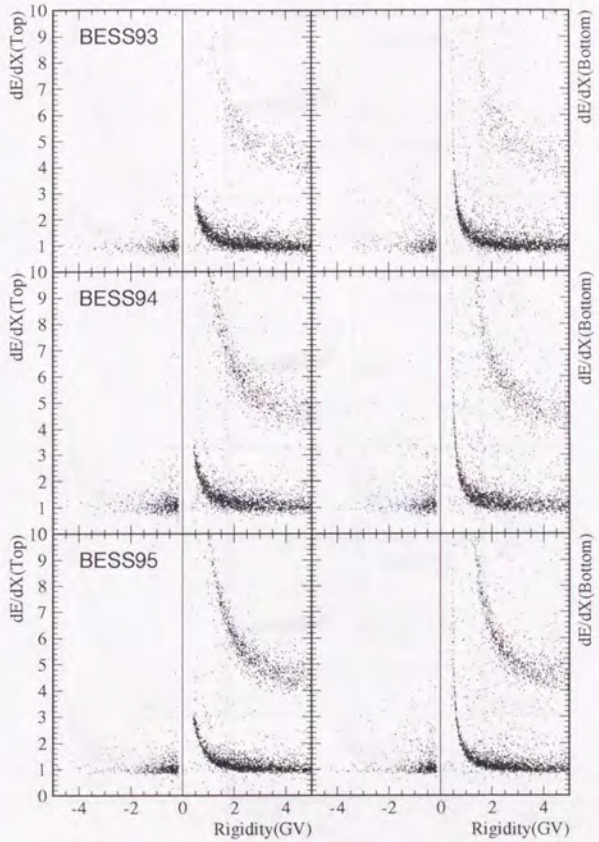

Figure 4.1: $\mathrm{d}E/\mathrm{d}x$ vs rigidity distribution

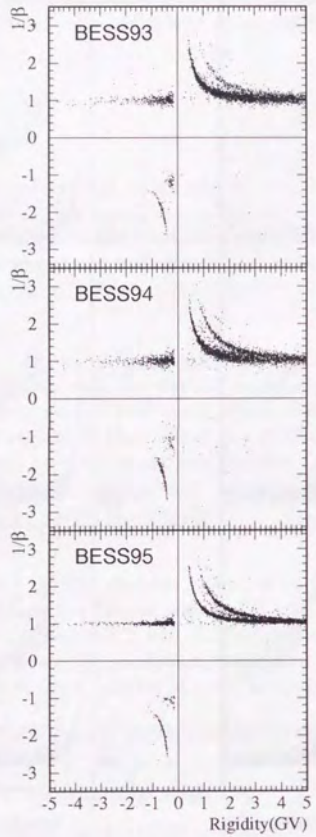

Figure 4.2: $1/\beta$ vs rigidity distribution

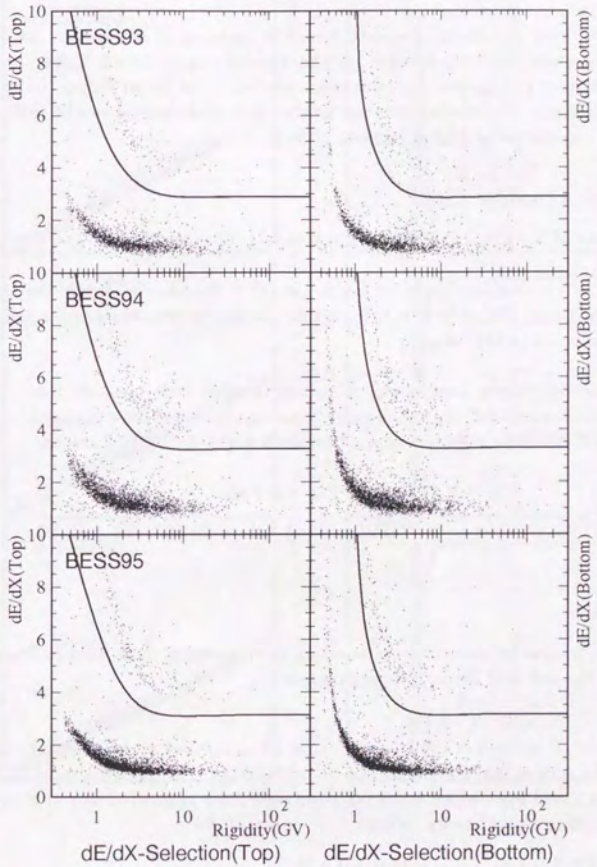

Figure 4.3: "Proton-like" events selection.

selected events are already accurate enough at low rigidity region. This can be seen in Figure 4.4, where relative fitting error of transverse rigidity ($\Delta R_t/R_t$) is shown as function of R_t at left and the integral error distribution at R_t =2 GV is shown at right. As seen from the figure, the rigidity at 2 GV is measured within 2% accuracy for 99% of events.

However, the error in the rigidity determination goes up in proportion to the rigidity. We therefore need to demand ,in the rigidity region much higher than 10 GV, much stricter cut specially in the track quality in order to ensure reliable rigidity determination. Otherwise, the tail in the ΔR_t distribution might deform the steep energy spectrum at higher rigidity region.

4.2.3 Event Quality Cut

The main purpose of "quality cut" is to improve the rigidity resolution in the highest rigidity region.

The rigidity of the incident particle inside the JET chamber is determined by fitting the hit positions. Only the events for which the fitting procedure was applied accurately are selected in this stage.

> The cut conditions have some difference in each year because the read-out scheme and the state of chambers during the flights have changed. Hear-after if different cuts are applied for each flight data, they are expressed as
>
> $$X \geq [CUT93, CUT94, CUT95],$$
>
> where $CUT93$, $CUT94$ and $CUT95$ are cut values for '93, '94 and '95 data.

Goodness of fits

The goodness of fits can be checked by examining the number of data used in fitting procedures and the reduced chi-square parameters:

I. $N_{r\phi\text{-fit}} \geq 17$, $N_{z\text{-fit}} \geq [9, 13, 13]$.
The number of hit points used in $r\phi$-fitting ($N_{r\phi\text{-fit}}$) and in z-fitting ($N_{z\text{-fit}}$) are directly related to the reliability of its results. The above condition is good enough and even when more hit points used are requested in the fitting procedure, the results hardly change.

II. $\chi^2_{r\phi\text{-fit}} < [4.5, 5.0, 4.5]$, $\chi^2_{z\text{-fit}} < [5.0, 5.0, 5.5]$,
where

$$\chi^2_{r\phi\text{-fit}} \equiv \frac{1}{\sqrt{N_{r\phi\text{-fit}} - 3}} \sqrt{\sum \frac{(\Delta(r\phi)_i)^2}{\sigma^2_{r\phi,i}}},$$

$$\chi^2_{z\text{-fit}} \equiv \frac{1}{\sqrt{N_{z\text{-fit}} - 2}} \sqrt{\sum \frac{(\Delta(z_i))^2}{\sigma^2_{z,i}}}.$$

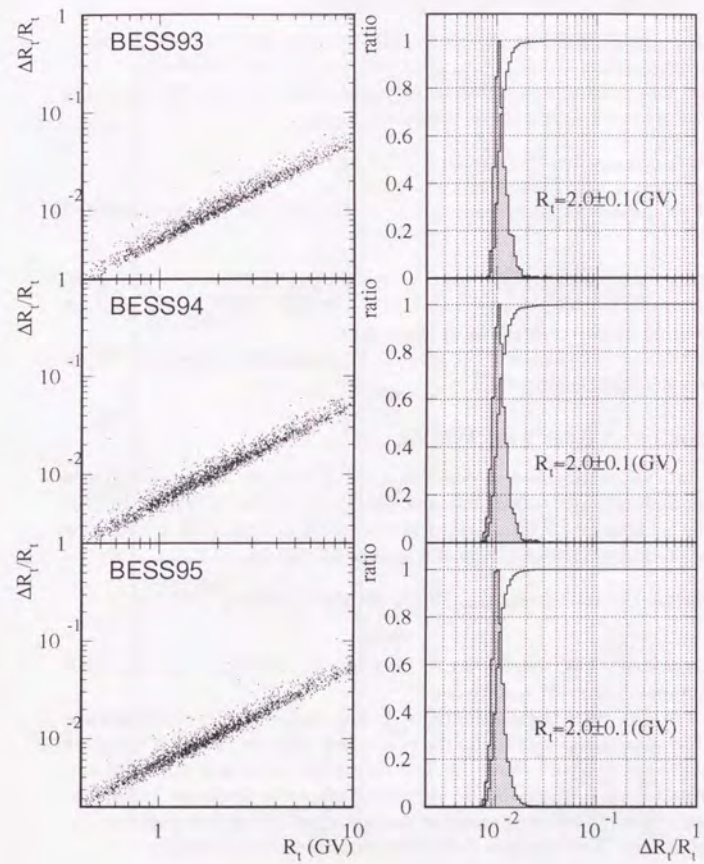

Figure 4.4: Relative error of transverse rigidity after primitive cuts. Hatched:differential, Open:integral

Requirement of good IDC hits

In order to select "good" events, whose track trajectory or velocity is believed to be reconstructed correctly, the following cuts were applied.

I. $\min\{\Delta(r\phi)_{\mathrm{IDC1(Inner)}}, \Delta(r\phi)_{\mathrm{IDC1(Outer)}}\} < [0.7, 1.0, 0.8]$ mm,
$\min\{\Delta(r\phi)_{\mathrm{IDC2(Inner)}}, \Delta(r\phi)_{\mathrm{IDC2(Outer)}}\} < [0.9, 1.3, 1.2]$ mm.
The IDC hits provide useful information independent of the JET hits, and these hits are strict constraint on trajectory fitting.

II. $\min\{\Delta(z)_{\mathrm{IDC1(Inner)}}/3, \Delta(z)_{\mathrm{IDC1(Outer)}}\} < 2.0$ mm,
$\min\{\Delta(z)_{\mathrm{IDC2(Inner)}}/3, \Delta(z)_{\mathrm{IDC2(Outer)}}\} < 2.0$ mm.
Desired precision of the informations in z–fit are obtained only by using IDC hits.

When the fitting is done wrong, the fitted track is far from IDC hits. The above two cuts require a consistency between the hits in JET and IDCs. At least one good hit in each IDC should be close enough to the trajectory.

The above cuts, i.e. "goodness of fits cuts" and "requirement of good IDC hits", are categorized to "track quality cut".

Consistency of fitted track with TOF hit

Impact point in TOF scintillation counter along the z-direction can be determined by two independent methods; extrapolation of the fitted track in JET/IDCs and the time difference between two PMTs located at both ends of each TOF scintillation counter. The consistency between them will be a good anchor.

I. $\{\Delta(z)_{\mathrm{TOF(Top)}})^2 + (\Delta(z)_{\mathrm{TOF(Bottom)}}\}^2 < [(100\mathrm{mm})^2, (100\mathrm{mm})^2, (40\mathrm{mm})^2]$.

This cut is named "TOF quality cut". The track quality cuts and the TOF quality cuts compose the event quality cut.

Figures 4.5 to 4.11 show the distributions of these values together with the cut boundaries. The open histograms are for the events that pass the pre-selection (good single track selection, fiducial volume cut and downward movement selection) and proton-like event selection (loose $\mathrm{d}E/\mathrm{d}x$ selection), while the shadowed histograms are for the events that remain after applying the event quality cut (track quality cut and TOF quality cut). The selection criteria are summarized in Table 4.1.

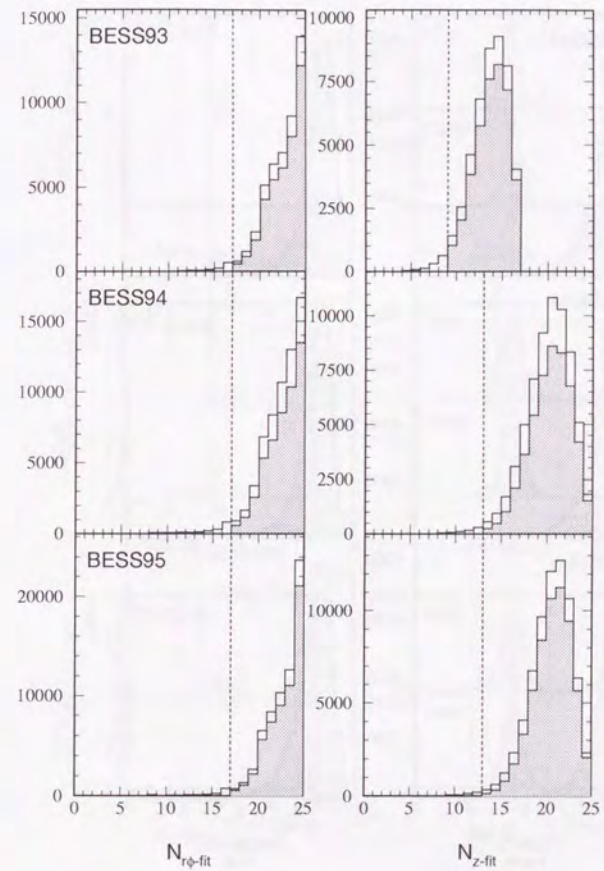

Figure 4.5: $N_{r\phi\text{-fit}}$ cut and $N_{z\text{-fit}}$ cut.

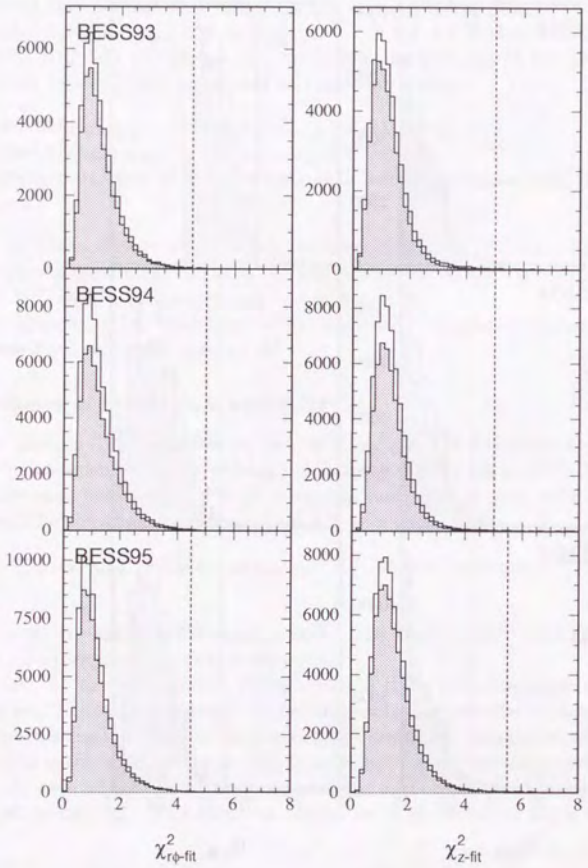

Figure 4.6: $\chi^2_{r\phi-\mathrm{fit}}$ cut and $\chi^2_{z-\mathrm{fit}}$ cut

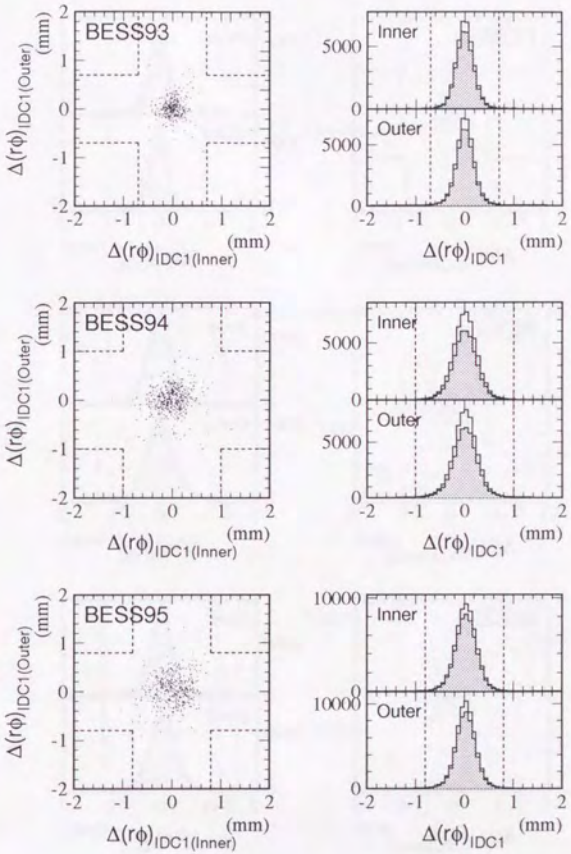

Figure 4.7: $\Delta(r\phi)_{\mathrm{IDC1}}$ cut

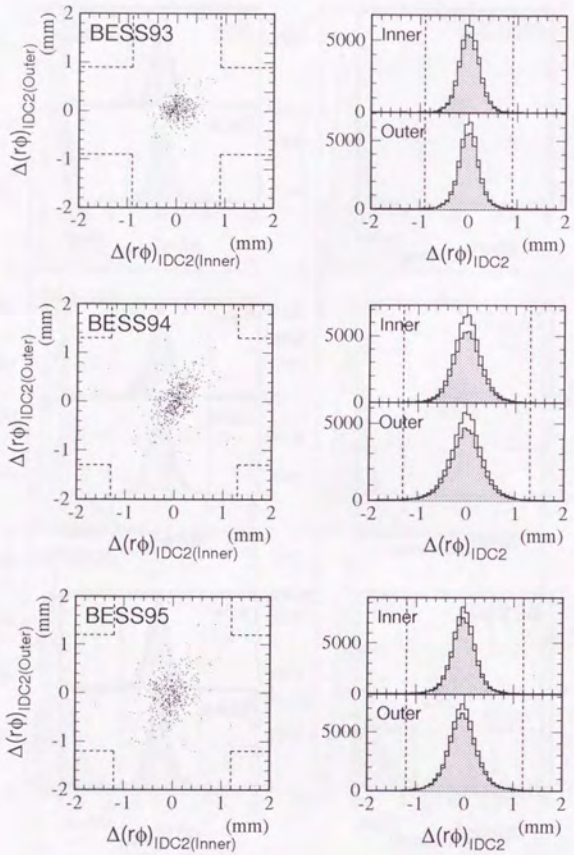

Figure 4.8: $\Delta(r\phi)_{\mathrm{IDC2}}$ cut

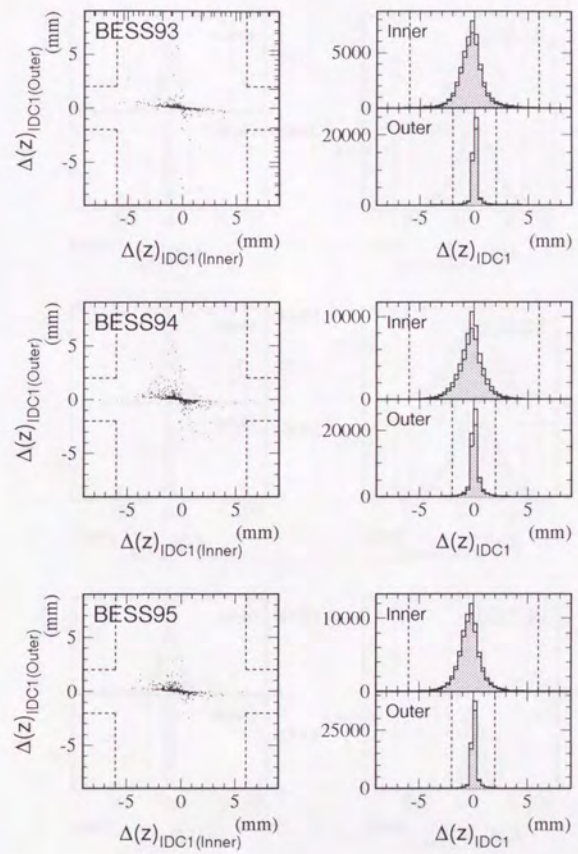

Figure 4.9: Δz_{IDC1} cut

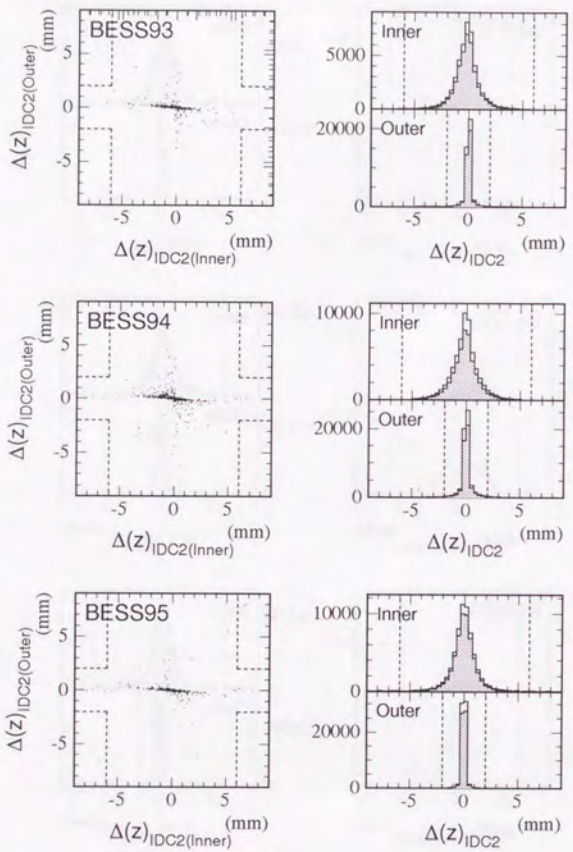

Figure 4.10: Δz_{IDC2} cut

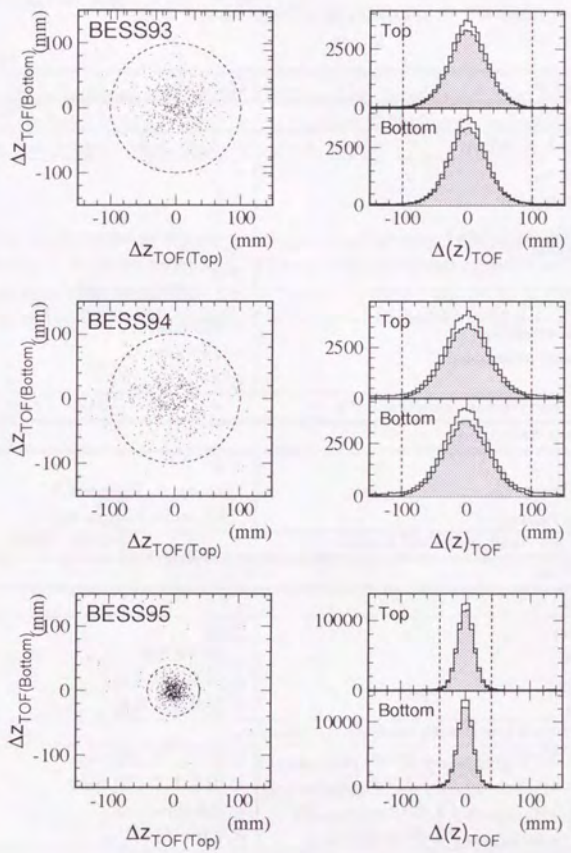

Figure 4.11: Δz_{TOF} cut

Table 4.1: A summary of the selection criteria.

Cut No.	Variable	Quantity
Pre-selection		
Good single track selection		
I.	$N_{\mathrm{TOF(Top)}}$	$= 1$
	$N_{\mathrm{TOF(Bottom)}}$	$= 1$
II.	N_{Track}	$= 1$
Downward movement		
I.	β	> 0
Fiducial volume cut		
I.	$\lvert z_{\mathrm{Track@TOF(Top)}}\rvert$	< 430 mm
	$\lvert z_{\mathrm{Track@TOF(Bottom)}}\rvert$	< 430 mm
II.	N_{Expect}	≥ 24
The number of survived unbiased events		[53429, 78267, 78818]
Proton-like Event Selection		
I.	R	> 0
II.	$\mathrm{d}E/\mathrm{d}x_{\mathrm{Top}}$	"Shown in Figure 4.3"
	$\mathrm{d}E/\mathrm{d}x_{\mathrm{Bottom}}$	"Shown in Figure 4.3"
The number of survived unbiased events		[44686, 63335, 66426]
Event Quality Cut		
Goodness of fits		
I.	$N_{r\phi-\mathrm{fit}}$	≥ 17
	$N_{z-\mathrm{fit}}$	$\geq [9, 13, 13]$
II.	$\chi^2_{r\phi-\mathrm{fit}}$	$< [4.5, 5.0, 4.5]$
	$\chi^2_{z-\mathrm{fit}}$	$< [5.0, 5.0, 5.5]$
Consistency of fitted track with each hit in chamber		
I.	$\min\{\Delta(r\phi)_{\mathrm{IDC1(Inner)}}, \Delta(r\phi)_{\mathrm{IDC1(Outer)}}\}$	$< [0.7, 1.0, 0.8]$ mm
	$\min\{\Delta(r\phi)_{\mathrm{IDC2(Inner)}}, \Delta(r\phi)_{\mathrm{IDC2(Outer)}}\}$	$< [0.9, 1.3, 1.2]$ mm
II.	$\min\{\Delta z_{\mathrm{IDC1(Inner)}}/3, \Delta z_{\mathrm{IDC1(Outer)}}\}$	< 2.0 mm
	$\min\{\Delta z_{\mathrm{IDC2(Inner)}}/3, \Delta z_{\mathrm{IDC2(Outer)}}\}$	< 2.0 mm
Consistency of fitted track with each hit in TOF		
III.	$(\Delta z_{\mathrm{TOF(Top)}})^2 + (\Delta z_{\mathrm{TOF(Bottom)}})^2$	$< [(100\mathrm{mm})^2, (100\mathrm{mm})^2, (40\mathrm{mm})^2]$
The number of survived events (unbiased)		[37689,49629,57182]

4.3 Selection of Proton Events

In Section 4.2 are already described the selection criteria of "proton-like" events. In order to eliminate small contaminations of positrons and deutrons, we applied tighter cuts at this stage in $\mathrm{d}E/\mathrm{d}x$ and $1/\beta$.

$\mathrm{d}E/\mathrm{d}x$ cut

Two lines in each figure in Figure 4.12 show the "proton $\mathrm{d}E/\mathrm{d}x$-band"cut. The proton $\mathrm{d}E/\mathrm{d}x$-band is determined to contain the 95% of protons assuming Vavilov or Landau distribution depending on rigidity region.

β cut

Two lines in each figure in Figure 4.13 show the "proton $1/\beta$-band" cut. To keep high efficiency in β cut, a half width of the proton $1/\beta$-band is set to be 3.89σ. The efficiency is very close to 100%.

After these tighter $\mathrm{d}E/\mathrm{d}x$ cut and $1/\beta$ cut, protons are selected with an efficiency of 95%.

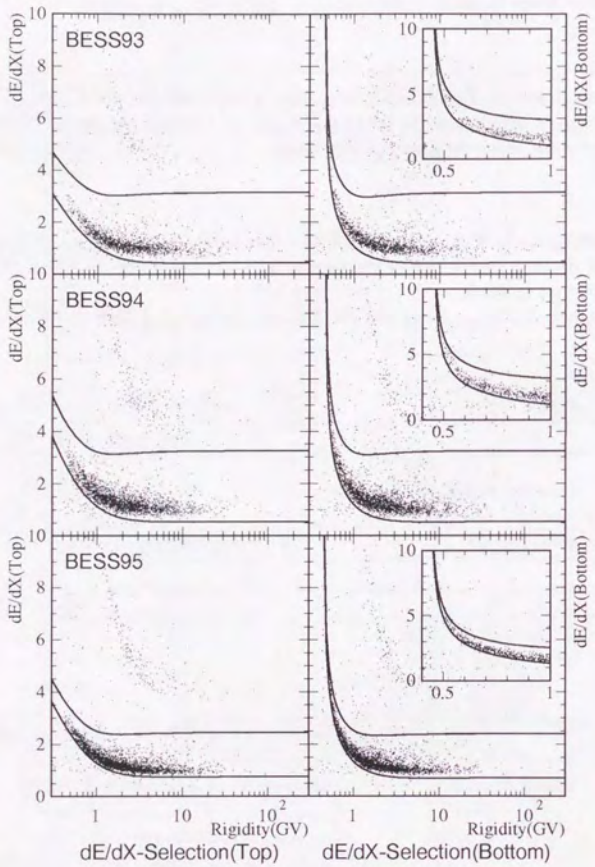

Figure 4.12: Proton dE/dx cut

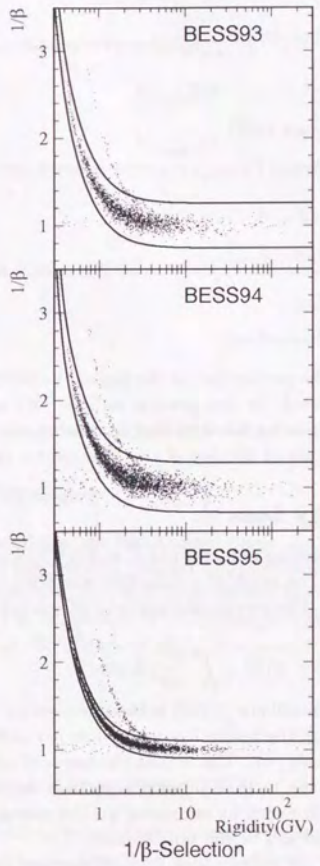

Figure 4.13: Proton $1/\beta$ cut

4.4 Corrections

The energy spectrum and the flux measured in the BESS tracking detector (JET and IDCs) has some difference from those at the top of the atmosphere (TOA) because of the following processes:

1. Ionization Energy Loss
2. Trigger Efficiency ($\varepsilon_{Trigger}$)
3. Energy dependent acceptance ($S\Omega$)
4. Single Track Selection Efficiency (ε_{single})
5. Quality Cut Efficiencies (ε_{Q-cut})
6. Proton Selection Efficiencies ($\varepsilon_{P-select}$)
7. Losses in the Atmosphere
8. Atmospheric Secondary Production

After the corrections for 1 – 6, the proton flux at the top of the BESS instrument (at 5g/cm^2 below TOA) is determined. In this process online– and off-line efficiency, are to be considered. Then, correcting for the effect of residual air above the BESS instrument (7 – 8), the proton flux at the top of the atmosphere can be obtained.

4.4.1 Ionization Energy Loss

The protons observed by the tracking detector (JET and IDCs) had lost their energies while traversing 5 g/cm^2 of the residual atmosphere and 9.0 g/cm^2 of the upper half material of the instrument. The energy of a particle after traveling into a depth x is given as:

$$E(x) = E(0) - \int_0^x \frac{dE}{dx}(E)dx.$$

The energy at the top of the atmosphere ($E(0)$) is then derived by using the energy measured at JET chamber ($E(x)$), the ionization energy loss per unit depth (dE/dx), and the thickness of the materials (x). The actual thickness of the material for a particle to traverse depends on the inclination of the particle trajectory. The total energy loss is calculated for each event by summing up the energy losses at every steps in the detector components and in the atmosphere.

In this calculation process, no energy loss fluctuations are considered. This simplification holds to a fairly good approximation down to 0.1 GeV as will be seen in Figure 4.20. The vertical spread of the dense line labeled "NOT INTERACTED" corresponds to the energy loss fluctuations, which is so small that neglecting the Landau tail will not deform the spectrum shape.

Hereafter, we will use the term "energy" to refer to the energy at the top of the atmosphere (TOA).

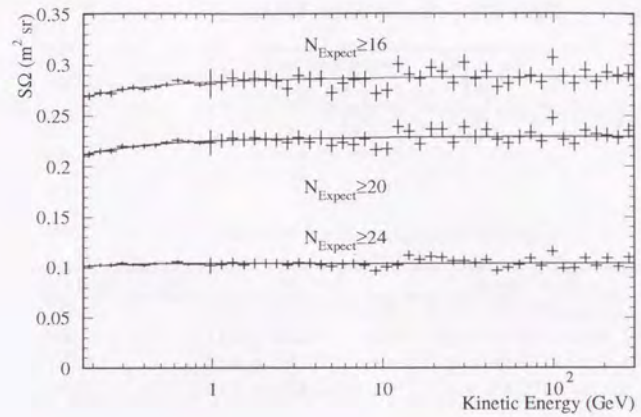

Figure 4.14: The energy and $N_{\rm Expect}$ dependence of acceptance (BESS95).

4.4.2 Trigger Efficiency ($\varepsilon_{Trigger}$)

In BESS DAQ scheme, there are two trigger mode, i.e. unbiased (T0 CD) and biased trigger (TT). As described in Section 2.7, the analysis in this thesis uses only CD trigger events. Since the rate of trigger failure is considered to be negligible thanks to the enough low thresholds of TOF trigger signals, the trigger efficiency can be defined simply as the inverse of count down cycle N_{CD}

$$\varepsilon_{Trigger} = \frac{1}{N_{CD}}.$$

4.4.3 Geometrical Acceptance ($S\Omega$)

In the stage of pre-selection, "fiducial volume cut" was applied using $z_{\rm Track@TOF(Top)}$, $z_{\rm Track@TOF(Bottom)}$ and $N_{\rm Expect}$. Once the fiducial volume is defined, geometrical acceptance is delimited.

The geometrical acceptance of the BESS instrument was calculated, using Monte Carlo simulation by GEANT codes, to be about 0.1m ^{2}sr. In the simulation, the three-dimensional detector configuration is constructed in detail. In Figure 4.14, the energy dependence of acceptance in BESS-95 is shown for different $N_{\rm Expect}$ cuts. In spite of the different configurations in the three flights, the definition of "fiducial volume" is common to all data and the acceptance is practically the same.

Table 4.2: Summary of the live time

flight year	live time (hour)
'93	8.6
'94	7.3
'95	7.6

Table 4.3: Summary of the dead time.

flight year	data process	fast clear	error	dead time
'93	1.5 ms×87 Hz = 0.13	84μs×1.7 kHz = 0.14	–	0.27
'94 first half	1.9 ms×140 Hz = 0.27	84μs×1.3 kHz = 0.11	–	0.38
'94 last half	1.8 ms×100 Hz = 0.18	84μs×1.5 kHz = 0.13	–	0.31
'95	2.1 ms×100 Hz = 0.21	84μs×1.2 kHz = 0.10	0.08	0.39

Exposure Factor ($S\Omega \cdot t$)

Energy spectrum is normalized by exposure factor ($S\Omega t$), where t is the "live time".

The live time, or effective exposure time, can be derived from the ratio of T0 trigger to T0 coincidence, 73.0%, 65.7% and 61.4%, as 3.1×10^4sec (8.6 hours), 2.6×10^4sec (7.3 hours) and 2.7×10^4sec (7.6 hours) as seen in Table 4.2.

The "dead time" of the BESS instrument is caused by two processes; one is the decision time before fast clear (80μs) and the other is process time of data acquisition (1.5 – 2.0 ms). These depend on the status of the instrument, including the number of read-out channel of electronics, the trigger rate and the data size per event. In the '94 flight, a bad gas condition made the chambers noisy and increased data size which lead to a large fraction of dead time. Additionally, in the '95 flight, error due to one bad FADC channel caused another dead time. The 'dead time' of the three flights are summarized in Table 4.3.

4.4.4 Single Track Efficiency (ε_{single})

Since only the cosmic ray particle recognized as a single track undergoes further analysis, a probability that one particle rushing into BESS spectrometer is identified as one particle is crucial. This "single track efficiency" is determined mainly by the interactions in the upper half of the detector. To estimate this efficiency, we need to rely on the Monte Carlo simulations. The energy dependent single track efficiency in BESS-95 is shown in Figure 4.15 as an example. The energy dependent of the efficiency is mostly attributed to the energy dependence of the hadronic interactions.

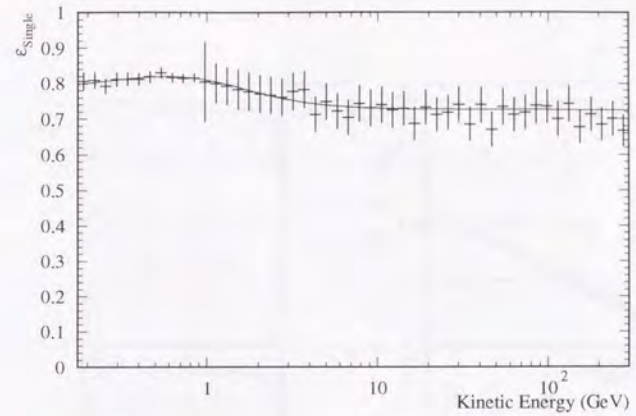

Figure 4.15: The energy dependence of single track efficiency (BESS95).

4.4.5 Quality Cut Efficiencies (ε_{Q-cut})

The quality cut was applied to squeeze out the best performance of rigidity determination especially in high rigidity region. As is described in section 4.2.2, however, even before applying quality cut satisfactory performance is achieved at least in low rigidity region. This situation is clearly shown in Figure 4.16. In the figure, relative fitting error of the transverse rigidity ($\Delta R_t/R_t$) after the quality cuts is shown as function of R_t at left and the differential (hatched) / integral (open) error distribution at R_t =2 GV before (dotted line) and after (solid line) quality cuts is shown at right. Comparing Figure 4.16 with Figure 4.4, the distribution of ($\Delta R_t/R_t$) is almost identical. In this case, the efficiency of the quality cut is evaluated by just dividing the number of events after the quality cut by the number before the cut.

In the high rigidity region, this simple direct method cannot be applied because the number of events is too small to evaluate the efficiency. But it is reasonable to extrapolate the efficiency in lower energy to high energy region. Figure 4.17 and 4.18 shows the distribution of the fourteen parameters used in quality cut for '95 data as an example. The left side figures show for Kinetic energy > 16 GeV and the right ones for Kinetic energy ~ 7 – 16 GeV, respectively. Both histograms have almost identical shape in all fourteen parameters, i.e. all these values have no dependence on rigidity. From these figures it is concluded that the efficiency of the quality cut is constant above around 10 GeV.

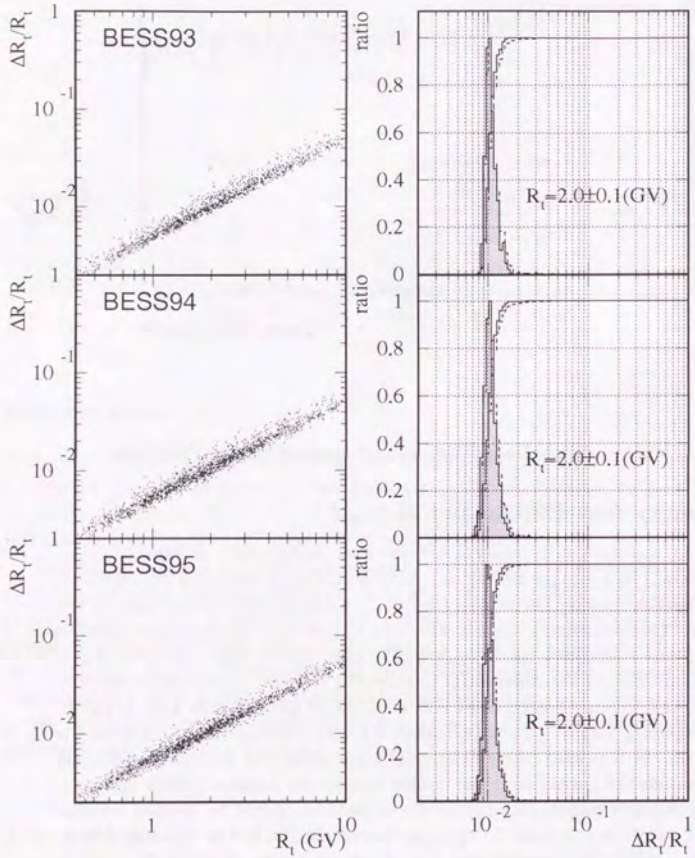

Figure 4.16: Differential (hatched) and integral (open) relative error distribution of transverse rigidity before (doted line) and after (solid line) quality cuts.

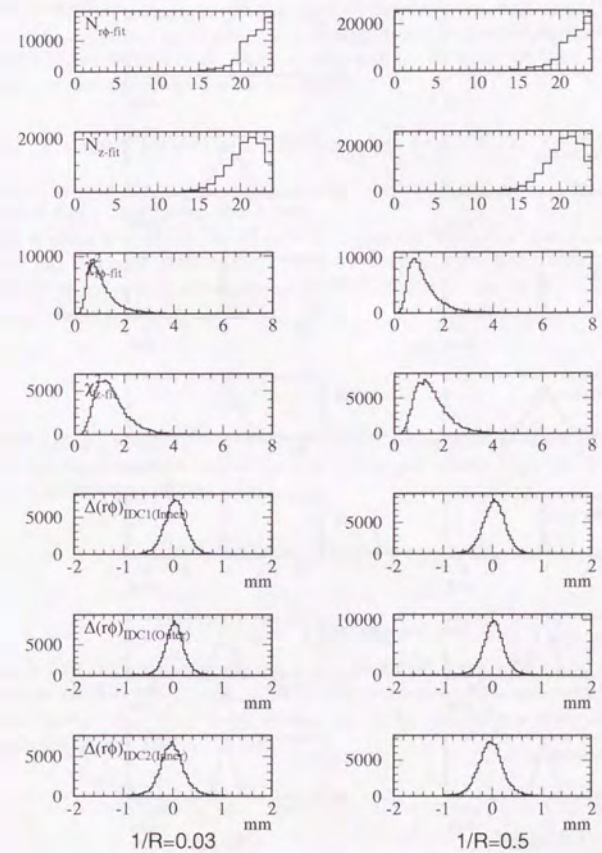

Figure 4.17: The distributions of the parameters used in quality cut (1).

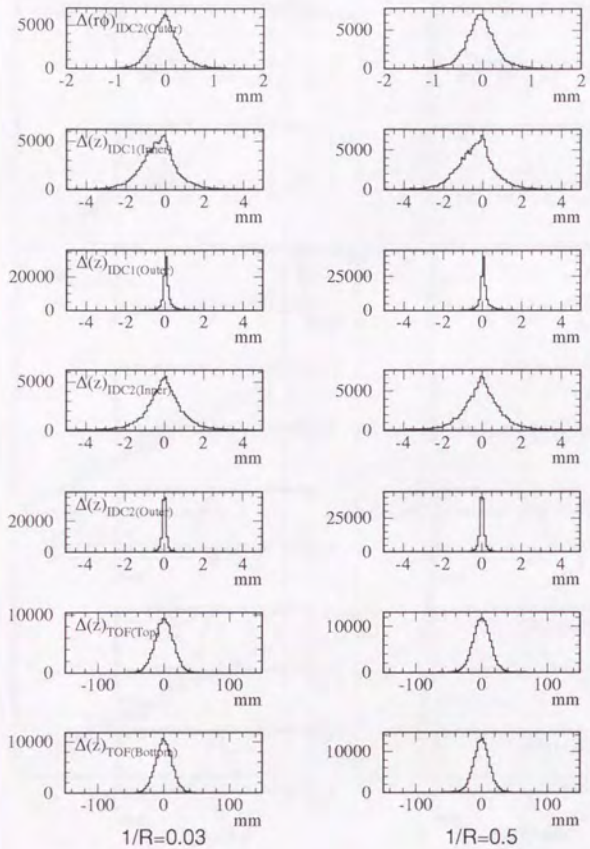

Figure 4.18: The distributions of the parameters used in quality cut (2).

In order to determine the efficiency of the quality cut above 10 GeV, we averaged the efficiencies between 10 and 20 GeV and extrapolated it toward the higher energy region as shown in the bottom of Figure 4.19. In Figure 4.19 are also shown the efficiencies in the track quality cut ($\varepsilon_{\mathrm{Track-QualityCut}}$), in the TOF quality cut ($\varepsilon_{\mathrm{TOF-QualityCut}}$), and the total efficiency in the event quality cut ($\varepsilon_{\mathrm{Q-cut}} = \varepsilon_{\mathrm{Track-QualityCut}} \times \varepsilon_{\mathrm{TOF-QualityCut}}$). High efficiencies around 80% was achieved. A relatively low efficiency of Track-quality cut in '94 flight suffered from the bad condition of the chambers during the flight.

4.4.6 Proton Selection Efficiencies ($\varepsilon_{P-select}$)

The efficiencies of the proton selection (the $\mathrm{d}E/\mathrm{d}x$-cut and β-cut) are derived from the actual flight data for proton events.

The distribution of $\mathrm{d}E/\mathrm{d}x$ is well described as Vavilov or Landau distribution and $1/\beta$ has Gaussian distribution. Once the probability density function is known, the efficiencies of proton selection can be evaluated; 95% for $\mathrm{d}E/\mathrm{d}x$-cut and 99.99% for β-cut, respectively.

At this stage, the number of particles identified as protons in the analysis N_{obs} is converted into the proton flux at the top of the instrument F_{TOI} (at 5g/cm^2 depth) using the online- and off-line efficiencies;

$$F_{TOI}(E) = N_{obs}(E) \cdot \frac{1}{\varepsilon(E)} \cdot \frac{1}{S\Omega(E) \cdot t}, \tag{4.1}$$

where

$$\varepsilon(E) = \varepsilon_{Trigger} \cdot \varepsilon_{single} \cdot \varepsilon_{Q-cut} \cdot \varepsilon_{P-select}.$$

$\varepsilon_{Trigger}$ is the trigger efficiency, ε_{single} is the single track efficiency, ε_{Q-cut} is the quality cut efficiencies, $\varepsilon_{P-select}$ is the proton selection efficiencies and $S\Omega t$ is the exposure factor. E is the energy at the top of the atmosphere after the correction of ionization energy loss in the air.

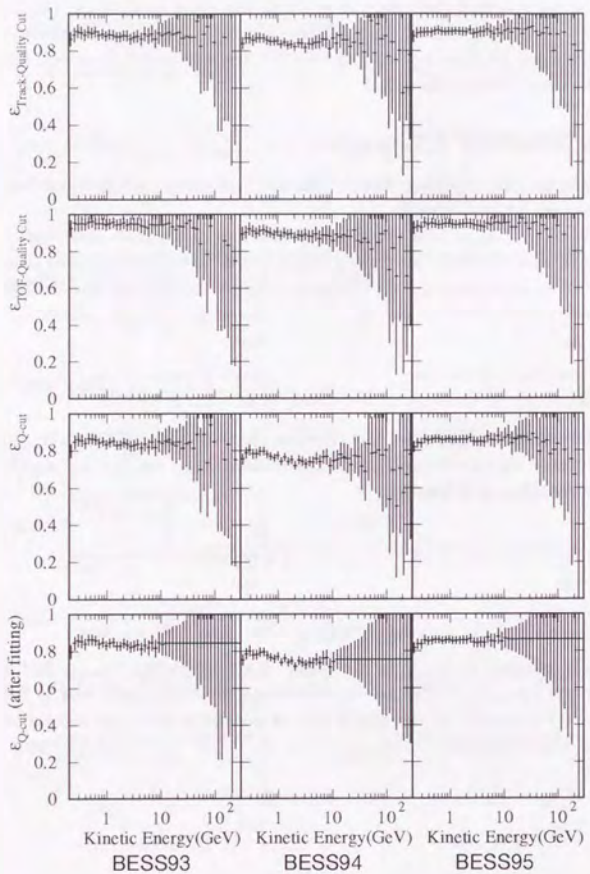

Figure 4.19: The efficiencies of the quality cuts.

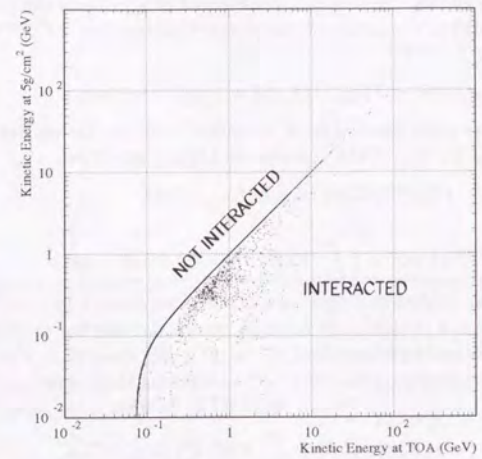

Figure 4.20: The simulated energies of protons at the top of atmosphere and at the depth of 5 g/cm^2.

4.4.7 Interactions in the Atmosphere

In order to grasp the effect of residual air on the cosmic ray proton spectrum shape, we performed Monte Carlo simulations using GEANT. The Monte Carlo data are produced by injecting the protons having the same energy spectrum as used in [22] into the air of 5 g/cm^2 thick.

Figure 4.20 shows the relations between the simulated energies at the top of atmosphere and at the depth of 5 g/cm^2. There found in Figure 4.20 are two component: one is a sparse area which looks like a mist (labeled "INTERACTED") and the other is a dense line (labeled "NOT INTERACTED").

The events found inside the "INTERACTED" area are "secondary protons". Some of them are incident primary protons which entered the atmosphere and slowed down resulting from inelastic interactions. The others are produced by the inelastic interactions of incident primary protons with air nuclei. These secondary portions should be subtracted in order to obtain the primary flux at the top of the atmosphere.

On the other hand, the events lying inside the "NOT INTERACTED" line are incident "primary protons" which didn't suffer any hadronic interactions and just lost there energy in ionizing process. Some of the primary protons entered the atmosphere were lost while traveling in the air. These negative contributions should be compensated to evaluate the primary flux at the top of the atmosphere.

Figure 4.20 indicates that the proton flux observed at the top of the instrument F_{TOI} (at 5g/cm^2 depth) is composed of the primary proton flux $F^{primary}$ and the secondary proton flux $F^{secondary}$:

$$F_{TOI}(E)dE = F_{TOI}^{primary}(E)dE + F_{TOI}^{secondary}(E)dE. \tag{4.2}$$

The two terms on the right hand side of equation (4.2) can be written using a primary proton flux at the top of the atmosphere (F_{TOA}) as follows:

$$F_{TOI}^{primary}(E)dE = \eta(E)F_{TOA}(E)dE \tag{4.3}$$

and

$$F_{TOI}^{secondary}(E)dE = \left(\int_E^\infty Y(E,E')F_{TOA}(E')dE'\right)dE, \tag{4.4}$$

where $\eta(E)$ means the probability that incident proton doesn't interact with air nuclei, while $Y(E,E')$ is a proton-yield function, which denotes the number of secondary protons in the energy region from E' to $E'+dE'$ created in hadronic interactions by a primary proton with energy E. Combining these equations, we can obtain the relation between $F_{TOA}(E)$ and $F_{TOI}(E)$ as follows:

$$F_{TOI}(E) = \eta(E)F_{TOA}(E) + \int_E^\infty Y(E,E')F_{TOA}(E')dE'. \tag{4.5}$$

Atmospheric Secondary Production

The observed protons include the atmospheric secondary protons which are produced in the atmosphere above the instrument by collisions of the cosmic rays with air nuclei. These portions (the second term on the right hand side of equation (4.5) and (4.4)) should be subtracted in order to obtain the primary flux at the top of the atmosphere. We estimated these atmospheric secondary protons by the following two methods; one is M.C. simulations, and the other is solving sets of coupled transport equations accomplished by P.Papini et al.[22]. In these estimations, we have to know the primary proton flux at the top of the atmosphere (F_{TOA}). In our M.C. calculation, we made use of the same spectrum as used in [22]. As shown in Figure 3.6 in Chapter 3, the solar modulation was very close to the minimum and we adopted the primary proton flux for minimum solar modulation.

Once the primary and secondary proton spectrum are obtained, the ratio of secondary to primary protons (R_{air}) can be defined [22]:

$$R_{air}(E) = \frac{F_{TOI}^{secondary}(E)}{F_{TOA}(E)}. \tag{4.6}$$

Figure 4.21 shows the calculated ratio R_{air}. Two M.C. calculations were performed with GEANT simulation code using GHEISHA and FLUKA packages for hadronic interactions. All the three ratios agree well within 1% above 1 GeV and 4% above 0.4 GeV.

The ratio depends on the primary proton flux, and in order to obtain the primary proton flux, iterative calculations using the equation (4.5) are necessary. In our analysis, however, assumed primary proton flux and obtained primary proton flux after all corrections agree very well and no iterative calculation was done.

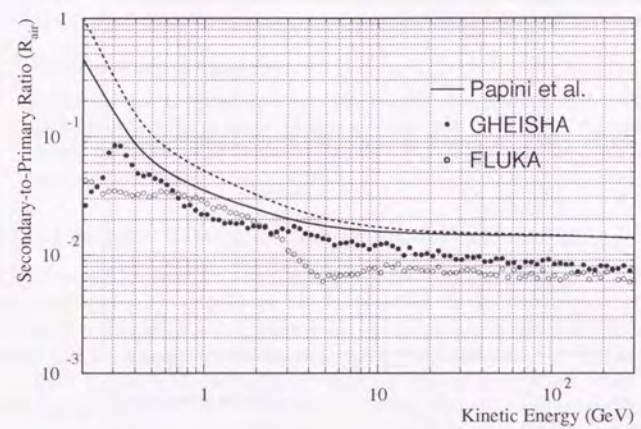

Figure 4.21: The ratio of the secondary proton flux at 5 g/cm^2 depth to the incident proton flux at the top of the atmosphere. Solid and dashed curves : minimum and maximum solar modulation[22]. • and ∘ : M.C. data using GHEISHA and FLUKA packages for hadronic interactions.

Losses in the Atmosphere $(1-\eta)$

Interactions in the 5 g/cm^2 of the atmosphere above the instrument reduce the number of protons to be observed in the experiment. We defined "survival probability" $(\eta(E))$ as the probability that the protons with certain energy at the top of atmosphere can penetrate 5 g/cm^2 of the atmosphere without hadronic interactions. (see equation (4.3)). Figure 4.22 shows the survival probability of protons estimated from the M.C. events shown in Figure 4.20. The survival probability of protons is as high as 95% over the entire energy range.

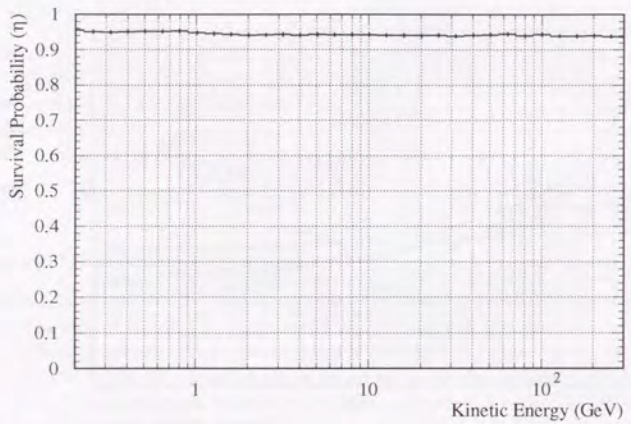

Figure 4.22: Survival probability of protons for 5 g/cm^2 of the atmosphere. The losses are due to interactions.

4.4.8 Summary of Corrections

Combining all the corrections mentioned above, the proton flux at the top of the atmosphere F_{TOA} can be obtained as follows:

$$F_{TOA}(E) = N_{obs}(E) \cdot \frac{1}{\varepsilon(E)} \cdot \frac{1}{S\Omega(E)} \cdot \frac{1}{t} \cdot \frac{1}{\eta(E) + R_{air}(E)}. \tag{4.7}$$

4.5 Background estimation

Because proton is the most abundant component in cosmic rays, if the single track events are correctly selected and its efficiency is well known, the effect of the background processes should be very small. But to ensure that proton-selection is correctly performed, examining the background processes which may fake protons is important. The background processes are categorized as follows:

1. Positive charged particles

   Because of the finite resolution of the TOF measurement, it is impossible to distinguish the particle species except in the rigidity region below a few GV. Any kinds of positive single charged particles may fake protons.

2. Albedo negative charged particles

   Albedo particles, which entered the detector from below and exited at the top, have opposite curvature to that of down-going particles. Albedo negative charged particles could be selected when their TOF values were wrong by more than ten nanosecond.

4.5.1 Positive Charged Background Particles

In order to select protons, cuts on the values of $\mathrm{d}E/\mathrm{d}x$ and $1/\beta$ are applied. Multiple charged particles such as heliums can be rejected almost perfectly by the $\mathrm{d}E/\mathrm{d}x$ cut. Therefore the main background source is deutrons. In the low rigidity region deutrons can be separated from protons using the information of $1/\beta$ as shown in Figure 2.40. Figure 4.23 shows the deutron (+ proton) energy spectrum. Because above 0.8 GeV (2.0 GeV) in '93 and '94 ('95) data, deutron's and proton's $1/\beta$-band overlaps each other, Figure 4.23 shows strange behavior in higher rigidity region. Assuming that deutron's and proton's energy spectrum have the same shape, the ratio of deutrons to protons can be estimated to be about 1/40. Thus deutron has negligible effect on observed proton spectrum.

4.5.2 Albedo negative charged particles

The chance of an albedo negative charged particle faking proton is also extremely small, since downward $(1/\beta > 0)$ and upward $(1/\beta < 0)$ moving particles are clearly separated as it is clear from Figures 4.2. Figure 4.24 shows the projection onto $1/\beta$ axis. There are no tail events which spill beyond $\beta^{-1} = 0$ both for down-going and up-going particles.

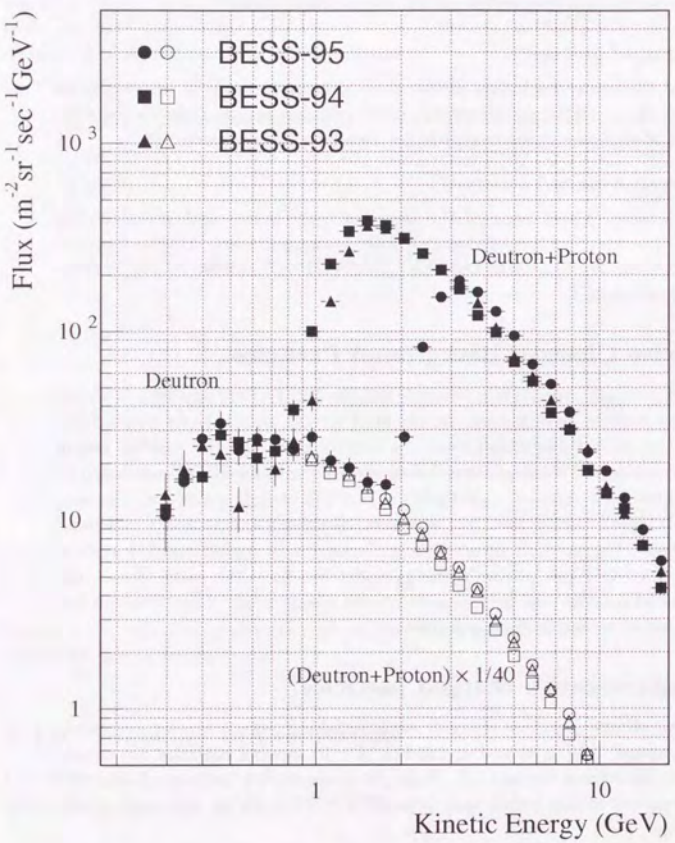

Figure 4.23: Deutron energy spectrum.

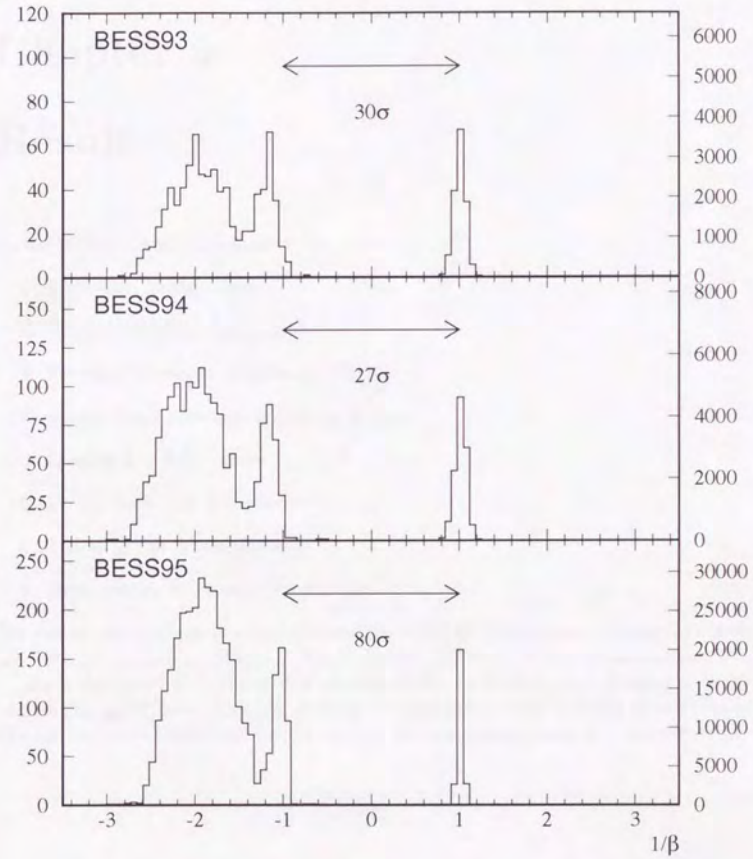

Figure 4.24: β^{-1} distribution.

Chapter 5

Result

As described in section 4.4, after the corrections of

1. Ionization Energy Loss
2. Trigger Efficiency ($\varepsilon_{Trigger}$)
3. Energy dependent acceptance ($S\Omega$)
4. Single Track Selection Efficiency (ε_{single})
5. Quality Cut Efficiencies (ε_{Q-cut})
6. Proton Selection Efficiencies ($\varepsilon_{P-select}$)
7. Losses in the Atmosphere
8. Atmospheric Secondary Production,

the proton spectrum at the top of atmosphere (TOA) is obtained. Figure 5.1 shows the obtained proton spectrum at TOA. This is the result of our measurement.

As is described in Chapter 6, a change of flux in the low energy range is owing to the change of solar activity. During '95-flight, the solar activity is most quiet among the three flights and proton flux in the low energy range is relatively high.

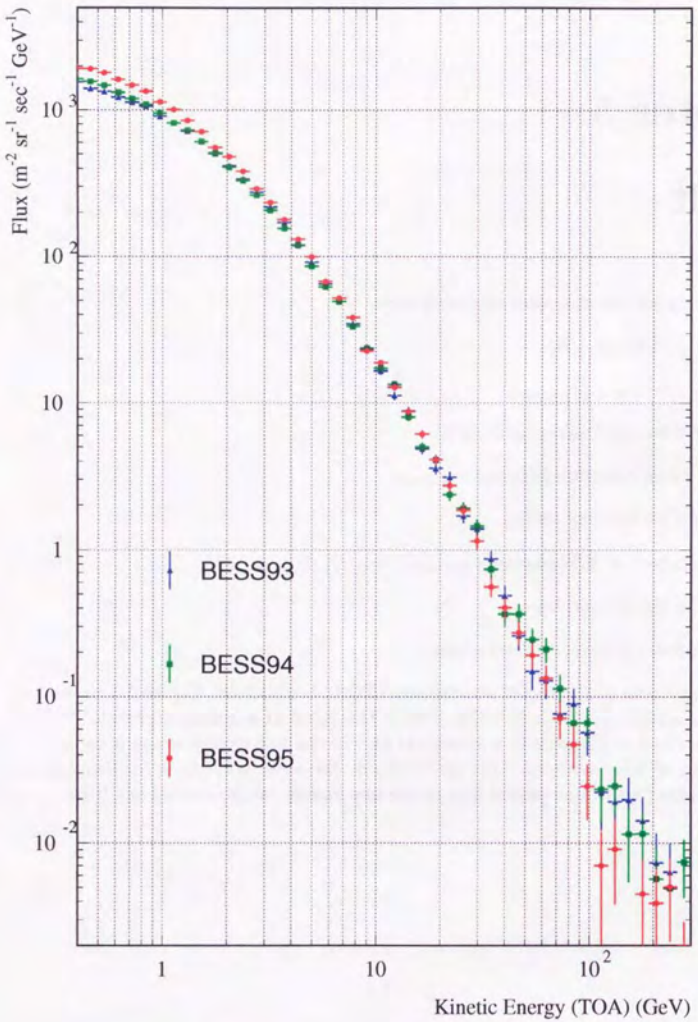

Figure 5.1: Proton Energy Spectrum at the top of Atmosphere.

Chapter 6

Discussion

6.1 Error Estimation

The expression of the error of the proton flux will be derived from equation (4.7), assuming the variables are independent;

$$\left(\frac{\Delta F}{F}\right)^2 = \left(\frac{\Delta N_{obs}}{N_{obs}}\right)^2 + \left(\frac{\Delta \varepsilon}{\varepsilon}\right)^2 + \left(\frac{\Delta(S\Omega)}{S\Omega}\right)^2 + \left(\frac{\Delta t}{t}\right)^2 + \left(\frac{\Delta(\eta + R_{air})}{\eta + R_{air}}\right)^2 \quad (6.1)$$

The first term is the statistical error, and the others are systematic errors.

6.1.1 Statistical error

In the obtained proton spectrum, the number of events per bin is large, so the statistical error is easy to estimate. Shown in Figure 5.1 are the statistical error only.

6.1.2 Systematic error

1. Error in the efficiencies ($\Delta\varepsilon_{selection}$)

   The efficiencies used in deriving the proton flux are decomposed into three categories, i.e. ,

   - Single track selection efficiency (ε_{single}),
   - Quality cut efficiency (ε_{Q-cut}),
   - Proton selection efficiency ($\varepsilon_{P-select}$).

   The first ε_{single} is obtained from M.C. simulation. The systematic error of the single track selection efficiency is estimated by examining agreements between observed and simulated distributions of the values used in single track selection ($N_{\mathrm{TOF(Top)}}$, $N_{\mathrm{TOF(Bottom)}}$ and N_{Track})

The two main sources of multiple hits in TOF counters are the interaction which occurs inside the the coil and the chance that the incident particle passing through near the side end of TOF counter loses its energy both in two adjacent counters. We checked the rate of these multi-$N_{\rm TOF}$ events by comparing the result of scanning 500 real data events with M.C. simulated data. The probability of interaction events is 3.4±0.8% in the real data and 4.2±0.04% in the M.C. The probably of two adjacent counters hit is 3.0±0.8% in the real data and 4.8±0.04% in the M.C. The difference between real data and M.C. data is 2.6% in total. Furthermore, from the scanning 1500 real data events, only 1.1±0.2% of the single track events were missed in track reconstruction process. From these studies, we estimate that the systematic error of the single track selection efficiency is 3%.

Essentially, the quality cut should not cause any errors in the low rigidity region up to around 10 GV. Comparing ε_{Q-cut} and $\varepsilon_{Q-cut}(after fitting)$ shown in the bottom part of Figure 4.19, the error in ε_{Q-cut} was estimated to be 10% around 100 GV.

The ambiguity in proton selection efficiency ($\varepsilon_{P-select}$) lies mainly in the dE/dX cut. The efficiency of dE/dX is as high as 95%, and we estimated its error should be as small as 3%.

Summing up all the estimated errors, the total error in the efficiency was about 5% at energies below 10 GeV and 11% above 10 GeV.

$$\frac{\Delta\varepsilon}{\varepsilon} \simeq \begin{cases} \pm 5\% & (E < 10\ \text{GeV}) \\ \pm 11\% & (10\ \text{GeV} \leq E) \end{cases}$$

2. Error in the geometrical acceptance ($\Delta S\Omega$)

   The geometrical acceptance could be obtained only from the Monte Carlo simulation. The geometrical acceptance is prescribed by "fiducial volume" cut, namely by $N_{\rm Expect}$, $z_{\rm Track@TOF(Top)}$ and $z_{\rm Track@TOF(Bottom)}$. If the distribution of each value obtained from the flight data and the simulated data are consistent with each other, the geometrical acceptance will have no error. These distributions are well reproduced by M.C. simulation, but the M.C. distributions have slightly different rigidity dependence. Based on this small difference, we estimate the error of the geometrical acceptance

$$\left(\frac{\Delta(S\Omega)}{S\Omega}\right) \simeq \pm 5\%$$

3. Error in the 'live time' (Δt)

   The 'live time' t was derived by multiplying the total exposure time with the ratio of the live time to the exposure time, which is measured exactly by the ratio of the issued number of T0 trigger (gated by the "ready" status) to the number of ungated T0 triggers. The error in the live time thus is negligibly small.

$$\left(\frac{\Delta t}{t}\right) \simeq 0$$

4. Error in correction of loss and secondary protons in air ($\Delta\eta$ and ΔR_{air})

   Essentially, the correction of air effect can be evaluated by M.C. simulation if simulation code can simulate all the interactions completely. Hence, we consider the errors of η and R_{air} simultaneously.

   The losses of protons due to the annihilation and the inelastic collisions in the residual atmosphere were estimated by Monte Carlo simulations. There were ambiguities in the cross sections used in the simulation and in the simplified model of the atmosphere. We estimate it is 5%.

   The calculation of the atmospheric secondary proton flux involves some approximations and energy dependent cross sections. The value of R_{air} could change by a factor of 3 around 3 GeV due to these uncertainties[22]. As shown in Figure 4.21, the ratio of secondary protons to primaries varies from 20% at 0.2 GeV to 2% at 10 GeV, so the uncertainty of factor 3 in R_{air} changes the primary flux +33/−11% at 0.5 GeV, +6/−2% at 1 GeV and +1/−1% at 10 GeV.

   Summing up above two factors, we estimated the error in the correction of loss and secondary protons as follows:

$$\frac{\Delta(\eta + R_{air})}{\eta + R_{air}} \simeq \begin{cases} +33/-12\% & (E = 0.5\ \text{GeV}) \\ +8/-5\% & (E = 1\ \text{GeV}) \\ +1/-1\% & (E \geq 10\ \text{GeV}) \end{cases}$$

Table 6.1 summarizes the systematic uncertainties.

Table 6.1: Summary of systematic errors of proton flux.

Kinetic Energy (TOA)	0.5 GeV (%)	1 GeV (%)	10 GeV (%)	100 GeV (%)
Geometrical acceptance	±5	±5	±5	±5
Effective exposure time	±0	±0	±0	±0
Efficiencies	±5	±5	±11	±11
Atmospheric corrections	+33/−12	+8/−5	+1/−1	+1/−1
Total	+34/−14	+10/−9	+13/−13	+13/−13

6.2 Spectrum Deformation by Finite Resolution

Because the rigidity measurement has a finite resolution and the proton flux has a very steep spectrum shape, the observed proton energy spectrum may suffer deformation, i.e. , it may have a "tail" above around 200 GV. In order to estimate an effect of this deformation, we simulated the effect of the finite resolution in the rigidity measurement. The error in rigidity measurement ($\Delta(1/R_t)$) was tuned up to reproduce the distributions shown in Figure 2.39. Figure 6.1 shows the simulated spectrum together with the input spectrum. This figure indicates that up to 100 GeV the observed spectrum will not significantly deviate from the original spectrum. In the next section, we limit the energy range below 100 GeV.

6.3 Comparison with Early Work

In Figure 6.2, the obtained spectrum from the compilation of three flight data is compared with previous experiment. Our spectrum is consistent with the flux which shows the lower fluxes reported previously.

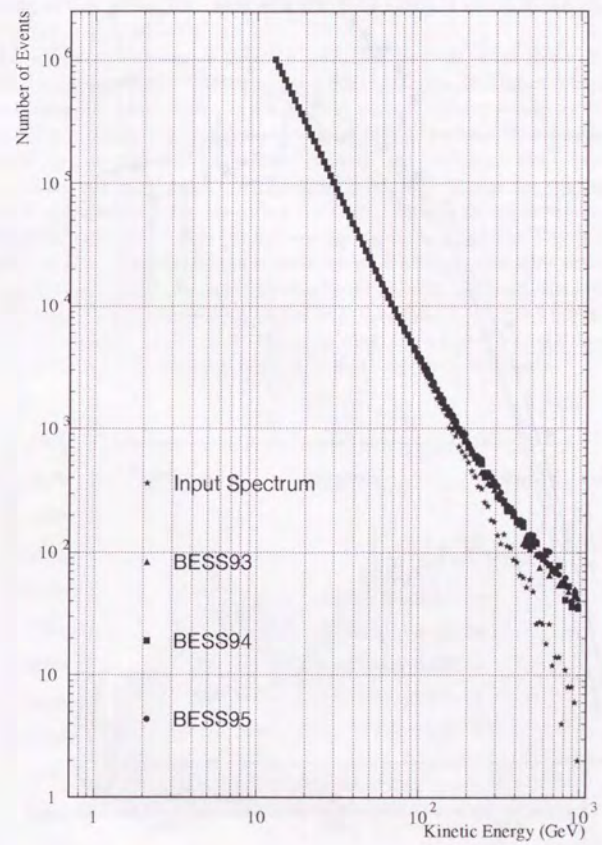

Figure 6.1: Simulated spectrum shapes.

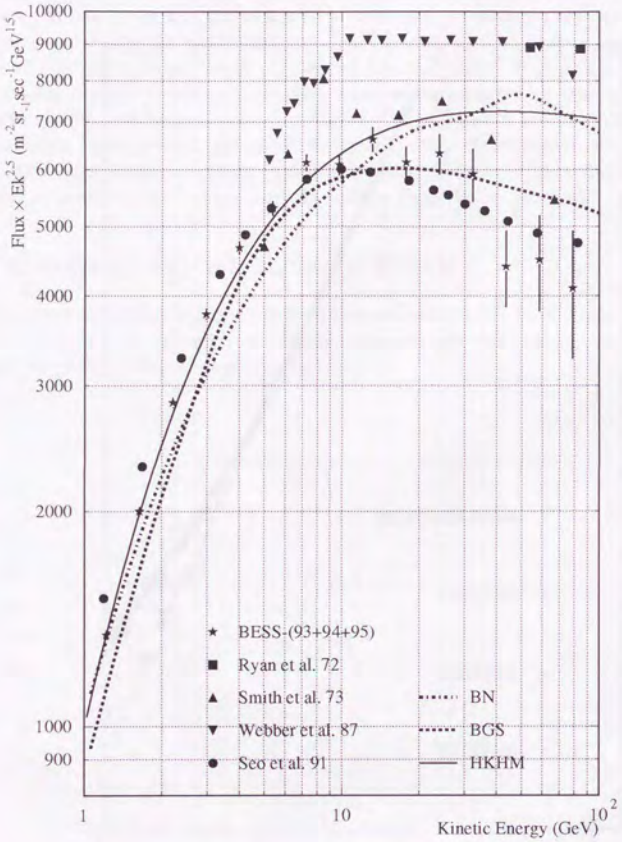

Figure 6.2: Absolute differential proton spectrum obtained by BESS experiment together with the spectrum obtained by previous experiments and those assumed spectrum in M.C. calculations of the atmospheric neutrino spectra by BGS[11], HKHM[12] and BN[13].

6.4 Solar Modulation

6.4.1 Solar Activity

A change of flux in the low energy range ($\leq$ 10 GeV) is owing to the change of solar activity (solar modulation).

The solar activity varies globally with the 11 year solar cycle and it was on its way to approach the minimum since '91 as shown in Figure 3.6(a). The solar activity changes, however, in much shorter period. There shown in Figure 6.3 are the of 7-day average (open histogram) and 27-day average (hatched histogram) of the counting rate of CLIMAX neutron monitor. According to the 7-day average, the solar activity was more quiet in BESS93 than in BESS94, but the contrary according to the 27-days average On the other hand, the proton fluxes measured in BESS93 and BESS94 are almost same at low energy region as shown in Figure 5.1. It seems to reflect the fact that the flux of cosmic ray is affected by the solar activity averaged over a half of a month. In order to clarify the relation between the cosmic ray flux and the solar activity, repeating flights over one solar cycle (at least half cycle) are desired. Especially, the fluxes at the solar maximum and solar minimum period are very important information to study the solar modulation theory.

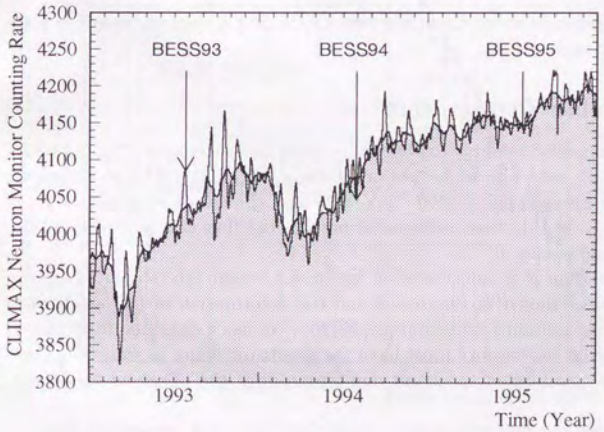

Figure 6.3: Solar activity; 7 days average (open histogram) and 27 days average (hatched histogram)

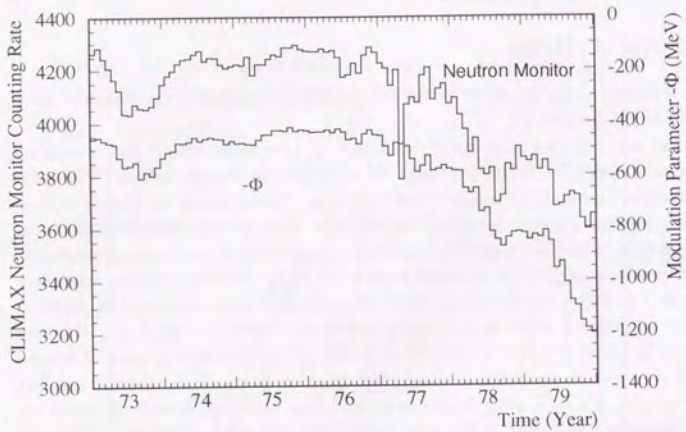

Figure 6.4: Time dependence of Counting rate of CLIMAX neutron monitor and solar modulation parameter[24].

6.4.2 Interstellar Proton Flux

The effect of solar activity is simply expressed by using one parameter, "modulation parameter" Φ, which acts like as a "potential energy"[23][24]. The modulation parameter changes around 400 – 1400 MeV with the change of solar activity as shown in Figure 6.4. In this case, interstellar proton flux flux can be evaluated in the limit when Φ approaches 0.

The solar modulation is demonstrated in Figure 6.5, where interstellar (IS) proton flux is assumed as shown in Figure 6.6 and the deformation of (IS spectrum) is calculated by using a numerical technique[25][26]. We can't conclude from these figures that interstellar proton flux must have the spectrum shape as shown in Figure 6.6 because the modulated spectrum don't reproduce the observed spectrum perfectly.

In order to determine the interstellar proton flux, the most important data is proton flux at the top of atmosphere observed in solar minimum epoch, which will come in '97. The proton spectrum whose shape is relatively close to the IS spectrum will be observed.

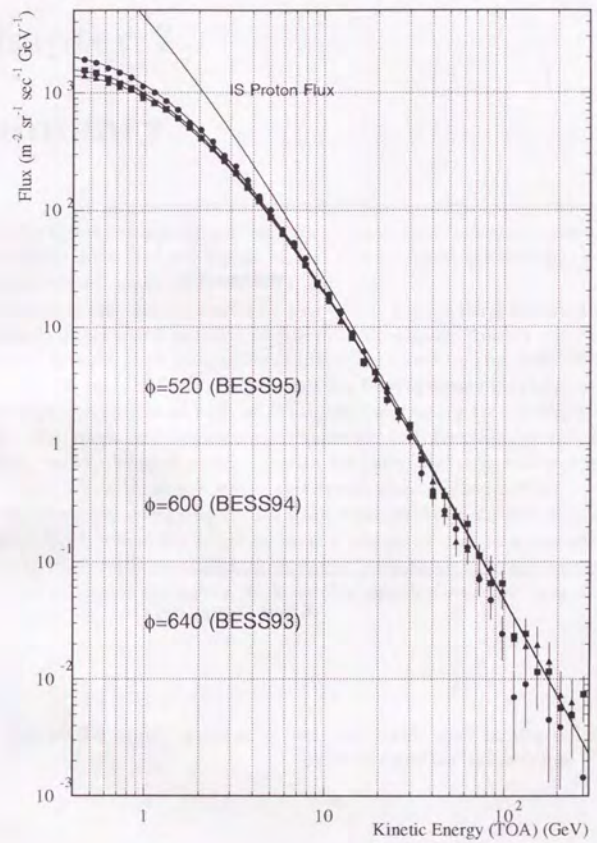

Figure 6.5: Solar modulation.

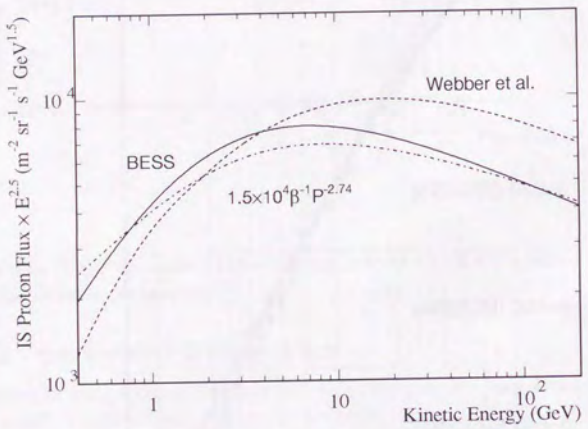

Figure 6.6: Interstellar proton flux. Solid line:used in making Figure 6.5 dashed line:Webber et al.[8] and dot-dashed line:Mitsui[26]

Chapter 7

Summary

The differential cosmic ray proton spectra have been measured using the data obtained from three balloon flights of BESS spectrometer which has been launched from Northern Canada in 1993, 1994, and 1995.

In the analysis, events with a single track in the tracking chamber were selected. In order to improve the rigidity resolution in the highest rigidity region event quality cuts were applied. The protons were identified based on the measurements of magnetic rigidity, time of flight, and energy loss in the plastic scintillators. The overall selection efficiency was as high as 75%. After correcting for the selection efficiencies and for the losses and secondary protons due to interaction in the air and in the detector, we've obtained energy spectra for three flights in the energy region from 0.4 to 100 GeV with an estimated systematic error of about 10%.

The measured energy spectrum from three flights data are in good agreement above 10 GeV, where the effect of solar modulation can be neglected. On the one hand, the effect of solar modulation is clearly observed in lower energy region.

Our spectrum is consistent with the flux which shows the lower fluxes reported previously.

Acknowledgments

I wish to express my sincere thanks to Professor S. Orito who has led the BESS experiment, for his guidance throughout my research reported in this thesis. I also wish to gratefully appreciate Professor A. Yamamoto who has managed the campaign and lead it to a success. The analysis were done owing a lot to Prof. S. Orito, K. Yoshimura, H. Matsunaga and M. Motoki. I would like to acknowledge them for their suggestions and helpful discussions and assistance at the various stages of the analysis.

I would like to thank all the BESS colleagues for their effort to make a success of the experiment, especially M. Nozaki, M. Imori, T. Yoshida and K. Yoshimura for their overall contributions; K. Anraku, T. Saeki, I. Ueda, H. Matsunaga, M. Motoki, N. Takimi, H. Matsumoto, M. Otoba, M. Kobayashi, K. Suzuki and Y. Nishihara. for their excellent works on the experiment. I also thank Y. Makida, K. Tanaka, M. Kimura, and the other staffs who have worked on the superconducting magnet; J. Suzuki, Y. Higashi, Y. Ajima, S. Koizumi, and all the other KEK staffs who contributed to the construction of the BESS instruments. I am grateful to D. Righter for his technical support. I am also indebted to K. Shimamura, T. Haga, T. Tsunoda, H. Honda and all the other people who were once involved in the experiment. It is a pleasure to express my appreciation to J. Ormes, A. Moiseev, R. Streitmatter, J. Mitchell, N. Yajima, T. Yamagami, E. S. Seo, B. Kimbell, and S. Stochaj, and the late Professor R. Golden, who are the collaborators of the experiment.

I greatly appreciate helpful suggestions from Professor. J. Nishimura, discussions with T. Mitsui and K. Maki about the theoretical calculations. I also thank the people in Lynn Lake for their kind hospitality during our stay there.

Furthermore, I am grateful to Dr. V. Jones and all other people at NASA who supported BESS, and to the balloon campaign team from the National Scientific Balloon Facility for their professional and skillful work in carrying out the BESS flights. I greatly acknowledge Professor. A. Nishida, Director General of ISAS, Professor. H. Sugawara, Director General of KEK, and Professor. S. Iwata of KEK for their support and encouragement. Sincere thanks go to International Center for Elementary Particle Physics (ICEPP) of University of Tokyo for kindly allowing me to use their workstations. The data of the CLIMAX neutron monitor were provided by Space Physics Data System of University of Chicago, supported by National Science Foundation Grant ATM-9420790. The BESS experiment has been supported by Monbusho International Scientific Research Grant and Scientific Research Grant, Kurata Research Grant, and Sumitomo Research Grant.

References

[1] K.S.Hirata *et al.*, Phys. Lett. B **280**, 146 (1992).

[2] E.W.Beier *et al.*, Phys. Lett. B **283**, 446 (1992).

[3] Y.Fukuda *et al.*, Phys. Lett. B **335**, 237 (1994).

[4] M.Honda *et al.*, Phys. Rev. D **52**, 4985 (1995) .

[5] J.F.Ormes *et al.*, J. Geophys. Res. **73**, 4231 (1968).

[6] M.J.Ryan *et al.*, Phys. Rev. Lett. **28**, 985 (1972).

[7] L.H.Smith *et al.*, Astrophys. J., **180**, 987 (1973).

[8] W.R.Webber *et al.*, Proc. 20th Internat. Cosmic Ray Conf. (Moscow), **1**,325 (1987).

[9] Eun-Suk Seo, Ph. D. thesis, Louisiana State Univ., (1991).

[10] E.S.Seo *et al.*, Astrophys. J., **378**,763 (1991)

[11] Giles Barr *et al.*, Phys. Rev. D **39**, 3532 (1989).

[12] M.Honda *et al.*, Phys. Lett. B **248**, 193 (1990).

[13] E.V.Bugaev and V.A.Naumov, Phys. Lett. B **232**, 391 (1989).

[14] Orito, S., Proc. of the ASTROMAG Workshop, KEK Report 87-19, 111 (1987).

[15] A. Yamamoto *et al.*, IEEE Trans. on Magnetics **24**, 1421 (1988).

[16] T. Massam CERN 76-21 (1996).

[17] T. Saeki *et al.*, Nucl. Instr. and Meth., A **355**, 506 (1995).

[18] Goossens, M., *ZEBRA – Overview of the ZEBRA system*, CERN Program Library Q100/Q101. CERN, 1993.

[19] Application Software Group, *HEPDB – Database Management Package*, CERN Program Library Q180. CERN, 1993.

[20] V. Karimäki, Report of University of Helsinki, HU-SEFT-1991-10.

[21] Bruyant, F.*et al.*, *GEANT – Detector Description and Simulation Tool*, CERN Program Library W5013. CERN, 1993.

[22] P.Paoini, C.Grimani and A.Stephens, NUOVO CIMENT **19** 367 (1996).

[23] L.J.Gleeson and W.I.Axford, Astrophys. J. **154** 1011 (1968).

[24] M.Garcia-Munoz *et al.*, Astrophys. J. Suppl. **64** 269 (1987).

[25] L.A.Fisk, J. Geophys. Res., **76** 221 (1971).

[26] T.Mitsui, Ph. D. thesis, Univ. of Tokyo, (1996).